Applications of spectroscopy with multiwavelength sources

Hänsel, A.

DOI
10.4233/uuid:99887eda-5264-4564-888e-dcaf2dbae356

Publication date
2018

Document Version
Final published version

Citation (APA)
Hänsel, A. (2018). *Applications of spectroscopy with multiwavelength sources*. [Dissertation (TU Delft), Delft University of Technology]. https://doi.org/10.4233/uuid:99887eda-5264-4564-888e-dcaf2dbae356

Applications of Spectroscopy with Multiwavelength Sources

APPLICATIONS OF SPECTROSCOPY WITH MULTIWAVELENGTH SOURCES

Proefschrift

ter verkrijging van de graad van doctor
aan de Technische Universiteit Delft,
op gezag van de Rector Magnificus Prof. dr. ir. T.H.J.J. van der Hagen,
voorzitter van het College voor Promoties,
in het openbaar te verdedigen op maandag 4 juni 2018 om 10:00 uur

door

Andreas HÄNSEL

Diplom-Physiker,
Friedrich-Schiller-Universität, Jena, Duitsland,
geboren te Erfurt, Duitsland.

Dit proefschrift is goedgekeurd door de

promotor: Prof. dr. H.P. Urbach
copromotor: Dr. N. Bhattacharya

Composition of the doctoral committee:

Rector Magnificus,	voorzitter
Prof. dr. H.P. Urbach,	Technische Universiteit Delft, The Netherlands
Dr. N. Bhattacharya,	Technische Universiteit Delft, The Netherlands

Onafhankelijke leden:

Dr. S.T. Persijn	VSL - Dutch Metrology Institute
Dr. E.A.J.M. Bente	Technische Universiteit Eindhoven
Prof. dr. A. Kemp	University of Strathclyde
Prof. dr. K.-J. Boller	Universiteit Twente
Prof. dr .ir. J.L. Herder	Technische Universiteit Delft
Prof. dr. G. Vdovin	Technische Universiteit Delft, reservelid

Keywords: Integrated Optics, Frequency Comb, Spectroscopy, Virtually Imaged Phased Array

Printed by: Ipskamp Printing

Front & Back: Cover art designed by Frederikke Chang Winterberg.

ISBN 978-94-028-1084-4

An electronic version of this dissertation is available at
http://repository.tudelft.nl/.

CONTENTS

Summary ix

Samenvatting xi

1 Introduction 1
- 1.1 Integrated optics . . . 4
- 1.2 Frequency comb technology . . . 4
- References . . . 5

2 Design and Testing of an Integrated Optical Single-Mode Laser for Absorption Measurements 9
- 2.1 Introduction . . . 10
- 2.2 Fabry-Pérot resonators . . . 10
  - 2.2.1 Propagating wave approach . . . 11
  - 2.2.2 Round-trip model . . . 12
  - 2.2.3 Important quantities . . . 13
- 2.3 The active medium . . . 14
  - 2.3.1 Optical pumping . . . 14
  - 2.3.2 Electrical pumping . . . 15
- 2.4 Lasers . . . 20
  - 2.4.1 Rate equations and two-level systems . . . 20
  - 2.4.2 Intra-cavity filters . . . 21
- 2.5 Generic photonic technologies . . . 22
  - 2.5.1 Used building blocks . . . 23
  - 2.5.2 Used software . . . 25
- 2.6 A Mach-Zehnder interferometer based intra-cavity filter for designing a single-mode laser . . . 26
  - 2.6.1 Working principle . . . 26
  - 2.6.2 CB07_2_3 layout . . . 29
  - 2.6.3 CB07_2_3 performance and results . . . 31
- 2.7 Conclusion . . . 35
- References . . . 36

3 Integrated Optical Single-Mode Ring Laser with Mach-Zehnder Intra-cavity Filters 39
- 3.1 Introduction . . . 40
- 3.2 Laser layout . . . 40
  - 3.2.1 Ring resonators . . . 41
  - 3.2.2 Tuning scheme . . . 43

3.3 Simulations . . . 44
3.4 Experimental results . . . 44
3.4.1 Lasing . . . 44
3.4.2 Single-mode operation . . . 45
3.4.3 Tunability . . . 46
3.5 Conclusion . . . 47
References . . . 48

4 Monolithically integrated widely tunable laser source operating at 2 µm 49
4.1 Introduction . . . 50
4.2 Layout . . . 50
4.3 Measurements . . . 52
4.4 Conclusion . . . 55
References . . . 56

5 Distance metrology with integrated mode-locked ring laser 57
5.1 Introduction . . . 58
5.2 Experimental setup . . . 58
5.2.1 On-chip laser . . . 59
5.2.2 Michelson interferometer . . . 60
5.2.3 VIPA spectrometer . . . 60
5.3 Method and Measurement . . . 61
5.4 Conclusion . . . 62
References . . . 65

6 Spectroscopic gas temperature measurements 67
6.1 Introduction . . . 68
6.1.1 Edlén's equation . . . 68
6.2 Absorption spectroscopy . . . 69
6.3 Setup . . . 69
6.3.1 VIPA spectrometer . . . 70
6.3.2 Frequency comb lasers . . . 76
6.3.3 Second harmonic generation . . . 78
6.4 Measurement procedure . . . 79
6.4.1 Developed software . . . 81
6.5 Obtained data . . . 81
6.5.1 Used equipment . . . 81
6.6 Limitations . . . 81
6.6.1 Thermal expansion of the gas cell . . . 84
6.6.2 Evacuation and filling of the gas cell . . . 85
6.6.3 Linearity of the cameras . . . 85
6.6.4 Camera noise and dead pixels . . . 86
6.6.5 Dynamic range of the camera image acquisition . . . 86
6.7 Conclusion . . . 86
References . . . 87

7 Long path spectroscopic temperature measurements in ambient air 89
7.1 Introduction . . . 90
7.2 Absorption of ambient air . . . 90
7.2.1 Optimal path length . . . 91
7.3 Optical turbulence . . . 93
7.4 Setup . . . 94
7.5 Measurements . . . 94
7.6 Conclusion . . . 94
References . . . 99

8 Improved gas cell experiment 101
8.1 Introduction . . . 102
8.2 Setup . . . 102
8.2.1 Laser source . . . 102
8.2.2 Gas cell . . . 102
8.2.3 VIPA Spectrometer . . . 103
8.3 Data analysis . . . 104
8.3.1 Increasing the temperature . . . 106
8.3.2 Line comparison . . . 108
8.4 Conclusion . . . 109
References . . . 114

9 Conclusion 115

A Appendix 119
A.1 Used equipment . . . 119
A.1.1 Chapter 2 . . . 119
A.1.2 Chapter 3 . . . 119
A.1.3 Chapter 5 . . . 119
A.1.4 Chapter 6 . . . 119
A.2 Maxwell's equations . . . 120
A.3 Stokes relations . . . 121
A.4 Reciprocity principle . . . 122
A.5 Symmetries in couplers . . . 123
A.6 Derivation of (6.20) . . . 124
References . . . 125

Acknowledgements 127

Curriculum Vitæ 131

List of Publications 133

SUMMARY

Spectroscopy is a powerful tool to investigate the physical properties of complex systems. The interaction of light with matter allows to get insights into the structure of it. Chapter 1 is dedicated to introduce this topic and to show the developments of the technologies that paved the way to its success. Special focus is given to the techniques that are used in this work. This includes monolithically integrated tunable laser sources, as well as integrated mode-locked lasers. In Chapter 2 we guide through the design process of single mode laser source using the generic approach and exploiting the availabilty of multi-project wafers. The design of a Fabry-Perot laser along with its benefits, drawbacks and the underlying physical concepts will be demonstrated. This requires theoretical background in solid state physics; the necessary basics are given in the text. Chapter 3 makes use of this background and expand the design to ring lasers. Chapter 3 also illustrates characterisation techniques for such laser sources. The presented device is investigated regarding its capabilities for gas spectroscopy. To reach different absorption lines that enable spectroscopy for different gas species, the laser design has been adapted for longer wavelengths. In Chapter 4 we will show that despite the reduced performance due to the lower technological status, gas spectroscopy can still be feasible with such devices. Besides the spectroscopical applications photonic integrated circuits can find use in the field of distance metrology. A setup verified the feasibility of a mode-locked laser in combination with a VIPA spectrometer to obtain metrological data with a single camera image, which is demonstrated in Chapter 5. This chapter also concludes the investigation of monolithically integrated laser sources.
In addition to on-chip lasers, this work investigates fiber-based frequency comb lasers. With a much lower repetition frequency in comparison to integrated pulsed lasers, the corresponding mode-spacing in the frequency domain sets different requirements of the spectrometer. On the other hand the denser and yet wider spectral coverage allows for spectroscopy over a wider range of absorption lines. Chapter 6 is dedicated to introduce frequency comb lasers and the virtually imaged phased-array (VIPA) spectrometer. The combination of both is used to determine the temperature of CO_2 by looking at its absorption behaviour. Similar measurements have been executed in ambient air and are summarised in Chapter 7. Due to the low concentration of CO_2 in ambient air, this required a very long path length. In Chapter 8 we demonstrate an optimised setup to increase the stability of the method introduced in Chapter 6. The improved setup is more stable with respect to ambient fluctuations and is portable, which allows measurements outside of laboratory conditions.
The final chapter, Chapter 9, summarises the results of all the presented experiments and discusses the impact it can have on future devices making use the presented methods.

SAMENVATTING

Spectroscopie is een krachtig middel om de fysische eigenschappen van complexe systemen te onderzoeken. De interactie tussen licht en materie zorgt ervoor dat men de structuur van deze systemen kan ontrafelen. In hoofdstuk 1 geven we een introductie over dit onderwerp en detailleren we de technologische ontwikkelingen die ervoor zorgden dat spectroscopie succesvol werd. Een speciale focus wordt gegeven aan de technieken die worden besproken in dit hoofdstuk, onder andere monolithisch geintegreerde lasers, wiens lasing golflengte afstembaar is, en geintegreerde mode locked lasers. In hoofdstuk 2 leggen we het ontwerp van een single mode laser bron uit via de algemene aanpak en hoe multi-project wafers hiervoor kunnen worden aangewend. Het ontwerp van een Fabry-Perot laser, alsook de voor- en nadelen en de onderliggende fysische concepten, worden gedemonstreerd. Om dit te begrijpen, heeft men een theoretische voorkennis in vastestoffysica nodig; de noodzakelijke basiskennis wordt gegeven in de tekst. Hoofdstuk 3 maakt gebruik van deze voorkennis en breidt het uit naar het ontwerp van ring lasers. Hoofdstuk 3 illustreert ook verschillende technieken die worden gebruikt om deze laser bronnen te karakteriseren. We onderzoeken in hoeverre het voorgestelde ontwerp kan worden aangewend voor gas spectroscopie. Om verschillende absorptielijnen te genereren die de spectroscopie mogelijk maken voor verschillende gassen, moet men het laser ontwerp aanpassen voor langere golflengtes. In hoofdstuk 4 tonen we aan dat, ondanks de mindere performantie door de lagere technologische status, gas spectroscopie nog altijd haalbaar is met deze apparaten. Naast de spectroscopische toepassingen, kan men fotonisch geïntegreerde circuits ook gebruiken in afstandsmetingen. In hoofdstuk 5 demonstreren we met een opstelling in hoeverre een mode-locked laser in combinatie met een VIPA spectrometer kan worden gebruikt om meteorologische data te verkrijgen via een enkele camera afbeelding. Dit hoofdstuk sluit ook de studie van monolitisch geïntegreerde laser bronnen af in dit doctoraatswerk.
Naast on-chip lasers, onderzoekt dit doctoraatswerk ook vezel-gebaseerde frequentie comb lasers. Aangezien de repetitie frequentie veel lager is dan wat men typisch terugvindt bij geïntegreerde gepulste lasers, zal de overeenstemmende mode-spacing in het frequentiedomein andere vereisten opleggen voor de spectrometer. Aan de andere kant laat een dichtere en bredere spectrale dekking toe om spectroscopie te doen over een breder bereik van absorptielijnen. In hoofdstuk 6 introduceren we frequentie comb lasers en de VIPA spectrometer. De combinatie van beide toestellen wordt gebruikt om de temperatuur van CO_2 te bepalen door te kijken naar zijn absorptiegedrag. Gelijkaardige metingen werden uitgevoerd in omgevingslucht en worden samengevat in hoofdstuk 7. Door de lage CO_2 concentratie in omgevingslucht is een heel lange padlengte nodig. In hoofdstuk 8 demonstreren we een geoptimaliseerde setup om de stabiliteit te verbeteren van de methode die in hoofdstuk 6 werd geïntroduceerd. De verbeterde setup is veel stabieler in omringende fluctuaties en is draagbaar, hetwelk metingen toelaat buiten het laboratorium.

In het laatste hoofdstuk, hoofdstuk 9, vatten we de resultaten samen van al de experimenten en bediscussiëren we welke impact deze resultaten kunnen hebben op toekomstige toestellen die gebruik maken van de gepresenteerde methoden.

1

INTRODUCTION

Spectroscopy is a rather young science, has emerged in the 17th century. The term spectrum was coined by Newton, who separated the colours of white light with the help of a prism[1]. Newton's explanation was based on the assumption that light consists of a stream of small elastic, weightless particles, *corpuscles*, that travel in straight lines. For many spectroscopic experiments this theory was sufficient, but it was abandoned when it failed to explain diffraction, interference, and polarisation. Spectroscopy is the study of the interaction between matter and light[2]. A modern interpretation goes beyond light and includes other kinds of radiation, including particles, acoustic waves, gravity and other interactions. Optical spectroscopy started with the analysis of the electromagnetic spectrum of the sun. Joseph von Frauenhofer improved the resolution and reliability of measurements by replacing the prism with a diffraction grating[3, 4]. While in a prism the dispersion, i.e. the dependence of velocity of the light on the material, was used to separate different wavelengths, the grating makes use of a different mechanism: the interference of waves. The periodical structures in gratings show a wavelength dependent angle for constructive interference[5]. The clear mathematical structure of the underlying theory allowed for quantifying the measurements and did not rely on immeasurable material properties. With the development of a wavelength scale the foundation for spectroscopy was laid. Different light sources and absorbers were investigated. Spectral properties could be linked to chemical elements. Johann Balmer discovered that the four visible lines of hydrogen were part of a series that could be expressed in terms of integers[6]. The spectroscopic measurements triggered the development of the arguably most famous model of the structure of atoms: the Bohr model[7].
From those beginnings spectroscopy has developed into a irreplaceable tool for fundamental research. In astronomy it allows for the determination of the composition of celestial bodies, their gravitational field, velocity, and other parameters[8]. Climate-relevant amospheric gases can be monitored to improve current climate models[9]. It found applications in farming and agriculture, where the quality of fruits or the fat content in meat can be spectroscopically determined[10, 11]. In the medical sector the human breath allows for a non-invasive testing for diseases[12–14]. *In* and *ex vivo* mea-

surements on tissue can detect cancerous cells[15].
These advances have only been possible due to the improving instrumentation and methods that developed alongside with applications. These improvements include increasing the capabilities of direct absorption spectroscopy, but also finding new concepts, such as Raman spectroscopy or indirect methods such as photoacoustic spectroscopy[16, 17]. While new interferometers, e.g. the Michelson interferometer and the Fabry-Pérot etalon, could achieve remarkable resolving powers, the development of the laser allowed for a new approach with unprecedented accuracy[18–20]. Interference based spectrometers had to be designed around the trade-off between resolution and ambiguity range, the so called free spectral range[5]. With the availability of a tunable coherent light source, e.g. a tunable diode laser, spectroscopic measurements could be both, broadband and accurate. In such a setup the laser output would be swept over the absorption lines and detected with a broadband detector, e.g. a photodiode. Due to the intrinsic coherence of single mode lasers, such systems are suitable for long propagation ranges. The downside of this approach is that the spectrum cannot be taken in a single shot. While in a classical broadband light source coherence and bandwidth are competing quantities, the development of the frequency comb provided a tool that can be both[21]. A frequency comb is a composition of multiple narrow linewidth laser lines with strictly defined spectrum and phase conditions between the lines. The resulting comb structure in the spectral domain is responsible for its name. A frequency comb has the ability to probe many different wavelengths simultaneously without the lack of coherence classical broadband light sources suffer from.
Apart from spectroscopic studies frequency combs and single mode lasers found applications in long distance metrology[22, 23]. Those measurements already reached accuracies, at which the variation of the refractive index of air is limiting[24, 25]. Relative accuracies of 10^{-7} and 10^{-8} have been reported using single mode lasers and frequency combs respectively. Two colour schemes to compensate for refractive index uncertainty were applied[26–28]. An alternative is determining the refractive index of air while taking the measurement. If the composition, pressure, and temperature are known, the refractive index of air can be calculated with Edlén's equation[29, 30]. Since its initial installation Edlén's equation has been continously updated and modified[31]. Among the parameters mentioned before, temperature shows the strongest local variations[32]. Therefore temperature sensors are commonly placed along the beam path. Classical thermometers are localised in nature, and can be based on density changes of a liquid, expansion of a solid, the change of thermal radiation as in a pyrometer, or changes in the electrical conductivity of a metal, semiconductor or insulator. While they come with different drawbacks and accuracies, all methods have one feature in common: the data are obtained in a single point in space. Retrieving line or volumetric data requires placing a whole array of detectors in or close to the region of interest. In contrast to classical temperature sensors, a spectroscopical temperature measurement provides integrated line data along the beam path. When combined with optical long distance measurement, the same beam can be used for temperature determination as well as for the length measurement, in which case the temperature is not just measured in the vicinity of the beam, but directly on the beam path. Since distance measurements tend to read out the phase, the temperature measurement should utilise amplitude changes, or absorption,

of the medium propagated through. Suitable gases for such absorption measurements in atmospheric air are O_2 and CO_2, since both show absorption lines in the visible and near infra-red wavelength range[33]. O_2 has a larger abundance in air and absorbs visible light. Diode laser-based setups obtained accuracies of 7 mK[34]. In those measurements line ratios of O_2 lines were compared for different temperatures. When analysing data over several wavelengths, composition and temperature can be obtained simultaneously, as each absorption line has a different temperature dependence.
Fiber-based optical frequency combs need to apply wavelength conversion methods, such as second harmonic generation, to access those wavelengths as their emission lies in the near infra-red region. Ti:Saph oscillator-based frequency combs reach visible wavelengths, but show, due to their lack of integration, limited performance if a portable setup is required. Portability is a requirement for outdoor long distance metrology. CO_2 on the other hand shows strong absorption in the emission range of Erbium doped fiber lasers, which can be fully integrated and relatively independent of the measurement environment. As a consequence those fiber-based lasers are great candidates for portable setups. CO_2 measurements have already been reported by Farooq et al. using diode laser absorption measurements at 2.7 µm wavelength[35]. These experiments have been conducted for the high temperatures of combustion gases and are not a good representation of regular ambient air conditions. Recent publications show an interest to expand spectroscopic temperature measurements in CO_2 to lower temperatures[36]. For climate research several applications focus on identifying the concentration of CO_2 in air; the techniques used there can also be used for determining the temperature, assuming the concentration can be obtained from a different channel. Measurements over path lengths of 2 km have already been reported[9]. Unfortunately water vapour has absorption lines that overlap with CO_2, which means that care has to be taken to select suitable lines without overlap. The water content in air is another quantity that allows for strong local variations.
While fiber-based setups for distance metrology already have the benefits of an integrated device, the long cavity length of frequency combs and mode-locked lasers results in a very low repetition rate. As a consequence the mode spacing of such laser sources is relatively small, imposing high resolution requirements on the spectrometer that is used to read out the data. Integrating the mode-locked laser on a chip results in a shorter cavity lenth and hence a larger mode spacing. If this spacing is larger than the resolution of the spectrometer, the lasing modes can be separated. The interference can be analysed for each individual mode, allowing for measurements with a large range of non-ambiguity. The measurement accuracy for the distance determination can be independent from the resolution of the spectrometer, as long as individual modes can be resolved and the mode spacing is known.
This work is aimed towards showing the possibilities and applications of spectroscopy at near infra-red wavelengths. Several different laser systems were studied. Experiments were conducted with fiber based frequency comb lasers, or monolithically integrated lasers. The frequency comb laser and tunable single mode on-chip lasers were employed for gas spectroscopy. A monolithically integrated mode-locked laser was investigated regarding its feasibility for high accuracy distance metrology. Due to the optical integration the presented setups are portable and can be applied on site, which is a necessary step

to find real spectroscopic applications outside of laboratory conditions.

1.1. INTEGRATED OPTICS

In the second half of the last century electronics followed a trend of increasing integration and miniaturisation. This is most commonly expressed by referring to Moore's law[1], which predicted an exponential growth for the number of components on integrated circuits[37]. More specifically the amount of components per integrated circuit should double every year for at least a decade, i.e. from 1965 to 1975 and beyond. In 1975 this predicted growth has been readjusted to doubling every two years. This rate held steady for roughly 30 years, with the growth slowing down in the following years[38].
In the same way electronic circuits improved, the field of integrated optics is attempting to meet the expectations of exponential growth. An increasing amount of materials and devices is investigated to achieve the same functionalities in integrated optics as the bulk optics counterparts. In a first step of integration, fiber-based lasers found their applications and are currently a well-established technology[39]. Further integration would result in lasers and spectrometers on a chip. Chapters 2, 3, and 4 will describe the design process as well as the applications in spectroscopy for such an on-chip laser. As part of the same project on-chip spectrometers have been developed by our collaborators[40].

1.2. FREQUENCY COMB TECHNOLOGY

A frequency comb is a merger between two regimes: ultrafast and ultrastable. In the time domain pulses in the femtosecond range are produced. Research led to the development of shorter and shorter pulses, reaching attoseconds in the recent years. As short-lived as the light pulses are in the frequency domain, they show remarkable stability in the frequency domain. A frequency comb is composed out of a set of strictly defined narrow lines with fixed distance and absolute positions[21]. While pulses are only femtoseconds long[2], each consecutive pulse is a duplicate of the former one. As a merger of both regimes the frequency comb quickly found ample applications of which only a few will be outlined in this work[42]. Chapters 6, 7, and 8 are meant to introduce direct frequency comb spectroscopy and highlight the importance of this technique for long distance metrology. Frequency combs are likely to replace current frequency standards in the coming years and are therefore a technology a scientist cannot afford to miss[43].

Frequency comb technology and integrated optics are not disjoint fields. While fiber based frequency combs are already commercially available, modern research is tackling the final hurdles for creating fully integrated, i.e. on-chip, frequency comb lasers. A step towards this can be found in the development of integrated mode-locked lasers[44]. The feasibility of mode-locked lasers for distance measurements has already been shown[45]. In Chapter 5 we investigate the possibility of using an on-chip laser for metrologic measurements.

[1] Despite its name, Moore's law is not a physical or natural law, but rather an extrapolation or prediction.
[2] They are femtoseconds long in the lasers used throughout this thesis. Modern research is determined to develop even shorter laser pulses, approaching attosecond pulse durations. Durations as short as 43 as have been reported recently[41].

Another interesting side route of frequency comb research are microcombs, which create the broad discretised spectrum of a comb by making use of the nonlinear interactions of single mode lasers on e.g. microtoroids. Nonlinear effects create side modes of the incident light with a spacing defined by the geometry of the optical microcavity. Subsequent phase control allows for the creation of a frequency comb[46]. This line of research has not been investigated in this work.

REFERENCES

[1] I. Newton, *A Letter of Mr. Isaac Newton, Professor of the Mathematicks in the University of Cambridge; Containing His New Theory about Light and Colors: Sent by the Author to the Publisher from Cambridge, Febr. 6. 1671/72; In Order to be Communicated to the R. Society,* Philosophical Transactions **6**, 3075 (1671), http://rstl.royalsocietypublishing.org/content/6/69-80/3075.full.pdf+html .

[2] D. W. Ball, *Field Guide to Spectroscopy* (SPIE Press, 2006).

[3] J. Fraunhofer, *Bestimmung des Brechungs- und des Farbenzerstreungs-Vermögens verschiedener Glasarten, in Bezug auf die Vervollkommnung achromatischer Fernröhre,* Annalen der Physik **56**, 264 (1817).

[4] J. Fraunhofer, *Kurzer Bericht von den Resultaten neuerer Versuche über die Gesetze des Lichtes, und die Theorie derselben,* Annalen der Physik **74**, 337 (1823).

[5] B. E. A. Saleh and M. C. Teich, *Grundlagen der Photonik* (WILEY-VCH, 2008).

[6] J. J. Balmer, *Notiz über die Spectrallinien des Wasserstoffs,* Annalen der Physik **261**, 80 (1885).

[7] N. Bohr, *XXXVII. On the constitution of atoms and molecules,* Philosophical Magazine Series 6 **26**, 476 (1913), http://dx.doi.org/10.1080/14786441308634993 .

[8] J. Brand, *Lines of Light: The Sources of Dispersive Spectroscopy, 1800-1930* (Gordon & Breach Publ., 1995).

[9] G. B. Rieker, F. R. Giorgetta, W. C. Swann, J. Kofler, A. M. Zolot, L. C. Sinclair, E. Baumann, C. Cromer, G. Petron, C. Sweeney, P. P. Tans, I. Coddington, and N. R. Newbury, *Frequency-comb-based remote sensing of greenhouse gases over kilometer air paths,* Optica **1**, 290 (2014).

[10] B. M. Nicolaï, K. Beullens, E. Bobelyn, A. Peirs, W. Saeys, K. I. Theron, and J. Lammertyn, *Nondestructive measurement of fruit and vegetable quality by means of nir spectroscopy: A review,* Postharvest Biology and Technology **46**, 99 (2007).

[11] S. Hanf, R. Keiner, D. Yan, J. Popp, and T. Frosch, *Fiber-enhanced raman multigas spectroscopy: A versatile tool for environmental gas sensing and breath analysis,* Analytical Chemistry **86**, 5278 (2014).

[12] M. J. Thorpe, D. Balslev-Clausen, M. S. Kirchner, and J. Ye, *Cavity-enhanced optical frequency comb spectroscopy: application to human breath analysis,* Opt. Express **16**, 2387 (2008).

[13] E. van Mastrigt, A. Reyes-Reyes, K. Brand, N. Bhattacharya, H. P. Urbach, A. P. Stubbs, J. C. de Jongste, and M. W. Pijnenburg, *Exhaled breath profiling using broadband quantum cascade laser-based spectroscopy in healthy children and children with asthma and cystic fibrosis,* Journal of Breath Research **10**, 026003 (2016), adonis, Nandini.

[14] M. R. McCurdy, Y. Bakhirkin, G. Wysocki, R. Lewicki, and F. K. Tittel, *Recent advances of laser-spectroscopy-based techniques for applications in breath analysis,* Journal of Breath Research **1**, 014001 (2007).

[15] K. Kong, C. Kendall, N. Stone, and I. Notingher, *Raman spectroscopy for medical diagnostics - from in-vitro biofluid assays to in-vivo cancer detection,* Advanced Drug Delivery Reviews **89**, 121 (2015).

[16] C. V. Raman, *A change of wave-length in light scattering,* Nature **121**, 619 (1928), history.

[17] Y. H. Wong, R. L. Thomas, and G. F. Hawkins, *Surface and subsurface structure of solids by laser photoacoustic spectroscopy,* Applied Physics Letters **32**, 538 (1978), http://dx.doi.org/10.1063/1.90120 .

[18] A. A. Michelson and E. W. Morley, *On the relative motion of the earth and the luminiferous ether,* American Journal of Science **Series 3 Vol. 34**, 333 (1887), http://www.ajsonline.org/content/s3-34/203/333.full.pdf+html .

[19] A. Perot and C. Fabry, *On the application of interference phenomena to the solution of various problems of spectroscopy and metrology,* Astrophysical Journal **9**, 87 (1899).

[20] T. H. Maiman, *Stimulated optical radiation in ruby,* Nature **187**, 493 (1960).

[21] J. Ye and S. T. Cundiff, *Femtosecond Optical Frequency Comb: Principle, Operation, and Applications* (Springer, 2005).

[22] J. Ye, *Absolute measurement of a long, arbitrary distance to less than an optical fringe,* Opt. Lett. **29**, 1153 (2004).

[23] S. A. van den Berg, S. T. Persijn, G. J. P. Kok, M. G. Zeitouny, and N. Bhattacharya, *Many-wavelength interferometry with thousands of lasers for absolute distance measurement,* Physical Review Letters **108** (2012), 10.1103/physrevlett.108.183901.

[24] M. Cui, M. G. Zeitouny, N. Bhattacharya, S. A. van den Berg, H. P. Urbach, and J. J. M. Braat, *High-accuracy long-distance measurements in air with a frequency comb laser,* Opt. Lett. **34**, 1982 (2009).

[25] M. Cui, M. G. Zeitouny, N. Bhattacharya, S. A. van den Berg, and H. P. Urbach, *Long distance measurement with femtosecond pulses using a dispersive interferometer,* Opt. Express **19**, 6549 (2011).

[26] I. Coddington, W. C. Swann, L. Nenadovic, and N. R. Newbury, *Rapid and precise absolute distance measurements at long range,* Nat Photon **3**, 351 (2009).

[27] J. Guillory, J. P. Wallerand, A. F. Obaton, and C. Alexandre, *Laser diodes based absolute distance meter,* in *Conference on Precision Electromagnetic Measurements (CPEM) 2014* (2014) pp. 490–491.

[28] J. Guillory, R. Šmíd, J. García-Márquez, D. Truong, C. Alexandre, and J.-P. Wallerand, *High resolution kilometric range optical telemetry in air by radio frequency phase measurement,* Review of Scientific Instruments **87**, 075105 (2016), http://dx.doi.org/10.1063/1.4954180, smid.

[29] B. Edlén, *The dispersion of standard air,* Journal of the Optical Society of America **43**, 339 (1953).

[30] B. Edlén, *The refractive index of air,* Metrologia **2**, 71 (1965).

[31] J. C. Owens, *Optical refractive index of air: Dependence on pressure, temperature and composition,* Appl. Opt. **6**, 51 (1967).

[32] R. B. Stull, *An Introduction to Boundary Layer Meteorology* (Kluwer Academic Publishers, 1988).

[33] Harvard-Smithsonian Center for Astrophysics (CFA) and V.E. Zuev Institute of Atmospheric Optics (IAO), *Hitran on the web,* website.

[34] T. Hieta, M. Merimaa, M. Vainio, J. Seppä, and A. Lassila, *High-precision diode-laser-based temperature measurement for air refractive index compensation,* Appl. Opt. **50**, 5990 (2011).

[35] A. Farooq, J. Jeffries, and R. Hanson, *CO_2 concentration and temperature sensor for combustion gases using diode-laser absorption near 2.7 µm,* Applied Physics B **90**, 619 (2008).

[36] A. Klose, G. Ycas, F. C. Cruz, D. L. Maser, and S. A. Diddams, *Rapid, broadband spectroscopic temperature measurement of CO_2 using VIPA spectroscopy,* Applied Physics B **122** (2016), 10.1007/s00340-016-6349-4, cO2.

[37] G. E. Moore, *Cramming more components onto integrated circuits, reprinted from electronics, volume 38, number 8, april 19, 1965, pp. 114 ff.* IEEE Solid-State Circuits Society Newsletter **11**, 33 (2006).

[38] M. Lundstrom, *Moore's law forever?* Science **299**, 210 (2003), http://science.sciencemag.org/content/299/5604/210.full.pdf .

[39] Joint European Platform for Photonic Integration of Components and Circuits (JePPIX), *The jeppix roadmap,* website.

[40] M. Muneeb, A. Vasiliev, A. Ruocco, A. Malik, H. Chen, M. Nedeljkovic, J. S. Penades, L. Cerutti, J. B. Rodriguez, G. Z. Mashanovich, M. K. Smit, E. Tourni, and G. Roelkens, *III-V-on-silicon integrated micro-spectrometer for the 3 µm wavelength range,* Opt. Express **24**, 9465 (2016).

[41] T. Gaumnitz, A. Jain, Y. Pertot, M. Huppert, I. Jordan, F. Ardana-Lamas, and H. J. Wörner, *Streaking of 43-attosecond soft-X-ray pulses generated by a passively CEP-stable mid-infrared driver,* Opt. Express **25**, 27506 (2017).

[42] J. L. Hall, *Optical frequency measurement: 40 years of technology revolutions,* IEEE Journal of Selected Topics in Quantum Electronics **6**, 1136 (2000).

[43] S. A. Diddams, J. C. Bergquist, S. R. Jefferts, and C. W. Oates, *Standards of time and frequency at the outset of the 21st century,* Science **306**, 1318 (2004), http://science.sciencemag.org/content/306/5700/1318.full.pdf .

[44] S. Latkowski, V. Moskalenko, S. Tahvili, L. Augustin, M. Smit, K. Williams, and E. Bente, *Monolithically integrated 2.5 ghz extended cavity mode-locked ring laser with intracavity phase modulators,* Opt. Lett. **40**, 77 (2015).

[45] K. Minoshima and H. Matsumoto, *High-accuracy measurement of 240-m distance in an optical tunnel by use of a compact femtosecond laser,* Appl. Opt. **39**, 5512 (2000).

[46] P. Del'Haye, A. Schliesser, O. Arcizet, T. Wilken, R. Holzwarth, and T. J. Kippenberg, *Optical frequency comb generation from a monolithic microresonator,* Nature **450**, 1214 (2007).

2

Design and Testing of an Integrated Optical Single-Mode Laser for Absorption Measurements

The design process for an intracavity filter and the concept of generic photonic integration are explained. A simple linear theory is applied to determine the lasing wavelength. Measurements show at which points the design worked, and where it failed. To facilitate the process of understanding, resonators, active media, and lasers are briefly introduced.

2.1. INTRODUCTION

There are two main building blocks which go into making a laser: an active medium and a feedback mechanism. Having a feedback system but no active medium results in a resonator, such as a Fabry-Pérot interferometer. In such a resonator the incident light is reflected multiple times by the reflective surfaces and the interference of incoming and reflected beams will result in an at first glance unintuitive transmission behaviour. Especially the fact that two (nearly) perfect reflectors can achieve full transmission is counter-intuitive. This is accompanied by an enhanced field inside the resonator. Section 2.2 begins this chapter with the introduction to Fabry-Pérot interferometers.
A resonator is, as mentioned before, just one requirement for building a laser. Laser operation without some kind of active medium is impossible[1]. The active medium amplifies incoming light by the process of stimulated emission. This process is firmly linked to the laser, as it is part of its acronym: light amplification by stimulated emission of radiation. The list of active media includes gases, dyes, and crystals, but is by no means exhaustive. A great fraction of the effort for extending the 1.55 µm generic photonics platform used in this project to longer wavelengths consisted of creating an active medium capable of providing gain in the new wavelength region. This generic platform, namely COBRA[2], and the reasons for choosing it, will be introduced in Section 2.5. Stimulated emission is not sufficient to explain laser operation. In addition to stimulated emission, spontaneous emission needs to be understood, which can create photons randomly within the gain bandwidth of the active medium, resulting in light emission even when not triggered by an external light source. Section 2.3 will be devoted to the explanation of these effects.
When combining both, gain and resonance, or active medium and feedback mechanism respectively, the resonance can become critical, effectively creating a laser. Increasing the gain beyond the threshold would lead to an infinitely increasing light field, which sets the limit for what can be described when simply linearly adding fields. The lasing threshold or lasing condition however can still be found in a linear theory. More about this will be explained in the section about laser principles (Section 2.4).
Filters can block or absorb certain wavelengths and be transmitting for others. While this alone already has applications, the dynamics become especially interesting when inserting such filters in resonant laser cavities. How this can be used to tune a single-mode laser will be explained in the final sections of this chapter, starting from Section 2.6.

2.2. FABRY-PÉROT RESONATORS

A Fabry-Pérot interferometer is an optical resonator made of a transparent plate with a mirror coating on both sides, or two parallel highly reflective mirrors. The former is commonly called etalon, but the terminology is not used consistently in literature. Especially in laser physics the term Fabry-Pérot resonator is used. The instrument is named

[1] An exception to this is the Free Electron Laser, which uses an entirely different physical phenomenom to radiate light.
[2] Communication Technology: Basic Research and Applications

after Charles Fabry and Alfred Pérot[3], its inventors[1]. Examples of optical resonators are shown in Figure 2.1.

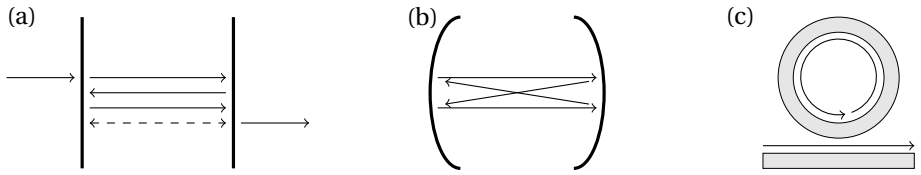

Figure 2.1: Three examples of optical resonators; (a) Fabry-Pérot resonator, (b) curved mirror resonator, and (c) ring resonator

2.2.1. PROPAGATING WAVE APPROACH

There are several ways of describing Fabry-Pérot interferometers; two will be presented here. For the first approach we consider a plane wave hitting a flat glass plate from the left side, such as in Figure 2.2. The plate is assumed to be homogeneous, isotropic, and thin enough to ignore effects of limited coherence of the light. The optical response of the glass is assumed to be linear. If the incident beam is perpendicular to the surface, a scalar wave optical approach is sufficient to describe the system. For angled incidence the field should be separated into TM/TE[4] or s/p[5] polarisation and solved independently. We will segment our wave propagation into pieces using r_1 and r_2 to describe the reflection at the interfaces 1 and 2; t_1 and t_2 for the transmission through the same interfaces and l for the propagation. To simplify the model we assume a piece-wise homogenous, linear, and isotropic medium. In that case l is identical for both forward and backward moving beam. For a propagation length L this would result in $l = \exp(i\beta L)$ with $\beta = n_{\text{eff}}\frac{2\pi}{\lambda}$ being the propagation constant, accomodating for phase changes and losses. An impinging light field E_0 will have a field of $t_1 \cdot E_0$ after transmission through the interface. The derivation of the reflected field is identical to the derivation of the transmitted field, and will not be shown here. The light has to pass through the enclosed medium and the interface on the opposite side resulting in the transmitted field $E_1 = E_0 \cdot t_1 \cdot l \cdot t_2$. This field will interfere (we assume the light to be sufficiently coherent) with light that gets reflected back and forth within the cavity to generate the transmitted field $E_2 = E_0 l^3 r_2 r_1 t_2$. Figure 2.2 visualizes this more detailed. When continuing with this process the pattern of

$$E_{n+1} = E_0 t_1 t_2 l \left(r_1 r_2 l^2\right)^n, \quad n \in \mathbb{N}_0 \tag{2.1}$$

[3] The complete names are Maurice Paul Auguste Charles Fabry and Jean-Baptiste Alfred Perot, although not stated as such in the publication. Perot himself chose to spell his last name as Pérot.

[4] TM = transverse magnetic, TE = transverse electric

[5] s stands for German *senkrecht* (perpendicular) and p for *parallel* to the plane of incidence on a surface

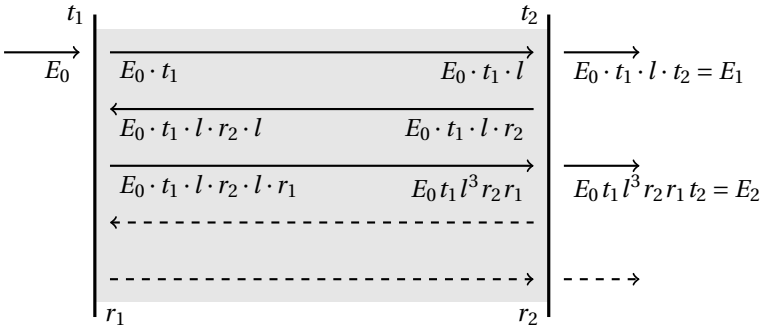

Figure 2.2: The electric field inside and outside a Fabry-Pérot resonator

emerges. The total field at the output side of the interferometer is a superposition of all fields E_{n+1}.

$$E_{\text{total}} = \sum_{m=1}^{\infty} E_m = E_0 t_1 t_2 l \sum_{n=0}^{\infty} \left(r_1 r_2 l^2\right)^n. \tag{2.2}$$

This corresponds to the geometric series and it converges as long as $\left|r_1 r_2 l^2\right| < 1$[2]. We can rewrite Equation (2.2) as

$$E_{\text{total}} = E_0 t_1 t_2 l \frac{1}{1 - r_1 r_2 l^2}. \tag{2.3}$$

All quantities used can be complex valued and can be separated in amplitude and phase, i.e. $z = |z| \exp(i\varphi_z)$. Non-real values for t_1 and t_2 result in a phase offset in E_{total}, but complex values for l, r_1, and r_2 have a more interesting effect. For this we calculate $|E_{\text{total}}|^2$.

$$|E_{\text{total}}|^2 = |E_0|^2 |t_1 t_2 l|^2 \frac{1}{1 + |r_1 r_2 l^2|^2 - (r_1 r_2 l^2 + c.c.)}. \tag{2.4}$$

With $A + A^* = 2\text{Re}(A) = 2|A|\cos(\varphi_A)$ it follows that $\varphi_{r1} + \varphi_{r2} + 2\varphi_l = n \cdot 2\pi$, with $n \in \mathbb{Z}$ implies maximum transmission and $\varphi_{r1} + \varphi_{r2} + 2\varphi_l = (2n+1) \cdot 2\pi$ implies minimum transmission. $E_{\text{total}} \to \infty$ for $r_1 r_2 l^2 \to 1$, which can be understood as the threshold condition for laser operation.

2.2.2. Round-trip model

Another treatment for the resonator is using equations for the forward and backward propagating field in the resonator and defining suitable boundary conditions for both fields, as done in [3]. We will use $a(z)$ for the forward and $b(z)$ for the backward field. $a(z = L) = l \cdot a(z = 0)$ and $b(z = L) = b(z = 0)/l$ when using the same notation as before. The boundary conditions are

$$a(z = 0) = r_1 b(0) + t_1 E_0, \tag{2.5}$$

$$b(z = L) = r_2 a(L). \tag{2.6}$$

The transmitted field is $E_{\text{total}} = t_2 a(L)$. The solution to this is identical to Equation (2.3).

2.2.3. IMPORTANT QUANTITIES

A certain set of parameters have been established that allow for a proper comparison of different resonators. An obvious important quantity is the resonance frequency. Another important quantity is the mode separation ν_F, or the Free Spectral Range (FSR). When the mode linewidth is known, derived quantities such as the finesse $\mathscr{F}$ can be introduced. When considering lossless propagation within the resonator it can be defined as

$$\mathscr{F} = \frac{\pi\sqrt{R}}{1-R} \approx \frac{\nu_F}{\delta\nu},$$

with $R = |r|^2$ as the reflection coefficient for the intensity[4]. In this case mirrors with identical reflection and transmission properties were assumed. It is possible to include the propagation losses by reducing the reflectivity of the mirrors creating an effective reflectivity [6]. A typical transmission curve of a Fabry-Pérot resonator is shown in Figure 2.3.

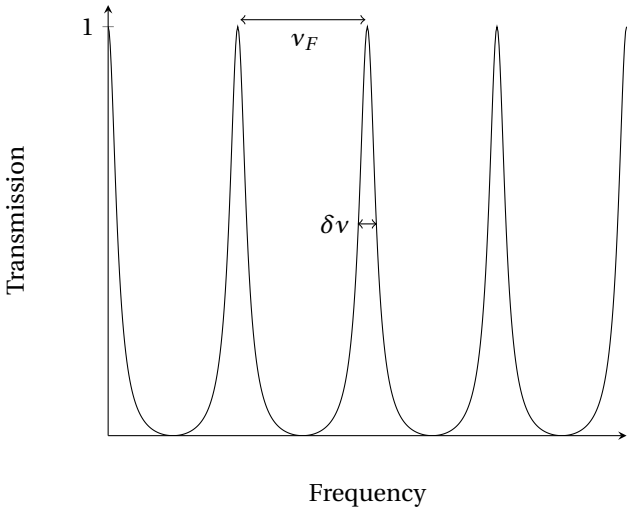

Figure 2.3: Typical transmission profile of a Fabry-Pérot resonator. In the lossless case a transmission of 1 can always be reached if the phase conditions are met, independent of the strength of the mirrors. A transmission of 0, i.e. full reflection, is only possible for perfect mirrors.

In addition to the finesse the *Q-factor* is commonly used. The definition is

$$Q = 2\pi \frac{\text{stored energy}}{\text{energy loss per round trip}},$$

[6] In case of nonlinear optics within the resonator the damping of the field can have an influence and cannot always be ignored.

according to [4]. Since the linewidth of a resonator increases with losses (see Equation (2.3)), Q can be related to $Q = \frac{\nu_0}{\delta\nu}$; ν_0 is the central frequency. It can be understood as a dimensionless quantity describing the quality of different resonator types operating at different frequency ranges.

2.3. THE ACTIVE MEDIUM

In its simplest form a laser can be described by a two-level system, such as an ensemble of atoms in an excited state (N_2) or ground state (N_1)[5]. Once population inversion is reached, i.e. $N_2 > N_1$, stimulated emission, or in other words the de-excitation of the atom while emitting an identical photon, dominates over absorption, which is the annihilation of a photon and excitation of an atom from the ground state to a higher state, and lasing can begin. Unfortunately it is impossible to reach sufficient inversion when just considering a two-level system. The creation of inversion with optical and electrical pumping will be covered in the following sections.

2.3.1. OPTICAL PUMPING

When an active medium is optically pumped, incident light at the wavelength λ_1 is absorbed to excite electrons in an atom, molecule, or crystal. The relaxation of this system is supposed to emit light at a different wavelength λ_2. Usually the photon energy of the absorption is higher than of the emission, which corresponds to $\lambda_1 < \lambda_2$.
Figure 2.4(a) shows simplified two level system, containing stimulated emission, absorption and spontaneous emission. N_1 and N_2 denote the number of atoms in state 1 and 2. Here n is the total number of photons in the system. We will stick mostly to the notation and derivation shown in [5]. We modify the equations to only consider a single pass through the active medium.

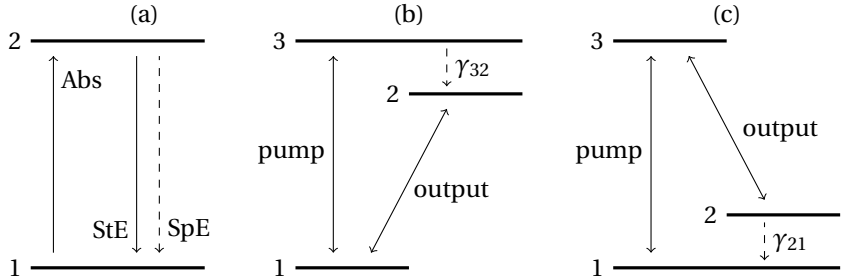

Figure 2.4: Simplified Jablonski diagrams for (a) two-level and (b),(c) three-level systems. The absorption of a photon (Abs) can excite an electron from ground state to the excited state, which can be used to pump the laser. Electrons in the excited state can relax to the ground state by stimulated emission (StE) or spontaneous emission (SpE). The labels γ_{32} and γ_{21} denote fast transitions preventing the pump from the depleting the population inversion.

$$n_{\text{out}} = G(N_{2,\text{in}} - N_{1,\text{in}})n_{\text{in}} + CN_2 + n_{\text{in}} \tag{2.7}$$

$$N_{2,\text{out}} = -G(N_{2,\text{in}} - N_{1,\text{in}})n_{\text{in}} - CN_{2,\text{in}} + N_{2,\text{in}} \tag{2.8}$$

$$N_{1,\text{out}} = +G(N_{2,\text{in}} - N_{1,\text{in}})n_{\text{in}} + CN_{2,\text{in}} + N_{1,\text{in}} \tag{2.9}$$

The index 'out' corresponds to the situation when the light passes through the medium, and 'in' for light entering the medium. From now on those indices will be omitted using the convention that everything on the left-hand side is carrying the index 'out', while everything on the right-hand side has the index 'in'. In these equations G is the gain coefficient for stimulated emission, which is described by $G(N_2 - N_1)n$. The same factor can also be attributed to absorption when $N_1 > N_2$. C is a similar coefficient for spontaneous emission of state 2 into state 1. We neglected non-radiative losses or losses due to radiation into other levels, which are non-existent when having a true two-level system. By virtue of Equations (2.7)-(2.9) using light fields to populate the excited state in a two-level system will stop once $N_2 = N_1$. In a three-level system such as in Figure 2.4(b) light is pumped into state 3, which decays quickly into state 2. This way the pump and the output light operate at different wavelengths. Figure 2.4(c) shows a different three-level system with a short lived lower laser level near the ground state. A combination of both results in a four-level system, which avoids the negative contribution in $G(N_2 - N_1)n$ for both pump and output wavelength.

2.3.2. ELECTRICAL PUMPING

In electrical pumping an electric current is used to excite the medium, instead of photons as in the section before. We will limit the scope of this chapter to doped semiconductors and will not go into the details of quantum structures to tailor the density of states and mode confinement in the active medium. The aim of the reduced treatment is to keep the description of the mechanisms concise despite their great importance in the development of diode lasers. A more detailed discussion of confinement and the density of states can be found in [6–9]. Here we will describe the p-n junction and the use of electron-hole pairs for light emission. Diode lasers allow for very high conversion efficiencies and completely integrated optical circuits, which allowed these lasers to enter everyday life outside of the laboratory environment.

TWO-BAND MODEL

In the two-band model or band gap model a semiconductor consists of a conduction and a valence band. A band corresponds to a selection of possible states for electrons in the crystal. Outside of those bands are *forbidden zones*, the probability for an electron being in this state is zero. The conduction band is the first band not populated by charges (in the natural state of the semiconductor), the valence band is assumed to be completely filled with electrons. A vacant state for an electron is called a hole, whereas holes in the valence band and electrons in the conduction band are considered movable charge carriers[7]. A typical bandstructure for direct band gap semiconductor can be found in Figure 2.5(a). The band gap energy corresponds to the lowest energy difference between

[7] Electrons carry negative charges, holes carry positive charges.

states in the conduction band and states in the valence band. When the minimum of the conduction band and the maximum of the valence band fall on the same crystal wave vector **k** we speak of a direct band gap[8]. Electrons can be moved from the valence band to conduction band leaving a hole (i.e. the absence of an electron) in the valence band. Both together form an electron-hole pair and the interaction between them allows for absorption, stimulated emission and spontaneous emission (see Figure 2.5 (b)-(d)).

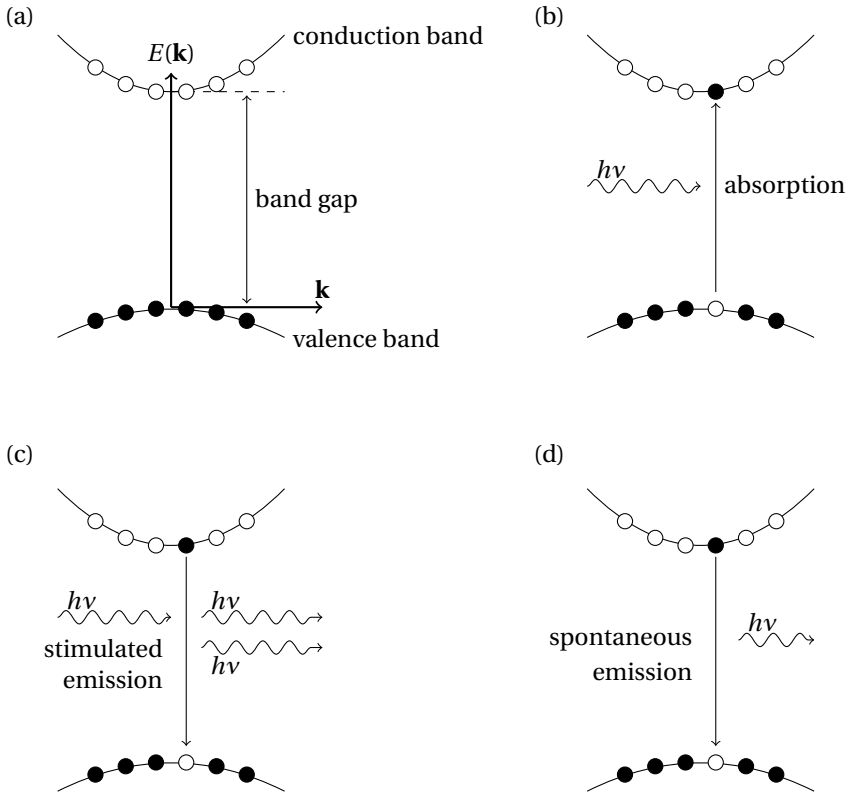

Figure 2.5: (a) Band structure of a semiconductor with direct band gap; holes are marked as hollow circles, electrons as solid circles. **k** corresponds to the crystal wave vector and $E(\mathbf{k})$ denotes the allowed engery levels for a given **k**. (b) An incident photon is absorbed exciting an electron-hole pair, elevating an electron from the ground state to the excited state. (c) An electron-hole pair is hit by a photon of matching energy (and momentum), emitting another identical photon while destroying the pair, moving the electron back into ground state. (d) An electron-hole pair spontaneously decays emitting a photon of corresponding energy.

EFFECTIVE MASS

The potential can be approximated to be parabolic at the critical points giving rise to the concept of the effective mass. An electron at this critical point behaves like a free elec-

[8] The crystal wave vector corresponds to vectors in the reciprocal lattice space and should not be confused with the wave vector in optics.

tron with the effective mass[9] instead of having the real electronic mass[7]. The concept of effective mass is not needed to follow the following derivations and is just listed for completeness. It is sufficient to know that it describes the curvature of the potential in the vicinity of the critical point.

FERMI LEVEL

The probability for an electron to be in a certain state depends on its energy (E) and its temperature and follows the Fermi-Dirac distribution[6, 7]:

$$F(E) = \frac{1}{1+\exp\left(\frac{E-E_F}{k_B T}\right)}. \tag{2.10}$$

For $T = 0$ this equation has a discontinuity at $E = E_F$. For $T \neq 0$ it implies, that if there is a state at the Fermi-level, the probabilty for an electron to occupy said state is 50% (i.e. $F(E_F) = \frac{1}{2}$ for $T \neq 0$). In Equation (2.10) $k_B = 8.6173303(50) \cdot 10^{-5}\,\text{eV/K}$ is the Boltzmann constant[10] and E_F is called Fermi energy[10]. A good approximation for room temperature is $k_B T|_{273\text{K}} \approx \frac{1}{40}\,\text{eV}$. In the theoretical case of zero temperature ($T = 0\,\text{K}$) we get

$$F(E)|_{T=0} = \begin{cases} 1, & \text{if } E < E_F \\ 0, & \text{if } E > E_F \end{cases}.$$

In a semiconductor such as in Figure 2.5 the Fermi energy is in the band gap region. The Fermi level is the Fermi energy for $T = 0$, that means the point up to which all electronic states are filled[11]. The Fermi energy is a material property and can be influenced by doping.

DOPING

Doping in solid state physics means introducing defects or impurities into the semiconductor to change the electrical properties. In this way allowed states within the band gap are created, commonly very close to the valence or conduction band, depending on the dopant type. In a p-type semiconductor the concentrations of holes is increased, moving the (effective) Fermi level closer to the valence band. An n-type semiconductor has a higher concentration of electrons (*majority carriers*) than holes (*minority carriers*) resulting in a higher Fermi level (that means closer to the conduction band).

P-N JUNCTION

Both p- and n-doped semiconductors are of neutral total charge, but the majority and minority carriers can be moved. This allows for interesting effects when both are brought together. A diffusion of carriers in the region of higher concentration to the region of lower concentration will set in; electrons will move from the p- to the n-region and vice versa for holes. This charge separation will create an electric field at the junction, which

[9] Although being called *mass* it is not a scalar quantity, but a matrix.

[10] Due to $E = h\nu$ and $c = \nu\lambda_0$ energies in eV can be converted into wavelengths by $E[\text{eV}] = \frac{1.24}{\lambda_0[\mu\text{m}]}$ [8]

[11] Depending on the literature the notations for Fermi energy and Fermi level are interchanged. To avoid confusions one can use the term *chemical potential* for $T \neq 0$ and Fermi level/energy for $T = 0$.

tends to *pull* those charges back towards their initial position. Both effects are counteracting and eventually an equilibrium will be established. An electric field automatically results in an electric potential (see Figure 2.6 for a graphical explanation). A depletion zone will build up, where the number of free charge carriers is strongly reduced.

Photon emission requires a high amount of electrons and holes to be present at the same region, such that they can recombine. An n-doped semiconductor contains an increased amount of electrons, but is lacking holes. A p-doped semiconductor on the other hand lacks electrons while having an increased amount of holes. Both by themselves could not create significant light emission. In the p-n junction, however, both holes and electrons are present, as long as they can pass the barrier separating them. This can be assisted (or hindered) by applying an external electric field.

Homojunctions, heterojunctions, and double heterostructures

So far, interfaces between similar semiconductor materials, i.e. materials with the same band gap, have been described. Such interfaces are called homojunctions. A heterostructure occurs, if the interfacing semiconductors exhibit a different band gap. A double heterostructure has two heterojunctions, e.g. with the smallest bandgap in the center. In such a structure, electrons and holes can be confined to a small region, which is beneficial for laser applications. Figure 2.7 shows examples for both, heterostructures and double heterostructures. Doping can be used to increase the amount of electrons (n-type doping) and holes (p-type doping) in the potential well formed by the double heterojunction. A double heterostructure does not only allow for a better confinement of electron hole pairs, which can provide the optical gain, but can also confine the light, as materials with a lower bandgap have typically a higher refractive index, which can be exploited to create waveguides, as discussed in Section 2.5.1.

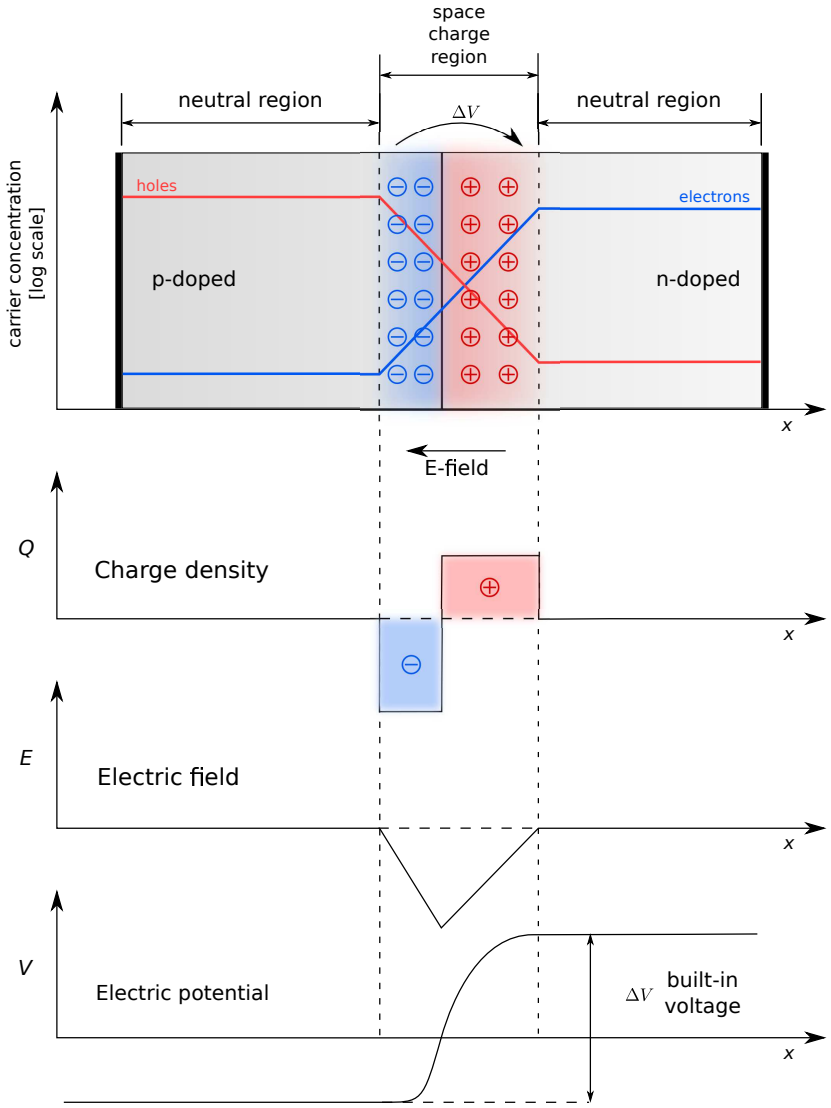

Figure 2.6: Carrier concentration, charge density, electric field and electric potential when p-doped and n-doped semiconductors are brought into contact.
Attribution: This vector image was created with Inkscape by Adundovi. (Own work) [CC BY 3.0 (http://creativecommons.org/licenses/by/3.0) or GFDL (http://www.gnu.org/copyleft/fdl.html)], via Wikimedia Commons

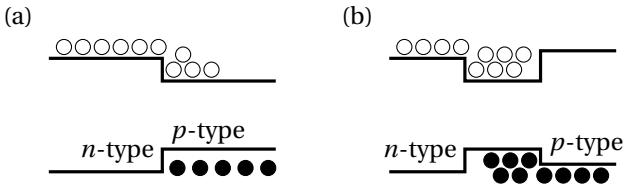

Figure 2.7: (a) Example for a heterojunction, here from n-type to p-type material. Electrons from the n-zone leak into the lower bandgap material. Due to the p-doping in that material, electron-hole pairs can be found near the interface. (b) In this example for a double heterostructure, a lower bandgap material is encapsulated by a higher bandgap material. This creates a potential well, that confines electrons originating from the n-doped zone as well as holes from the p-doped material. The high concentration of electrons and holes allows for effective recombination.

2.4. LASERS

In Section 2.3.1 we were already discussing a two-level system, decscribed by Equations (2.7)-(2.9). The dynamics of the system get more interesting, when the light is kept in the system. As will be shown in this section, laser operation can be achieved. The derivations are based on [5] and can be found there in a more extensive version.

2.4.1. RATE EQUATIONS AND TWO-LEVEL SYSTEMS

We will use the following rate equations for describing the number of photons n passing through a two-level system with N_2 excited atoms and N_1 atoms in ground state:

$$\frac{dn}{dT} = G(N_2 - N_1)n - \frac{n}{T_c}, \tag{2.11}$$

$$\frac{dN_2}{dT} = R_p - \frac{N_2}{T_1} - G(N_2 - N_1)n, \tag{2.12}$$

$$\frac{dN_1}{dT} = -\frac{N_1}{T_1} + G(N_2 - N_1)n. \tag{2.13}$$

As before G is used for the gain coefficient for stimulated emission, T_c is the decay time due to outcoupling or mirror losses, T_1^{-1} are the decay rates for the population levels, and R_p is the pumping rate. Equations (2.11)-(2.13) can be reduced to two equations when considering the population difference, or inversion, $N = N_2 - N_1$ and $N_0 = R_p T_1$ as population difference when no laser light is present.

$$\frac{dn}{dT} = GNn - \frac{n}{T_c} \tag{2.14}$$

$$\frac{dN}{dT} = -\frac{1}{T_1}(N - N_0) - 2GNn \tag{2.15}$$

We convert these equations into dimensionless quantities to make them system independent and obtain a general solution. We need to introduce new variables $I = 2GT_1 n$, $D = GT_c N$ and $t = T/T_c$. In this way I is a measure for the intensity and t for the time. Additionally we define the constants $A = GT_c N_0$ and $\gamma = T_c/T_1$, such that eventually

Equations (2.14) and (2.15) become

$$\frac{dI}{dt} = I(D-1), \tag{2.16}$$

$$\frac{dD}{dt} = \gamma\left(A - D(1+I)\right). \tag{2.17}$$

In the steady state, that means $dI/dt = 0$ and $dD/dt = 0$, we reach

$$I(D-1) = 0 \tag{2.18}$$

$$A - D(1+I) = 0 \tag{2.19}$$

for non-vanishing γ. Two solutions exist, Solution 1 being Equation (2.20) and Solution 2 being Equation (2.21).

$$I = 0 \text{ and } D = A \tag{2.20}$$

$$I = A - 1 \geq 0 \text{ and } D = 1 \tag{2.21}$$

The inequality in Equation (2.21) is the consequence of a non-negative photon number, or intensity respectively. A is a measure for the pump power[12] and lasing is possible for $A > 1$. For $A = 1$ both solutions intersect allowing for a transition from one solution to the other. A stability analysis is given in [5]; here we merely claim that this transition occurs at $A = 1$, which is the lasing threshold for the laser. We will later on interpret such an intensity pattern as an indication for lasing, as seen in Figure 2.8. In [5] the equations are modified by increasing the photon number by one creating a smoother transition.

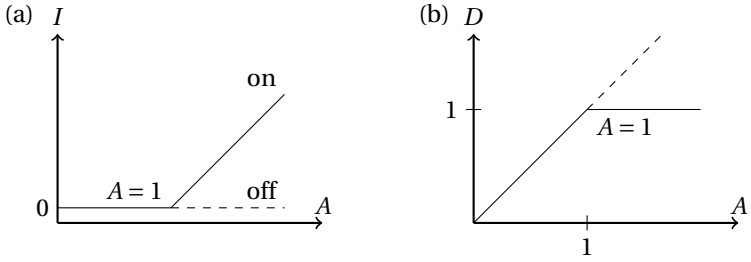

Figure 2.8: Plot of the possible steady state solutions, (2.20) and (2.21). (a) I as a measure for intensity shows the typical behaviour for a laser in the vicinity of its critical point/lasing threshold. (b) The population inversion, repesented by D, clamps at a constant level when laser operation sets in.

2.4.2. INTRA-CAVITY FILTERS

The derivations so far have been done for single wavelength lasers. In reality the gain material does not support only a singular frequency, but a finite bandwidth. Carefully introducing wavelength-dependent losses can eliminate unwanted wavelengths leaving them below the lasing threshold. Since a laser requires a resonator it only supports a

[12] $A = GT_c N_0 = GT_c R_p T_1$

discrete set of lasing modes, similar to a Fabry-Perot interferometer (see Section 2.2 for reference). The process of placing filters within the cavity is called intra-cavity filtering and enables the selection of a single longitudinal mode.

MACH-ZEHNDER INTERFEROMETER

In a Mach-Zehnder interferometer a propagating wave is split into two parts by a beamsplitter in the case of free space optics. Each of those two parts of the wave travels a different path and both are afterwards recombined again; the phase difference between the fields of both arms of the interferometer determines the output, shown in Figure 2.9(a). Integrated optics provides a similar scheme for the interferometer, replacing beams of light with guided waves and beamsplitters with waveguide couplers[13] such as in Figure 2.9(b). When mirrors are placed in the arms of the Mach-Zehnder interferometer it is effectively converted into a Michelson interferometer, which reflects both arms back to the initial beamsplitter. For both interferometers the output intensity shows a cosine or sine dependence regarding the phase difference of the arms.

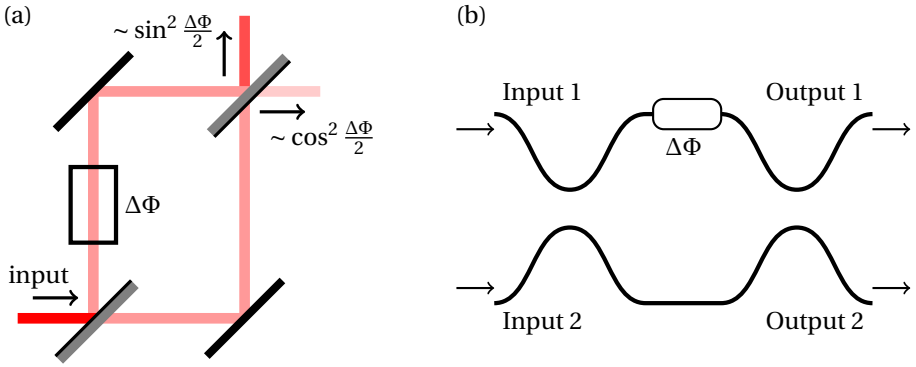

Figure 2.9: Mach-Zehnder interferometer in free space (a) and integrated (b) optics. The directional coupler transfers power from one input into both arms of the interferometer. The energy transfer is due to the overlap of the lobes of the guided modes due to the proximity of the waveguides. They mimick the behaviour of beamsplitters in free space optics. No building blocks for directional couplers were available. As a consequence multimode interference couplers were used instead, which are further explained in Section 2.5.1.

2.5. GENERIC PHOTONIC TECHNOLOGIES

Modern integrated photonics requires a clean room for manufacturing. The maintenance costs for a clean room are very high; so high that small companies targetting only a small set of customers will not have access to it, if it were not for multi-project wafer (MPW) runs. In these runs the idea is that the costs are shared between the projects and the wafer space is divided amongst the project partners. When using generic technologies and limiting the users to already tested building blocks, users get access to high performance structures without getting involved in the details of the clean room work-

[13] Comprehensive material about waveguides and waveguide couplers can be found in [4, 6, 9].

flow[11]. With these advantages in mind the LWAVE-TECH project[14] was started, which aimed to access longer wavelengths with on-chip lasers. First designs were made at 1.55 µm to test their feasibility in a better understood regime. A chip design for a tunable single mode laser was submitted to the 7th MPW run of COBRA. In addition to that a previous design was already submitted to the 6th run, for which functionality could be shown in a publication. We will discuss the chip of COBRA 7 in this chapter and dedicate the subsequent chapter to the description of the COBRA 6 design.
The initial goal of the LWAVE-TECH project was to develop an integrated tunable single-mode laser for gas spectroscopy for *long* wavelengths. It was decided to aim for the 2 µm range. First designs used components at the wavelengths around 1.55 µm, but took a subsequent migration to the longer wavelengths and consequently to a different platform into account. Therefore the used building blocks in each design had to be the basic ones to avoid additional testing of non-standard components when starting the new 2 µm platform. Simpler building blocks can be easier adapted to be suitable for the longer wavelengths.

2.5.1. USED BUILDING BLOCKS

The COBRA platform provides for a set of building blocks, that provide a similar, if not the same, functionality as their counter-part in free space optics. Table 2.1 lists the physical quantities and devices used to control them in the respective field.

Table 2.1: Comparison of optical components in free space optics and integrated optics.

physical quantity	free space optics	integrated optics
phase	delay line	electro-optical phase modulator (EOPM)
gain	active medium	semiconductor optical amplifier (SOA)
power division	beam splitter	multimode interference coupler (MMI)
orientation	mirrors	waveguides
power measurement	photo detector	integrated photodiode
feedback	mirrors	MMI-based integrated reflector (MIR)

WAVEGUIDES

The waveguides provided by the COBRA platform are ridge waveguides, however, the details of the structures are confidential [12]. They are either *deep* or *shallow edge*, referring to the height (h) and width (w) of the ridges (see Figure 2.10). Deep waveguides have a stronger mode confinement and less outcoupling at bends of the waveguide. For a straight waveguide the propagation losses are smaller in the shallow waveguides. In the simplest approach total internal reflection is considered as the guiding mechanism, trapping light with certain propagation angles within the waveguide. The structure can be further simplified when assuming $n_3 = n_2$ and $h_0 = 0$. The next level of complexity is added when solving the field equations for a dielectric slab. For a full understanding

[14] STW 11360-LWAVETECH

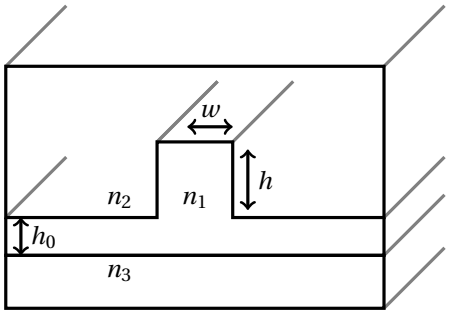

Figure 2.10: Ridge waveguide as used in the COBRA platform. Guided waves exist if the refractive index n_1 is higher as both n_2 and n_3.

a numerical mode solver can be used[13, 14]. Typically waveguide structures are more complex than shown in Figure 2.10, with index variations in the individual segments that have been here summarised as n_1, n_2, and n_3. However, the guiding mechanisms can be understood in the simplified picture.

SEMICONDUCTOR OPTICAL AMPLIFIER

The basic working principles of the semiconductor optical amplifier (SOA) have been explained in Section 2.3. The SOAs in COBRA are InP-based and are part of the same wafer. Passive and active structures can be made in the same process (active-passive integration). The wafer was predefined with active regions in which the SOAs had to be placed in the mask. Later iterations of the multi-project wafer runs do not suffer from this drawback anymore and gain sections can be placed freely on the chip.

MULTIMODE INTERFERENCE COUPLERS

Several coupling concepts exist in integrated optics, such as *arrayed waveguide gratings* (AWG), *directional couplers*, and *multimode interference couplers* (MMI)[15, 16]. Unfortunately no building blocks for directional couplers were provided. While AWGs are also available in COBRA they were not used for the chip designs presented here.
In an MMI the width of a single mode waveguide is increased to allow for multiple guided modes. Soldano and Pennings[16] have shown that due to the different propagation constants of those modes, power can be transfered from the input, e.g. the center of the device, to different output positions, e.g. the sides of the device. Placing waveguides at those maximum positions allows for efficient coupling and in consequence splitting of the initial light. The MMIs used here have a 50:50 splitting ratio among both arms. In case of the 1x2 MMI, one input and two output channels are provided. In contrast to the 2x2 MMI[15] with two input and output channels, light entering with a certain phase condition from side with two ports is lost when leaving the MMI from the side with one port. In the 2x2 MMI the phase conditions determine the power ratio between the output ports.

[15]The first number refers to the amount of input waveguides, the second to the output.

ELECTRO-OPTICAL PHASE MODULATORS

COBRA offers voltage-based phase modulators to be incorporated in the circuits, so called electro-optical phase modulators (EOPM). A constant electrical field interacts with the fast oscillating light field affecting the perceived effective index of refraction. This is based on the Kerr electro-optic effect, which is described in [17]. An easy understanding can be developed when assuming stress on the crystal due to the presence of the electric field. Therefore the waveguide gets compressed/stretched and the light propagates over a shorter/longer distance, changing the accumulated phase. The overall change of the refractive index is a combination of Pockels effect, Kerr effect, carrier-induced electro-optical effects and a modulation of the depletion layer thickness. Details about the contributions of the different effects can be found in [18]. The combination of all effects leads to a refractive index change that scales linearly with the applied voltage up to approximately 10 V.
Similarly changes in the temperature contribute to a change of the chip dimensions. Since the SOAs build up heat when being pumped they can also be used for tuning. This will be exploited in the following two chapters.

ON-CHIP MIRRORS

COBRA allows for angled and straight output port configurations. A straight output port reflects about 30% of the light if not treated with a coating. In an angled output port the reflected light will leave the waveguide and not affect the devices on the chip. In the case of straight output ports the reflected light is fed back into the photonic integrated circuit. It is possible to apply coatings to further optimise the output ports. An anti-reflective coating can prevent unwanted feedback due to the output facet, while a reflective coating can be applied to increase it.
In addition to facet reflections COBRA allowed for on-chip reflectors that could be placed anywhere on the chip. Those reflectors were called MIRs for MMI-based integrated reflectors. Instead of coupling light out of the MMI it was reflected back to the input ports. For the devices discussed here only 1x0 MIRs, with an identical nomenclature compared to the MMI, were used. In this configuration they are supposed to provide a reflectivity of ≈50% [12, 19, 20]. While not discussed here, 2x0 MIRs have been succesfully used for a different laser design.

INTEGRATED PHOTODIODES

The photodiodes were at an experimental stage at COBRA 7. The design of the integrated laser does not rely on them, but they were included for testing in some circuits. Like SOAs they had to be placed in the pre-defined active regions. When reading out the current in the photodiodes it is possible to evaluate whether the circuit was lasing without any fiber-chip coupling.

2.5.2. USED SOFTWARE

Designs were made using PhoeniX Software[16]. The available building blocks have been transfered into classes in the software. That way designs can be made without knowing the exact mask structure. The chip foundry on the other hand can export all the data

[16] www.phoenixbv.com

needed. That way even confidential devices can be easily embedded in the design. Besides having a communication platform between designers and chip foundry PhoeniX software packages include simulation tools to predict the behaviour of the designs.
It is worth mentioning that COBRA is not the only MPW platform that PhoeniX software is compatible with. The associated foundry can be selected upon installing the software.

2.6. A Mach-Zehnder interferometer based intra-cavity filter for designing a single-mode laser

As already mentioned in the introduction of Section 2.5 a single-mode laser has been designed and submitted to the the 7th MPW of COBRA. The design was based on a series of Mach-Zehnder interferometers. The chip design contained multiple photonic integrated circuits (PICs) testing the multiple possible configurations for the filter layout. The following sections aim to discuss the advantages and disadvantages of the those configurations.

2.6.1. Working principle

A Mach-Zehnder interferometer (MZI) shows a transmission profile $\propto \cos^2(\Delta\varphi/2)$, showing maximum transmission for wavelengths for which the phase difference due to propagation in the different arms $\Delta\varphi = n_{\text{eff}}\frac{2\pi}{\lambda_0}\Delta l = 2\pi \cdot m$, with $m \in \mathbb{Z}$. Changing the length of one arm can tune the transmission of the filter. When comparing the transmission for different wavelengths longer path length differences lead to stronger variations of the phase when varying the wavelength. Due to the $\cos^2(\Delta\varphi)$ dependence of the transmission this corresponds to narrower lines, but with a lower spacing. Increasing the distance of neighbouring maxima by decreasing the path length difference, automatically increases the linewidth of the filter. To select a single laser mode, the filter linewidth has to be small enough to differentiate neighbouring longitudinal modes of the cavity and, at the same time, only support a single transmission line over the whole covered wavelength range of the gain medium.
An easy way out of the dilemma seems to be to just chain a series of those filters in succession. Continuous multiplication of the transmission function narrows the linewidth and keeps the spacing constant, as can be seen in Figure 2.11. Unfortunately this is not helpful when being used as an intracavity filter since it increases the overall length of the laser cavity resulting in more densely spaced longitudinal modes. Those modes are often refered to as Fabry-Pérot modes, since a *cold cavity* laser resonator, i.e. a resonator ignoring the gain medium, is basically a Fabry-Pérot interferometer. It is vital for a single mode laser to sufficiently isolate a single longitudinal mode. Increasing the cavity length reduces the spacing of those modes and decreases the effectiveness of the applied wavelength selective filters.

While simply adding up identical filters does not solve the problem, a set of several interferometers with different path length differences helps. Different path lengths result in different transmission profiles. When combining such filters we can tailor the transmission profile to our needs. The fact that chaining several filters increases the cavity line density remains true. It is therefore needed to keep the number of filters as low as possible while isolating a single line within the whole gain region of the filter. The

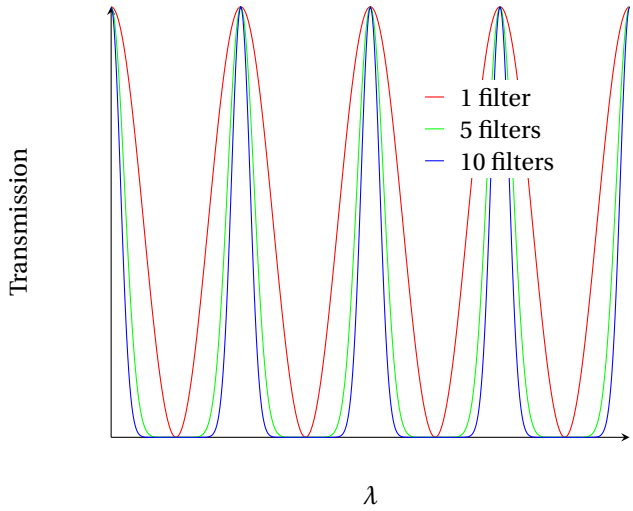

Figure 2.11: Transmission profile after passing through one (red), five (green), and ten (blue) identical Mach-Zehnder interferometers.

demanded wavelength selectivity was achieved using three different MZIs, i.e. with different path length differences, instead of identical ones. The resulting transmission profile can be seen in Figure 2.12. We aimed for single mode operation around 1.55µm and used ASPIC[17] for creating a suitable transmission profile. It has been shown before that several percent transmission difference in the cold cavity case can lead to an acceptable side mode suppression ratio (SMSR) [21]. Acceptable meant 20dB in this case, which was estimated to be enough for gas detection. Since the chip offered enough space for more than one circuit, several different designs were placed on it. The configurations used are shown in Figure 2.13. Additionally designs with 2x2 MMIs were also placed on the chip, routing one exit port to an on-chip photodiode. This was done to test the photodiodes and because the performance of 1x2 MMIs was under discussion at the time when the design had to be submitted. Although the configurations in Figure 2.13 appear very similar, there are notable differences:

- The Michelson configuration can be overall shorter, since the path length in the two arms can be half as long as in the Mach-Zehnder case. This also holds for the needed length of the phase shifters.
- In the Mach-Zehnder configuration the filters are passed twice per round trip, leading to superior filter behaviour while increasing the line density of the Fabry-Pérot modes.
- The Michelson configuration uses four on-chip mirrors. If stable performance of the mirrors cannot be guaranteed deviations might seriously impact the quality of

[17] ASPIC = Advanced Simulator for Photonic Integrated Circuits. It is distributed with the Phoenix software package.

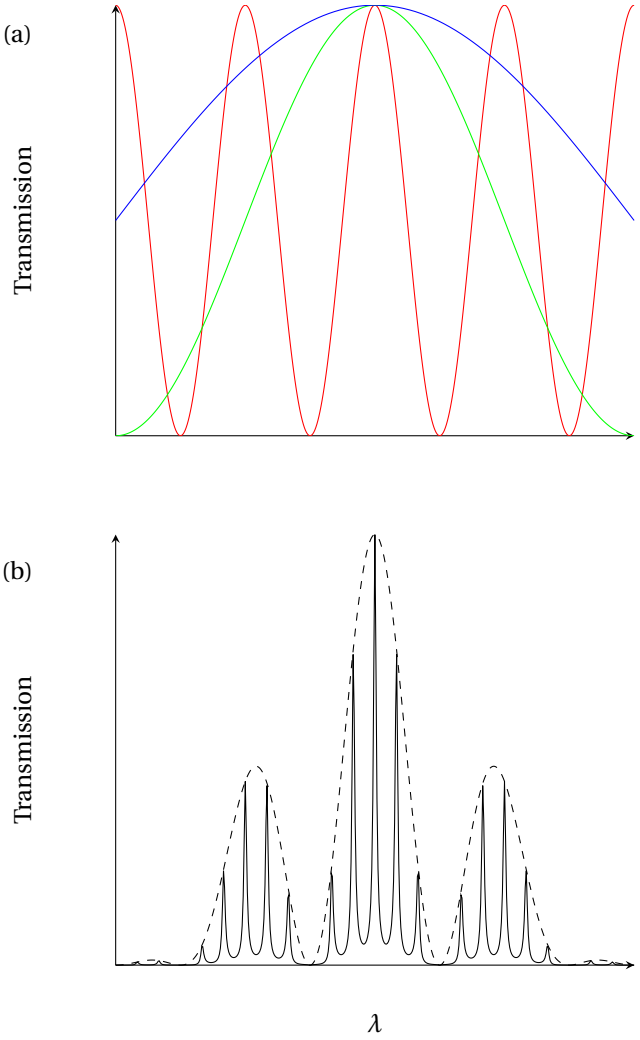

Figure 2.12: (a) Transmission profile of three Mach-Zehnder interferometers, each with their own path length difference. A longer path length difference results in a finer filter, at a cost of a smaller free spectral range. (b) The resulting transmission profile of the combination of the three filters of (a) is displayed as a dashed line. The solid line includes Fabry-Pérot lines as present in a laser cavity.

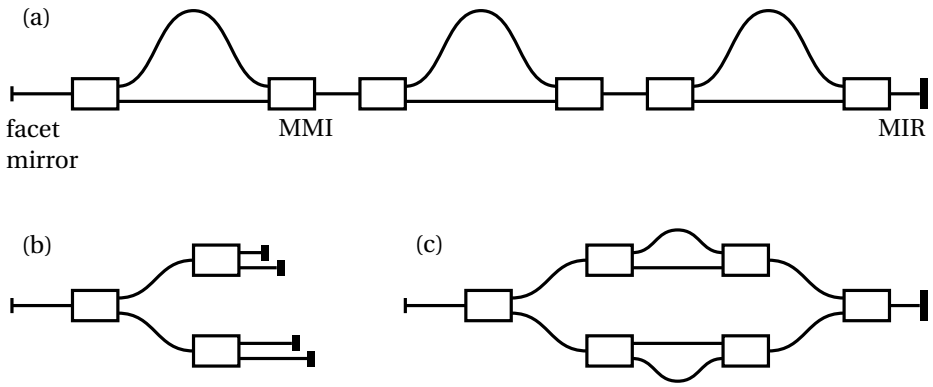

Figure 2.13: The different filter configurations that were placed on the chip CB07_2_3. (a) Serial Mach-Zehnder configuration, (b) Michelson configuration, (c) Nested Mach-Zehnder interferometer.

the filter. The Mach-Zehnder configuration does not suffer from those irregularities.

To tune the filter EOPMs are placed in both arms. That way the imbalance, or optical path length difference of the arms, of the interferometer can be adjusted. As shown before this translates in a change of the wavelength dependence of the transmission.

2.6.2. CB07_2_3 LAYOUT

The chips were manufactured in Eindhoven University of Technology. They were part of the the 7th COBRA multiproject wafer run, hence the serial number CB07_2_3. After the wafer was processed and the chips were delivered to the customers CB07_2_3 stayed in Eindhoven awaiting for mounting and wire bonding. The mount was developed by Sylwester Latkowski, which simplified electrical and optical coupling to the chip as well as cooling it. The electrical contacts were wire bonded to a printed circuit board with D-SUB connectors. Compared to landing a needle probe on the chip it reduced the operation to plug and play. The optical light output was collected with a fiber with tapered tip. Such a fiber tip works similar to a lensed fiber and allows to collect more of the light from the chip. Any light leaving the chip will be strongly diverging due to the strong confinement. The size of the waveguides is in the micrometer regime, the mode field extension is of equal order. The cell size for a chip on the MPW was $4 \times 4.6\,\mathrm{mm}^2$, visible in Figure 2.14. The whole chip including the mount can be seen in Figure 2.15. The dimensions of the devices are listed in Table 2.2.

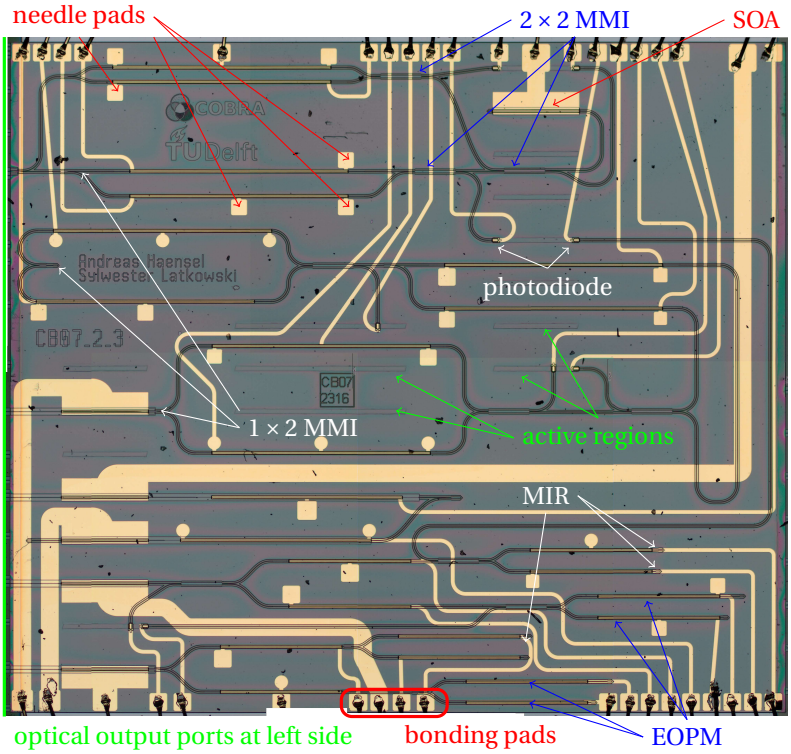

Figure 2.14: Microscope image of the chip several weeks after production. The lines of golden colour are conducting metal layers to get the electrical access ports to the side of the chip. This simplified wire bonding to a printed circuit board (PCB) connector. Thicker lines are for the current driven SOAs, the thinner ones for the photodiodes and EOPMs. The design is constrained by active regions at which the SOAs have to be placed. Waveguides (visible as dark lines) have to be guided around them. Additionally to the bonding pads elements have been provided with needle pads in case the wire bond breaks. Photodiodes have to be placed in the active regions as well.

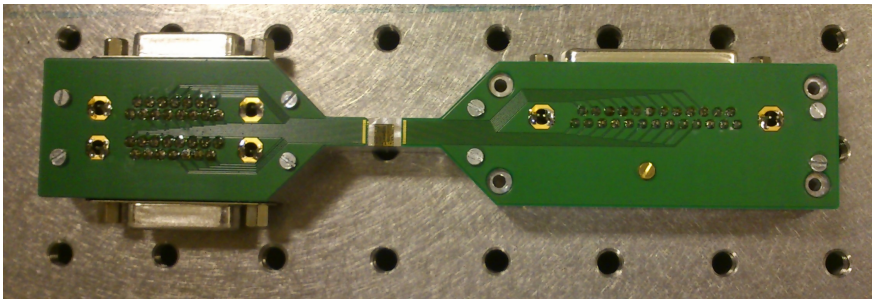

Figure 2.15: CB07_2_3 including the mount. With D-sub connectors the electrical ports can be accessed.

Table 2.2: Important dimensions for reproducing the circuits. Here Δ_n is the path length difference in the n-th filter stage. The effective length differences are twice the stated value, since the light passes through the arms two times.

circuit	element	length [µm]
all	SOA	500
Michelson	EOPM	700
	Δ_1	471
	Δ_2	95
	Δ_3	15.7
Mach-Zehnder	EOPM	1260
serial MZ	Δ_1	1410
	Δ_2	141
	Δ_3	15.7
nested MZ	Δ_1	712.2
	Δ_2	101.6
	Δ_3	14.8

2.6.3. CB07_2_3 PERFORMANCE AND RESULTS

The chips were tested in Eindhoven and Delft to evaluate their performance. Lasing could not be achieved with any of the circuits, a longer gain section seems to needed. When increasing the driving current we would expect a behaviour as predicted in Section 2.4; in our measurements however gain saturation sets in before we get the significant increase in output power. The results were similar for all circuits, we limit the description here to the case of the Michelson configuration. Figure 2.17 shows the corresponding PI diagram (optical power over driving current). The choice of the short SOA sections was due to limitations of the chip layout, most of the active regions available on the chip were of 500 µm size[18]. The tunability of the filter could be verified when driven sub-threshold as shown in Figure 2.16. For this figure we tuned the filter from zero to maximum voltage in 20 steps; the zero-voltage transmission is shown in black, while all the other profiles are plotted in grey. We only show the reduced data set. For the experimental verification of the tunability we scanned with a finer grid. Every wavelength within the design region can be targetted when tuning all the filters simultaneously. Single mode operation can only be shown once lasing has been achieved.
The used equipment for the measurements mentioned in this chapter is listed in Section A.1.1 in the Appendix.

EXTERNAL FEEDBACK

One way to increase the feedback and consequently lower the lasing threshold is to use external feedback, that means coupling part of the light leaving the chip back into the circuit. External feedback allowed as to achieve lasing operation, which was not possible

[18] In the most recent MPW run of the same foundry (although under the new name smartphotonics) wafers do not have pre-defined active regions any more.

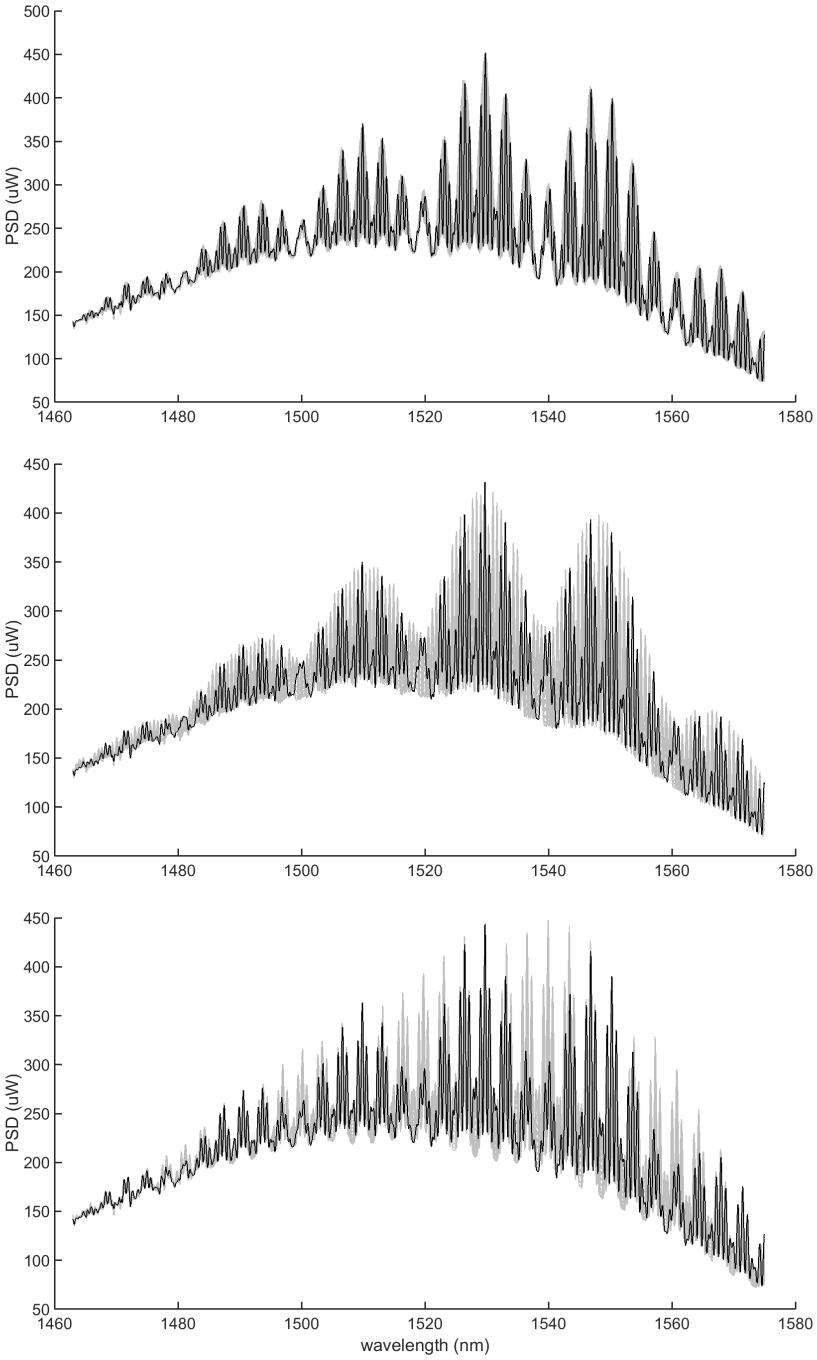

Figure 2.16: Power spectral density (PSD) when applying voltage to the EOPMs of the Michelson filter. The overlay of all spectra over one sweep is plotted in grey, black displays a single measurement. Only one phase shifter per filter was used, consequently the sweeping range can be doubled when using both. Δ_1 is swept for the top picture, Δ_2 for the centre, and Δ_3 for the bottom picture.

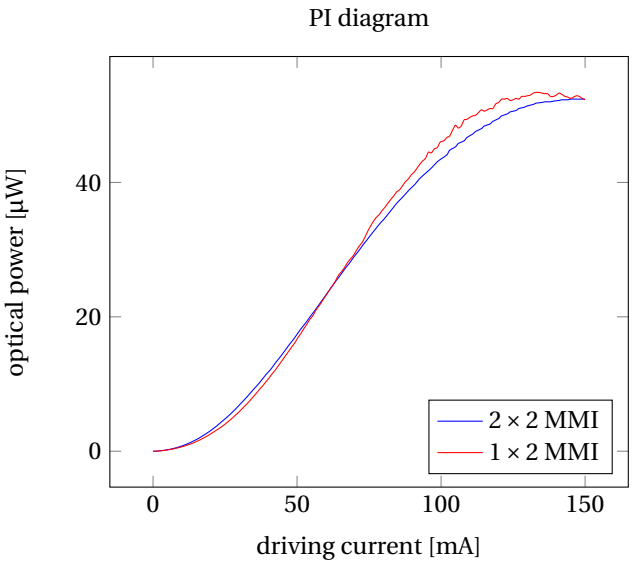

Figure 2.17: Measured optical power over driving current. The gain saturates before lasing could be achieved. The chips were kept at a constant temperature of 18°C during the measurement.

without it. Unfortunately fiber-chip coupling decreases within minutes, making the resulting laser unreliable. Additionally thermal fluctuation and vibrations can lead to very unpredictable coupling and therefore feedback behaviour. We encountered mode jumps in the ~ 10 s time scale and chose to not use external feedback for spectroscopic applications. This can be seen in Figure 2.19, where the coupling got lost during one sweep. A lasing threshold is visible at about 45 mA driving current. A spectrum at a current of 100.81 mA can be seen in Figure 2.20. Proper packaging can reduce the fluctuations and allow the creation of a single mode laser using this device.

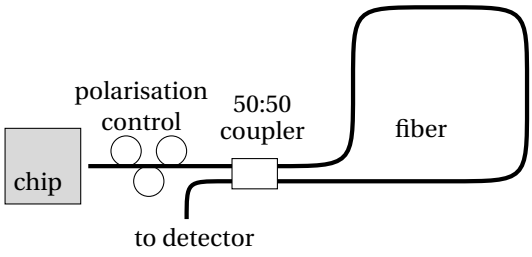

Figure 2.18: Schematic of the setup using external feedback to lower the laser threshold.

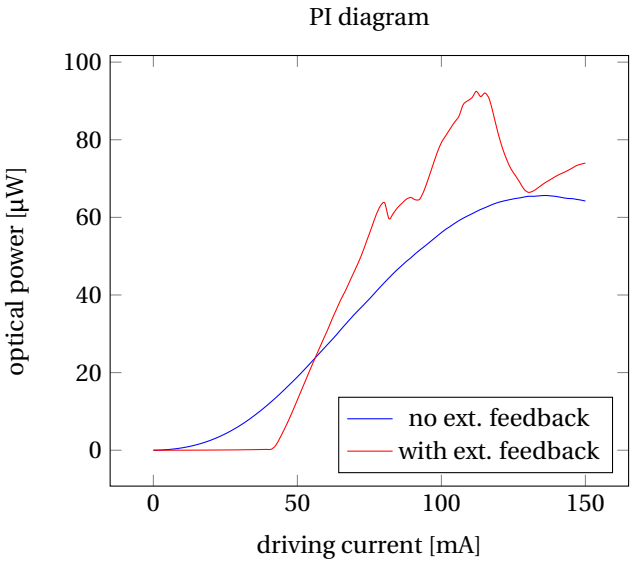

Figure 2.19: Measured optical power over driving current. Measurements taken with (red) and without (blue) external feedback. The chaotic behaviour of the red curve above 70 mA driving current is due variations in the fiber-chip coupling. While we could reach critical gain to enable lasing with external feedback, the fluctuations did not allow for stable single-mode operation.

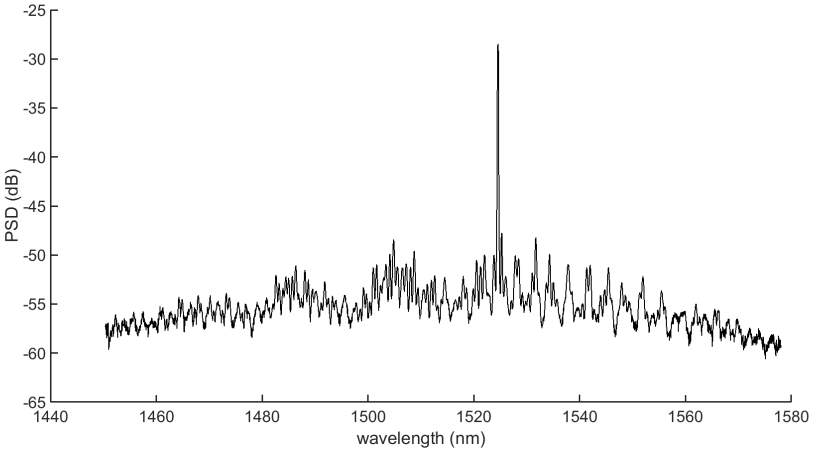

Figure 2.20: Power spectral density (PSD) in dB of chip-laser operating in single mode output using external feedback as shown in 2.18. The SMSR appears to be higher than 20 dB. It is worth mentioning, that the central peak could contain multiple lasing modes, as the spectral resolution was reduced to be able to scan over the whole wavelength range in a reasonable time.

2.7. CONCLUSION

This chapter introduced the necessary processes to design a tunable single-mode laser. Optical feedback and active media as well as the pumping mechanisms have been explained. With the introduction of intra-cavity filters and integrated optics, the design for the on-chip laser can be understood. The design for the chip CB07_2_3 of the 7th COBRA multi-project wafer run has been shown and the different nuances of the present variations have been explained. We presented an experimental setup to test the on-chip laser regarding its performance. While the tuning mechanism of the presented lasers have been verified, lasing operation has not been achieved. With the help of external feedback the underlying problem has been identified, and longer gain sections are supposed to lead to better results. As can be seen in the next chapter, resubmission was not needed since another chip was already fit for the task. The presented design was only making use of standard building blocks, which allows for easy adaptation and reapplication to longer wavelengths.

REFERENCES

[1] A. Perot and C. Fabry, *On the application of interference phenomena to the solution of various problems of spectroscopy and metrology,* Astrophysical Journal **9**, 87 (1899).

[2] I. N. Bronstein, K. A. Semendjajew, G. Musiol, and H. Mühlig, *Taschenbuch der Mathematik*, 7th ed. (Verlag Harri Deutsch, 2008).

[3] A. Hänsel, *Effekte der Selbstphasenmodulation in plasmonischen Wellenleitern*, Master's thesis, Friedrich-Schiller-Universität Jena (2011).

[4] B. E. A. Saleh and M. C. Teich, *Grundlagen der Photonik* (WILEY-VCH, 2008).

[5] T. Erneux and P. Glorieux, *Laser Dynamics* (Cambridge University Press, 2010).

[6] S. M. Sze, *Physics of Semiconductor Devices* (John Wiley and Sons, 1981).

[7] F. Bechstedt, *Festkörperphysik II,* lecture notes (2009).

[8] R. G. Hunsperger, *Integrated Optics: Theory and Technology* (Springer-Verlag, 1984).

[9] A. Yariv and P. Yeh, *Photonics*, 6th ed. (Oxford University Press, 2007).

[10] NIST, *CODATA internationally recommended 2014 values of the fundamental physical constants,* website.

[11] M. Smit, X. Leijtens, H. Ambrosius, E. Bente, J. van der Tol, B. Smalbrugge, T. de Vries, E.-J. Geluk, J. Bolk, R. van Veldhoven, L. Augustin, P. Thijs, D. D'Agostino, H. Rabbani, K. Lawniczuk, S. Stopinski, S. Tahvili, A. Corradi, E. Kleijn, D. Dzibrou, M. Felicetti, E. Bitincka, V. Moskalenko, J. Zhao, R. Santos, G. Gilardi, W. Yao, K. Williams, P. Stabile, P. Kuindersma, J. Pello, S. Bhat, Y. Jiao, D. Heiss, G. Roelkens, M. Wale, P. Firth, F. Soares, N. Grote, M. Schell, H. Debregeas, M. Achouche, J.-L. Gentner, A. Bakker, T. Korthorst, D. Gallagher, A. Dabbs, A. Melloni, F. Morichetti, D. Melati, A. Wonfor, R. Penty, R. Broeke, B. Musk, and D. Robbins, *An introduction to InP-based generic integration technology,* Semiconductor Science and Technology **29**, 083001 (2014).

[12] *JePPIX course 2012 - training on photonic integration technology,* workshop handouts (2012).

[13] H. Nishihara, M. Haruna, and T. Suhara, *Optical Integrated Circuits* (McGraw-Hill, 1989).

[14] A. W. Snyder and J. D. Love, *Optical Waveguide Theory* (Chapman and Hall, 1983).

[15] M. K. Smit, *New focusing and dispersive planar component based on an optical phased array,* Electronics Letters **24**, 385 (1988).

[16] L. Soldano and E. C. M. Pennings, *Optical multi-mode interference devices based on self-imaging: principles and applications,* Lightwave Technology, Journal of **13**, 615 (1995).

[17] R. W. Boyd, *Nonlinear Optics* (Academic Press (Elsevier), 2008).

[18] W. Yao, *Towards a high-capacity multi-channel transmitter in generic photonic integration technology*, Ph.D. thesis, Eindhoven University of Technology (2017).

[19] L. Xu, X. J. M. Leijtens, B. Doctor, T. de Vries, E. Smallbrugge, F. Karouta, and M. Smit, *MMI-Reflector: A Novel On-chip Reflector for Photonic Integrated Circuits,* in *ECOC 2009 - 35th European Conference on Optical Communication* (2009).

[20] E. Kleijn, M. K. Smit, and X. J. M. Leijtens, *Multimode interference reflectors: A new class of components for photonic integrated circuits,* J. Lightwave Technol. **31**, 3055 (2013).

[21] S. Latkowski, M. Smit, and E. Bente, *Integrated tunable and semiconductor laser and geometry and based on asymmetric mach-zehnder interferometers for gas sensing applications,* in *Symposium IEEE Photonics Society Benelux Chapter* (IEEE, Mons, 2012).

3

Integrated Optical Single-Mode Ring Laser with Mach-Zehnder Intra-cavity Filters

A laser with filter design similar to chapter 2, based on three asymmetric Mach-Zehnder interferometers, embedded in an optical ring resonator is presented. The chip has been processed within the COBRA multi-project wafer generic photonics platform. Four control voltages are enough to sweep over 74.3 *nm range with a linewidth of* 363 *kHz. The applicability to gas absorption measurements is demonstrated by scanning over a* 0.89 *GHz-wide absorption line of acetylene. Other fields of application include telecommunication and optical coherence tomography.*

Parts of this chapter have been published in IEEE Photonics Journal **7**, No. 6 (2015) [1].

3.1. INTRODUCTION

The conclusion of Chapter 2 was that the gain within the chip design was not sufficient to support laser operation. Fortunately another design was submitted to COBRA 6 with a similar layout using a ring resonator instead of relying on on-chip reflectors and the facet. This chip was processed later than the design for COBRA 7 had to be submitted, which is the design described in Chapter 2; otherwise knowledge gained from this design could have been incorporated in the follow up design. The designs on COBRA 6 featured 1 mm long semiconductor optical amplifier sections, twice as long as in Chapter 2.
Since a large part of this chapter has already been published in [1] we will abandon the notation of the preceding chapters and use the same as in the publication. This way both works can be used in unison.

3.2. LASER LAYOUT

The schematic of the used geometry can be found in Figure 3.1. A series of asymmetric Mach-Zehnder interferometers (AMZI) with different unbalances are incorportated in a ring-laser design. Each arm of the AMZIs is equipped with on-chip phase shifters. The phase shifters are tuned by applying a voltage to them and will be referred to as electro-refractive phase modulators[1] (ERM). All ERMs have a length of 2 mm. The gain needed to surpass laser threshold is provided by a 1 mm long semi-conductor optical amplifier (SOA) section, which is included in the ring. Multimode interference couplers (MMI) are used for splitting and combining the waveguides of the AMZI as well as coupling light from the ring towards the output line. Additionally a multimode interference reflector has been used to prevent light propagation in a direction without possible output. The output is angled and an anti-reflective coating has been applied to avoid reflections back into the ring laser.

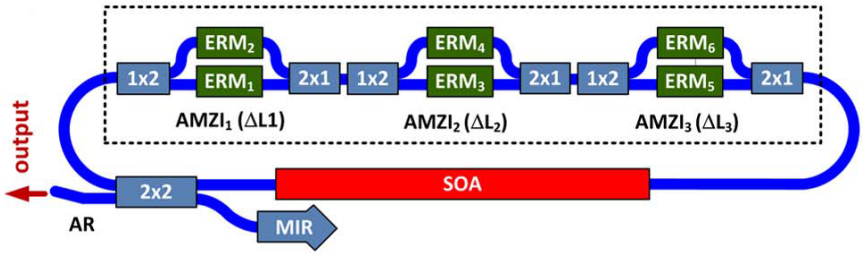

Figure 3.1: Schematic of the ring laser with a series of three AMZI filters as intra-cavity filters, along with the SOA and MMI couplers. An MIR is connected to one of the outports to ensure uni-directional laser operation. The output is angled and coated with an anti-reflective layer. [1]

As shown in Section 2.6 the transmission of an AMZI is periodic having a free spectral range $\mathrm{FSR}_N = c/\Delta L_N$ (c as the speed of light in vacuum, ΔL_N is the optical path length difference of the N-th AMZI). A combination of filters with different ΔL_N can lead to a transmission that can isolate an underlying ring laser longitudinal mode well enough

[1] In chapter 2 we labelled them as electro-optical phase modulators (EOPM).

to allow for single mode operation, as can be seen in Figure 2.12. With an efficiency of 15°/V·mm the ERMs allow for a shift of 2π in each arm, such that a full FSR sweep is still possible even if the ERM in one arm fails[2]. In any case a fourth control voltage is needed for tuning the cavity modes. The path length differences ΔL_N are 1263 µm, 97 µm, and 9 µm.

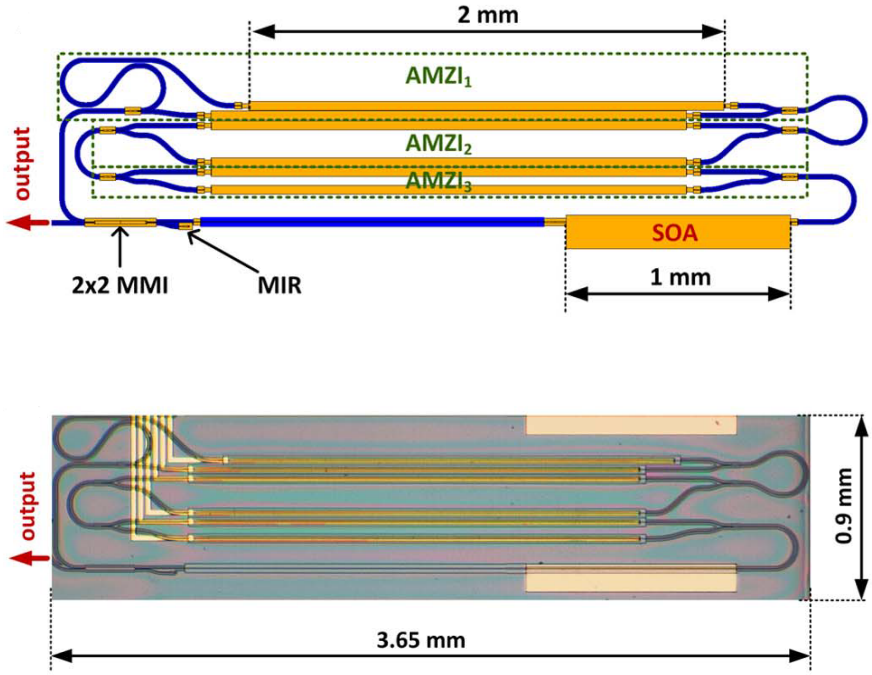

Figure 3.2: Mask (top) and microscope (bottom) picture of the single-mode laser circuit under test. The three different path length differences are visible in the top image, where the individual filter stages are marked with green dashed frames. The circuit is part of a larger chip shown in Figure 3.3.[1]

3.2.1. RING RESONATORS

Ring resonators[2] are similar to Fabry-Pérot resonators, and yet very different in some respects. A forward propagating wave going through a ring resonator will leave the resonator always in forward direction, assuming the components are perfect and no reflections occur. Especially in the lossless case with just a single coupler the transmission through the resonator will always be unity, independent of the coupling coefficient. The field within the resonator may differ depending on the coupling ratio. This can be seen

[2]The ring resonators here are actually race track resonators. The difference is purely geometrical, the physics remains unchanged.

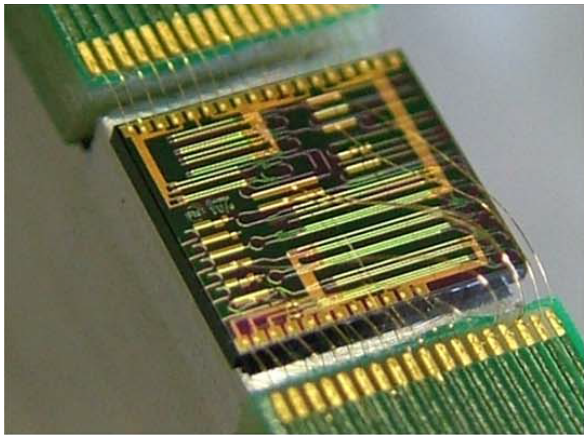

Figure 3.3: Fabricated chip mounted on an aluminum evaluation platform and wirebonded to printed circuit boards for easier electrical contact.[1]

using the following description of the coupler:

$$\begin{pmatrix} O_1 \\ O_2 \end{pmatrix} = \begin{pmatrix} t & -k^* \\ k & t^* \end{pmatrix} \begin{pmatrix} I_1 \\ I_2 \end{pmatrix} \tag{3.1}$$

with O_i indicating the output and I_i the input as shown in Section A.5 in the Appendix. With t being the transmission from input 1 to output 1 and k being the coupling to channel 2 from the same input channel, $|t|^2 + |k|^2 = 1$ holds, explaining the complex conjugation when considering input channel 2. Similar to [3, 4] we feed the output O_2 back to I_2, with $I_2 = l \cdot O_2$, as shown in Figure 3.4. In this case l denotes the change in amplitude and phase due to the propagation from output 2 to input 2.

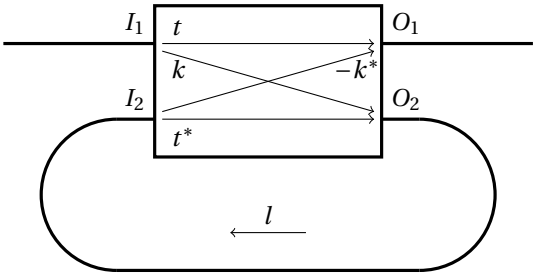

Figure 3.4: Schematic of a ring resonator. In this Figure the input channels are labeled as I_1 and I_2, similar to the output channels with the labels O_1 and O_2. The amplitude and phase changes in the coupler are described with t and k, whereas l describes the effect of propagation in the ring.

With that in mind we can write

$$O_2 = t^* I_2 + k I_1 = t^* l O_2 + k I_1 \Rightarrow \qquad O_2 = \frac{k}{1 - t^* l} I_1 \tag{3.2}$$

and it follows

$$O_1 = I_1 t - k^* I_2 = I_1 \left(t - \frac{k k^* l}{1 - t^* l} \right). \tag{3.3}$$

We define $x = |x| \exp(i\varphi_x)$ for $x = t, l, k$ and use $|t|^2 + |k|^2 = 1$ to get

$$O_1 = I_1 \frac{t(1 - t^* l) - |k|^2 l}{1 - t^* l} = I_1 \frac{t - l(|t|^2 + |k|^2)}{1 - t^* l} \tag{3.4}$$

$$= \frac{-|l| + |t| e^{i(\varphi_t - \varphi_l)}}{e^{-i\varphi_l} - |t| \cdot |l| e^{-i\varphi_t}} I_1 \tag{3.5}$$

When defining $\phi = \varphi_l - \varphi_t$ and using $e^{i\phi} + e^{-i\phi} = 2\cos\phi$ we end up with

$$|O_1|^2 = \frac{|t^2| + |l|^2 - 2|l||t|\cos\phi}{1 + |l|^2|t|^2 - 2|l||t|\cos\phi} |I_1|^2. \tag{3.6}$$

The definition of ϕ might look like a phase difference at first glance, but since the transmission within the ring is t^* (and $\varphi_t = -\varphi_{t^*}$) it represents actually the overall phase accumulated in one round trip in the resonator. For $|l| = 1$ the transmission is $|O_1|^2 / |I_1|^2 = 1$, independent of ϕ. In the case of $|l| = 0$ the transmission is reduced to $|t|^2$, the normal case for a coupler. For $\phi = m \cdot 2\pi$, Equation (3.6) simplifies to

$$|O_1|^2 = \left(\frac{|t| - |l|}{|l||t| - 1} \right)^2 |I_1|^2. \tag{3.7}$$

When coupling losses and transmission losses are equal, i.e. $|l| = |t|$ the transmitted power can vanish, which is referred to as critical coupling [4]. For $|l||t| = 1$ we can reach infinite transmission, which marks the lasing threshold.

ALTERNATIVE APPROACH: SUMMATION OF FIELDS

It is possible to write the output field as a sum of fields leaving the resonator with each round-trip. For this we obtain from Figure 3.4

$$O_1 = t I_1 + kl(-k^*) I_1 - klk^*(lt^*) I_1 - klk^*(lt^*)^2 I_1 + \cdots \tag{3.8}$$

$$= I_1 \left(t - \frac{|k|^2 l}{1 - lt^*} \right) \tag{3.9}$$

with the convergence radius of the geometric series $|lt^*| < 1$, showing the lasing condition derived before. Equations (3.3) and (3.9) are identical, resulting in the same solution.

3.2.2. TUNING SCHEME

The fact that all the phase shifters are of identical length results in the same voltage needed for a 2π phase delay, assuming that all ERMs show the same performance. When detuning all filters with the same frequency difference Δf, the single mode behaviour should be unchanged, but lasing occurs at a different wavelength. While a voltage was

applied to tune the filter, it is worth mentioning that the mathematics stay the same independent of the signal type used to control the phase shift. With $S_{2\pi}$ being the control signal for 2π phase shift in each filter, ΔL_N and ΔS_N being path length unbalance and control signal of the N-th element ($N = 1,2,3$) and Δf as the desired frequency detuning the following can be deduced:

$$\Delta S_N(f) = \frac{\Delta f}{v_g(f)} S_{2\pi}(f) \Delta L_N. \tag{3.10}$$

The group velocity v_g as well as $S_{2\pi}$ are frequency dependent, which has to be taken into account when tuning over a wide frequency range. In addition to the three AMZIs the longitudinal cavity modes have to be matched, which can be done by applying voltage on both arms of one AMZI simultaneously.
Since the ERMs have a finite breakdown voltage the controls signals have to be applied modulo 2π before exceeding it.

3.3. SIMULATIONS

Simulation data can be found in [1] and was obtained using two different software solutions [5, 6]. Tuning is possible over a 40 nm wavelength range, with a FSR due to cavity modes of 0.05 nm (5 GHz) and a side mode suppression ratio (SMSR) of more than 40dB. The results shown in Figure 3.5 were simulated in the simulation environment *PICWave*[5].

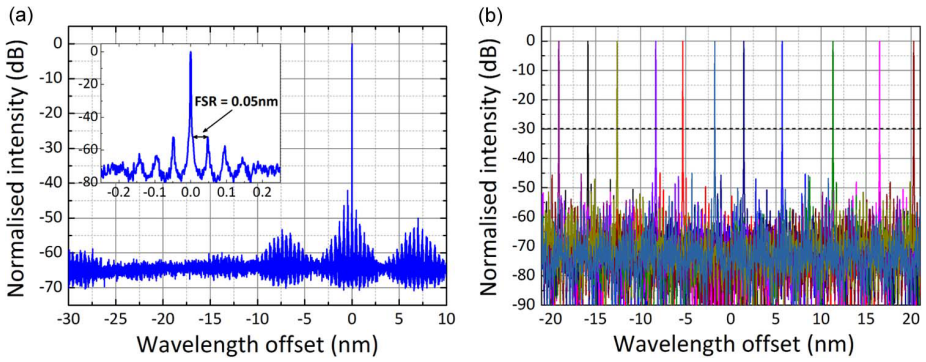

Figure 3.5: Simulated laser output. (a) Single-mode operation with an SMSR of more than 40dB. The inset is zooming in near the lasing mode showing cavity modes. (b) Simulated emission profiles for different filter settings. Temperature and current injection were kept constant, only ERM settings were changed. [1]

3.4. EXPERIMENTAL RESULTS

3.4.1. LASING

The laser output was collected with a lensed fiber for which a coupling loss of ~5dB was assumed. An optical isolator was used to avoid reflections back into the laser. The optical outpower over the driving current can be seen in Figure 3.6. The corresponding

voltage over the SOA section is shown in the same figure. A threshold current is visible at $I_{th} = 68\,mA$.

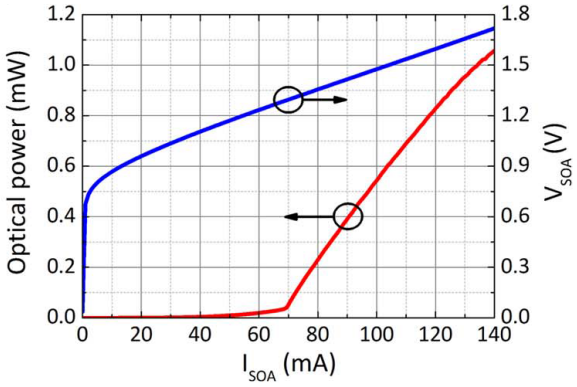

Figure 3.6: Optical power over driving current. The optical output power (red) is measured after coupling into a lensed fiber. The voltage curve (blue) corresponds to a slope resistance of 5.36 Ω. [1]

3.4.2. SINGLE-MODE OPERATION

A high resolution optical spectrum analyzer was used for the verification of the single-mode operation. The resolution of 20 MHz allowed for resolving the cavity modes, as can be seen in Figure 3.7(a). The laser was driven with $I_{SOA} = 134\,mA$, achieving a SMSR of 43dB. This is in good agreement with the simulations. The linewidth was measured

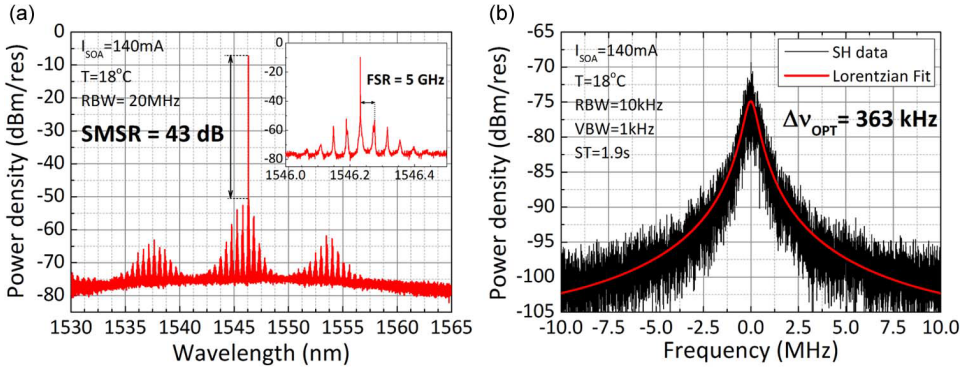

Figure 3.7: (a) Laser output spectrum as measured with a high resolution optical spectrum analyzer. The inset contains a zoom-in onto the lasing mode. (b) Linewidth retrieved with the self-heterodyne method.[1]

using a self-heterodyne technique. The outcome of this detection can be seen in Figure 3.7(b).

DELAYED SELF-HETERODYNE INTERFEROMETER

The delayed self-heterodyne interferometer (DSHI) was introduced by Okoshi *et al.* in 1980[7]. It offers the possibility of using a heterodyne detection scheme without the necessity of obtaining a stable local oscillator at the wavelength region under test. The signal to measure is split into two arms. One arm is sent through a delay line with a delay time τ_d and serves as a local oscillator. The arm is subsequently frequency shifted by a frequency difference of f_s. In the original publication of 1980 this is done via an acousto-optic modulator. The work presented in this chapter is based on the use of an electro-optic phase modulator. Both branches are recombined and the corresponding beat signal is measured with a fast photo-diode and analysed with an (electrical) spectrum analyzer. If τ_d is much longer than the coherence time of the laser both throughputs are not correlated and assuming white noise as dominant contribution to the laser line width the beat spectrum simplifies to[8]

$$S(f) \sim \frac{2S_{F0}}{(S_{F0})^2 + 2\pi\left(f - f_0\right)^2}. \tag{3.11}$$

In this case $S(f)$ is the frequency noise spectrum, f_0 is the centre frequency and S_{F0} the frequency independent white noise amplitude. The frequency shift f_s has to be larger than the linewidth, the frequency resolution is usually stated to be $\Delta s_{\text{ref}} \approx 1/\tau_d$.

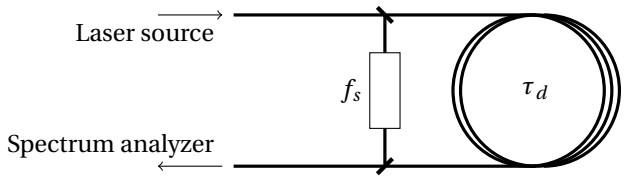

Figure 3.8: Simplified DSHI setup. The light is split into two arms, which are recombined later on a spectrum analyzer. One arm is frequency shifted, e.g. by the means of an acousto-optic modulator. This is indicated with f_s in the figure. The light in the other arm has to propagate long enough to lose its temporal coherence before the recombination with τ_d denoting the delay time.

3.4.3. TUNABILITY

Wavelength tuning can be realised by changing the SOA current or temperature or by applying a voltage to the on-chip phase shifters. The first two methods change the temperature and therefore expand/contract the crystal structure and consequently the accumulated phase while propagating. These thermal changes are not localised and take time to reach steady state, consequently they can only tune over a limited range and cannot match the tuning speed of the phase shifters. They do allow, however, for very fine tuning near the lasing line.

Here the wavelength tuning was done by applying a voltage to the ERMs, reaching from 0 to $V_{2\pi} = -11.5\,\text{V}$ (reverse bias). With four control voltages all four filters could be tuned. Three control voltages were applied to tune the AMZIs, the fourth voltage controlled the cavity mode. A wide tuning range of 74.3 nm was recorded using an optical spectrum analyzer, which can be seen in Figure 3.9(a).

Fine tuning was demonstrated by scanning an absorption line of a acetylene wavelength reference cell. The signal was split into two branches for recording reference and transmission through the cell at the same time. That way fluctuations in the laser intensity can be referenced out. The recorded transmission scanning over the R-branch 9th line of acetylene ($^{12}C_2H_2$, 50 Torr, 5 cm) can be found in Figure 3.9(b)[9]. The spectrum was recorded at 500 points with step size of 6.27 MHz,or 48 fm respectively. The wavelength was calibrated using the high resolution optical spectrum analyzer with 20 MHz resolution for the values at the side of the band.
This serves as a demonstration of the applicability of the developed on-chip laser for gas sensing experiments.

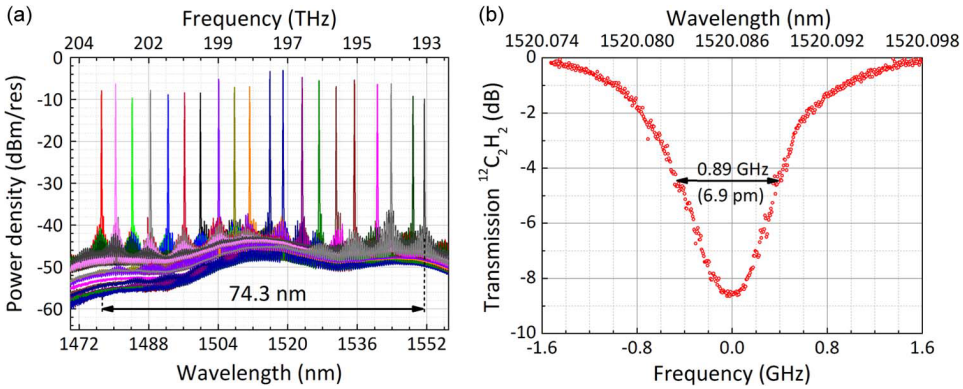

Figure 3.9: (a) Measured laser spectra for different filter settings spanning 74.3 nm. (b) When scanning the control voltages on the ERM the emission wavelength of the laser can be accurately controlled. This allowed for measuring the linewidth of an acetylene absorption line (R-branch, 9th line). [1]

For reproducibility the equipment used for the measurements reported in this chapter is listed in Table A.1 in SectionA.1.2 in the Appendix.

3.5. CONCLUSION

A fully integrated tunable single-mode ring laser with AMZI intra-cavity filters has been demonstrated. Output powers in the ~ 1 mW regime (measured in fiber) within a 363 kHz linewidth and a tunability over 74 nm were achieved. The feasibility for gas detection was verified by sweeping over an acetylene absorption line. Simulations of the laser chip matched the experimental results very well. The laser output was tuned by applying control voltages to four ERMs allowing for faster and more accurate tuning when compared to current variations. The design is limited to basic building blocks available in generic photonics technologies and can be easily adapted to different wavelengths.
The chips were designed and fabricated at the COBRA research institute. A second set was produced via foundry services offered by SMART Photonics through JePPIX; both offered similar functionality.

REFERENCES

[1] S. Latkowski, A. Hänsel, N. Bhattacharya, T. de Vries, L. Augustin, K. Williams, M. Smit, and E. Bente, *Novel widely tunable monolithically integrated laser source,* Photonics Journal, IEEE **7**, 1 (2015).

[2] M. Smit, X. Leijtens, H. Ambrosius, E. Bente, J. van der Tol, B. Smalbrugge, T. de Vries, E.-J. Geluk, J. Bolk, R. van Veldhoven, L. Augustin, P. Thijs, D. D'Agostino, H. Rabbani, K. Lawniczuk, S. Stopinski, S. Tahvili, A. Corradi, E. Kleijn, D. Dzibrou, M. Felicetti, E. Bitincka, V. Moskalenko, J. Zhao, R. Santos, G. Gilardi, W. Yao, K. Williams, P. Stabile, P. Kuindersma, J. Pello, S. Bhat, Y. Jiao, D. Heiss, G. Roelkens, M. Wale, P. Firth, F. Soares, N. Grote, M. Schell, H. Debregeas, M. Achouche, J.-L. Gentner, A. Bakker, T. Korthorst, D. Gallagher, A. Dabbs, A. Melloni, F. Morichetti, D. Melati, A. Wonfor, R. Penty, R. Broeke, B. Musk, and D. Robbins, *An introduction to InP-based generic integration technology,* Semiconductor Science and Technology **29**, 083001 (2014).

[3] W. Westerveld, *Silicon photonic micro-ring resonator to sense strain and ultrasound*, Ph.D. thesis, Delft University of Technology (2014).

[4] A. Yariv, *Universal relations for coupling of optical power between microresonators and dielectric waveguides,* Electronics Letters **36**, 321 (2000).

[5] *PICWave – Photonic IC (PIC)/Laser Diode/SOA Simulator for Active and Passive Devices [Online], http://www.photond.com/products/picwave.htm,* .

[6] *PhI Circuit Simulation – InP PIC Simulation Software [Online], Available: https://sites.google.com/site/inplaserseb/phi-circuit-simulation,* .

[7] T. Okoshi, K. Kikuchi, and A. Nakayama, *Novel method for high resolution measurement of laser output spectrum,* Electronics Letters **16**, 630 (1980).

[8] P. Horak and W. H. Loh, *On the delayed self-heterodyne interferometric technique for determining the linewidth of fiber lasers,* Opt. Express **14**, 3923 (2006).

[9] K. Nakagawa, M. de Labachelerie, Y. Awaji, and M. Kourogi, *Accurate optical frequency atlas of the 1.5-μm bands of acetylene,* J. Opt. Soc. Am. B **13**, 2708 (1996).

4

MONOLITHICALLY INTEGRATED WIDELY TUNABLE LASER SOURCE OPERATING AT 2 µM

The designs presented in Chapters 2 and 3 were feasibility studies to investigate whether the proposed intra-cavity filter allows single-mode laser operation. With the succesful demonstration at 1.55 µm wavelength the design needed to be adapted for longer wavelengths. A tunable single-mode laser emitting in the wavelength span of 2011 to 2042 nm is presented. Its capability for high-resolution scanning in demonstrated in a single-line spectroscopy experiment using a CO_2 reference cell.

Parts of this chapter have been published in Optica **3**, No. 12 (2016) [1].

4.1. INTRODUCTION

A integrated optical tunable laser source at wavelengths of 2 µm and higher has interesting applications in gas spectroscopy[2]. Several gas species, such as acetone, ammonia, carbon dioxide, water vapour, formaldehyde, diethylamine, ethylamin, and mehtylamine, absorb light at those wavelengths. Such applications include environmental monitoring in agriculture, process control in chemical pharmaceutical plants and laboratories, atmospheric pollution monitoring, and medical diagnosis and monitoring, to just name a few[3]. With the improved integration of the presented monolithical single-mode laser several sources can be used in conjunction. When resorting to integrated detection subsystems this can improve multispecies gas detection systems where the complexity and size of the bulk optics-based solutions are in many cases prohibitve factors[4]. Creating such a integrated optical device was the fundamental aim of the project; the chip presented in chapter 3 can be considered a major milestone and a step towards this goal. Progress in the extension of the photonic integration platform in COBRA research to accomodate for the 2 µm wavelength lead to the succesful fabrication of a full multi-project wafer (MPW) run with semiconductor optical amplifiers (SOA) in this new regime[5, 6]. This run included the photonic integrated circuit (PIC) which will be explained in the following sections. Due to the similarity to the PICs shown in chapter 2 and chapter 3 the explanations will be very brief.

4.2. LAYOUT

The design makes use of the generic active-passive integration technology developed in the COBRA research institute. It is modular in nature, consisting of several building blocks (BB) adding functionality to the circuit. Both, active and passive epitaxial layer stacks, are embedded in the same wafer. To reach the longer wavelength range a number of changes were introduced in the vertical layer stack. A detailed treatment of these changes can be found in [1]. Passive components needed their dimensions altered to be better optimised for 2 µm, while active components needed considerable changes.

To reach single-mode operation, an intra-cavity filter based on asymmetric Mach-Zehnder interferometers (AMZI) was used. When using ring lasers based on the nested configuration four of such lasers could be placed on a single MPW cell, which is shown in Figure 4.1.

The two internal AMZI stages featured physical path length differences of $\Delta L_1 = 2110\,\mu\text{m}$ and $\Delta L_2 = 16\,\mu\text{m}$ nested in a third one with an imbalance of $\Delta L_3^* = 74\,\mu\text{m}$. The light was split into the arms using multi-mode interference devices (MMI). The ring-cavity had a physical length of 9 mm, which corresponds to a free spectral range (FSR) ~ 9 GHz. The optical gain is provided by a 4 mm long SOA with a width 2.5 µm. The filter can be tuned with 1.8 mm long electro-refractive modulators (ERM). A voltage of 23 V can tune the AMZI over a full FSR ($V_{2\pi} = 23\,\text{V}$). With proper filter settings the laser is single-moded and tunable. Each circuit has two ports for fiber chip coupling. Two inner AMZI stages have on-chip photodiodes (PD) added on both sides of each stage for monitoring and calibration. The full layout is shown in Figure 4.2.

While the chip is decided to be entirely tuned by applying a control voltage, it is possible to make smaller sweeps using only one channel: temperature or current injected

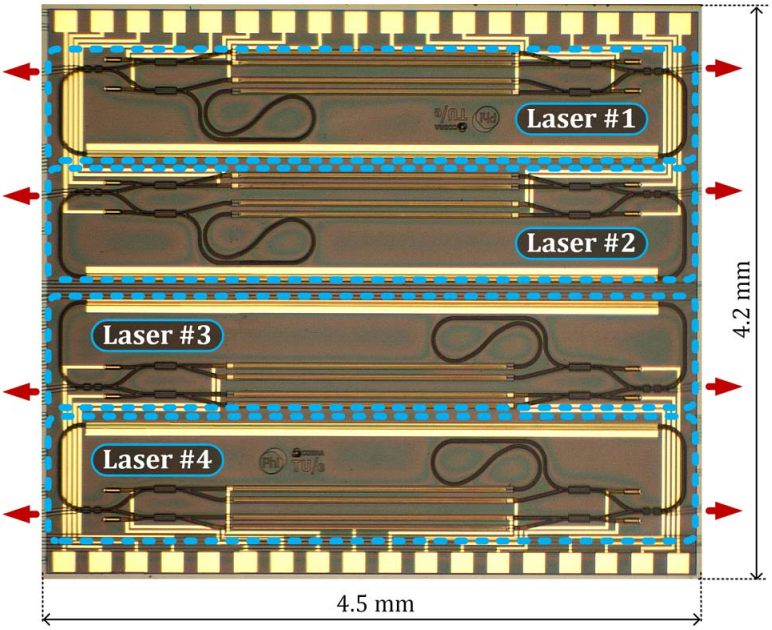

Figure 4.1: Microscope image of the fabricated MPW cell containing four on-chip lasers with two optical outputs each. [1]

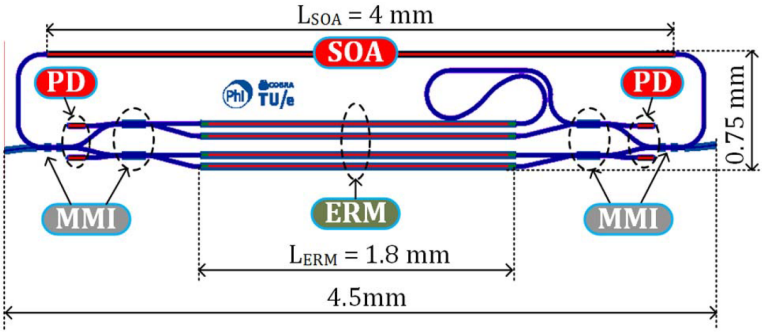

Figure 4.2: Mask layout of the ring laser in nested AMZi configuration. The gain esction spans almost over the whole width of the MPW cell. The 1.8 mm long ERM section allow for a full 2π sweep when tuning the voltage from 0 to 23 V. MMIs are used to form the filter, and the PD can be used to monitor and calibrate the laser. [1]

into the SOA.

4.3. MEASUREMENTS

The fabricated chip is mounted on an aluminum carrier, which is fixed to the submount. The submount is temperature controlled with a water cooling system. The measurements presented here were taken at a temperature of 18°C. The electrical contacts on the chip are wire bonded to a printed circuit board. An antireflection coated, lensed, single-mode fiber collects the light leaving the chip and feeds it through an optical isolator to the measurement equipment. The coupling loss is estimated to 5dB. To determine the laser threshold the total optical output power was measured with a photodiode (Thorlabs PDA10D). Lasing started at I_{TH} = 360 mA and reached an output power 97 µW at 500 mA (Figure 4.3). For these measurements no voltage was applied to the ERMs. The irregular behaviour at a bias current of 400 mA is attributed to mode jumps of the lasing mode. To verify if the laser is single-moded and tunable, spectrally resolved

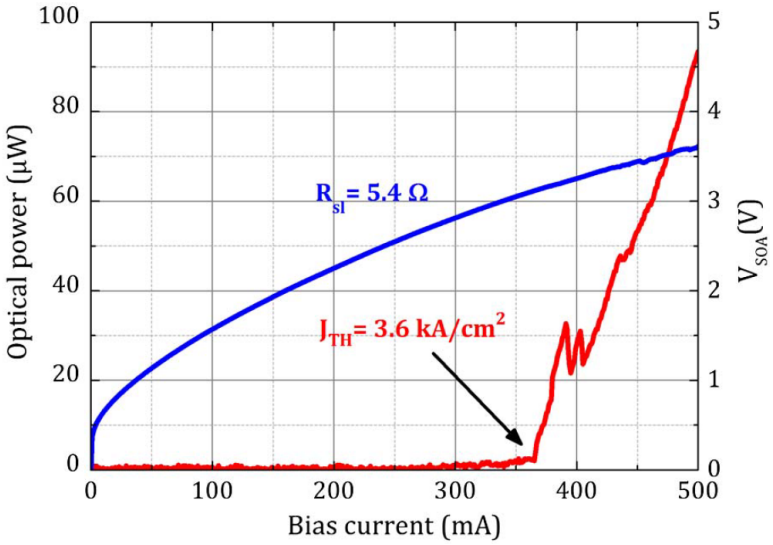

Figure 4.3: Optical power (red) in the fiber and voltage on the SOA (blue) over injected current. The measured threshold current of I_{TH} = 360 mA corresponds to a current density of J_{TH} = 360 mA/cm^2. The voltage across the SOA indicates a slope resistance of 5.4 Ω. [1]

measurements need to be taken. A Yokogawa AQ6375 optical spectrum analyser (OSA) with a 0.05 nm resolution recorded several spectra, with different reverse bias voltages applied to the ERM sections. All of those measurements had the same SOA current of I_{SOA} = 450 mA. These spectra are overlapped and presented in Figure 4.4. The side mode suppression ratio (SMSR) was more than 30 db for the whole measured wavelength range, which spanned over 31 nm, from 2011 to 2042 nm. While this confirms the wide tuning capabilities it does not allow insights into fine tuning possibilities the laser offers. To verify the feasibility of gas sensing experiments using this device the light

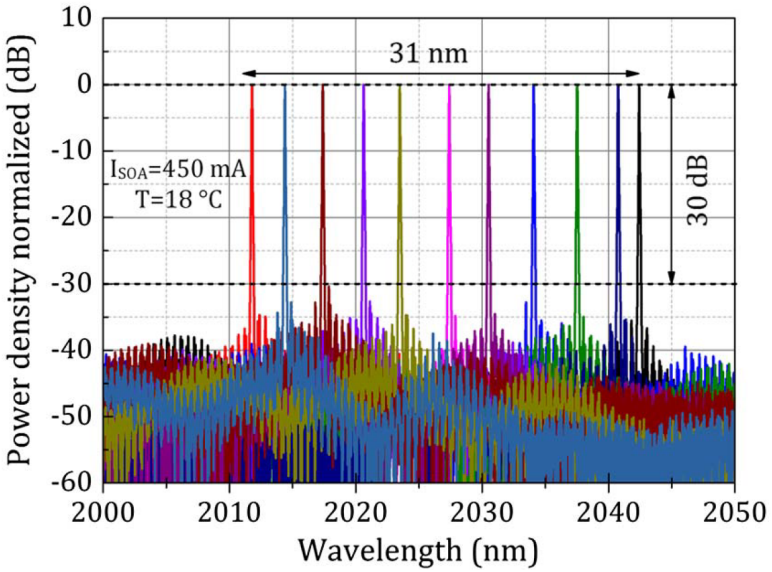

Figure 4.4: The output spectrum of the laser can be tuned by applying different sets of voltages to the ERM sections on the chip. Single-mode operation over a wavelength range of 31 nm could be achieved. [1]

was split in half using fiberised optical couplers. One fiber serves as reference signal, while the other output is sent through a gas reference cell. The reference signal was directed onto a PD, namely a Ultrafast Sensors FIR083. Fluctuations in the laser intensity will show up equally in reference and probe and can be compensated when comparing intensity ratios to not pollute the spectral data. The probe signal was collimated into free space and sent through a CO_2 filled gas cell, which is followed by another PD (Thorlabs PDA10). The cylindrical reference cell was 100 mm long with a diameter of 19 mm. The windows of the cell were angled by 2°to avoid cavity effects. The cell was filled with CO_2 at a pressure of 76 Torr, or 0.1 atm, and provided by Precision Glassblowing (TG-ABCO$_2$-Q). The ERMs were used to target a specific absorption line, while the actual sweep was done modulating the SOA current from 420 to 490 mA with a step size of 0.25 mA. Increasing the current does not only provide higher gain in the active medium, but also indirectly changes the refractive index of it. The aforementioned current modulation achieved a tuning range over 14 GHz with a frequency step size of 50 MHz. This translates into $\Delta\lambda \sim 676$ fm. Such a tuning range is wider than the cavity mode spacing of the laser. Figure 4.5 shows the measurement of the strongest CO_2 absorption line within the laser tuning range. Its spectral width of 864 MHz and the measured maximum absorption of 56% agree very well with the simulated spectrum, taken from HITRAN. The same figure also presents four additional CO_2 absorption lines that were measured. The wavelength scale was calibrated using the Yokogawa OSA.

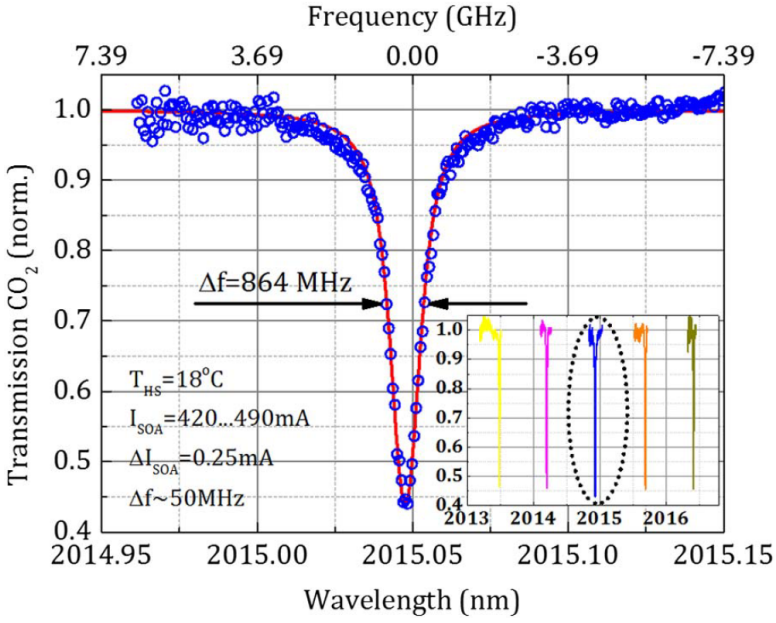

Figure 4.5: Normalised transmission through a gas cell filled with CO_2. While coarse tuning to select the absorption line has been done with ERMs, fine tuning has been achieved by scanning the SOA current. The tuning was fine enough to properly sample the absorption line. [1]

4.4. CONCLUSION

The presented device succesfully concluded the LWAVE-TECH project and extended the capabilities of the generic platform developed at COBRA to the longer wavelength regime of 2 µm. While the feasibilty for gas sensing applications was only shown measuring on a single gas, CO_2, the compact design as a result from the full integration shows prospect in multi-species gas sensing. Coarse tuning over a range of 31 nm could be shown; fine tuning without mode hops could be achieved by scanning the SOA current.

REFERENCES

[1] S. Latkowski, A. Hänsel, P. J. van Veldhoven, D. D'Agostino, H. Rabbani-Haghighi, B. Docter, N. Bhattacharya, P. J. A. Thijs, H. P. M. M. Ambrosius, M. K. Smit, K. A. Williams, and E. A. J. M. Bente, *Monolithically integrated widely tunable laser source operating at 2 µm,* Optica **3**, 1412 (2016).

[2] J. G. Crowder, S. D. Smith, A. Vass, and J. Keddie, *Infrared methods for gas detection,* in *Mid-infrared Semiconductor Optoelectronics*, edited by A. Krier (Springer London, London, 2006) pp. 595–613.

[3] Y. Ikeda, G.-M. Choi, D.-H. Chung, K. Fukuzato, and T. Nakajima, *A sensor for measuring co_2 gas temperature and concentration using 2µm dfb semiconductor laser,* in *Laser Techniques for Fluid Mechanics: Selected Papers from the 10th International Symposium Lisbon, Portugal July 10–13, 2000* (Springer Berlin Heidelberg, Berlin, Heidelberg, 2002) pp. 483–495.

[4] G. Roelkens, U. D. Dave, A. Gassenq, N. Hattasan, C. Hu, B. Kuyken, F. Leo, A. Malik, M. Muneeb, E. Ryckeboer, D. Sanchez, S. Uvin, R. Wang, Z. Hens, R. Baets, Y. Shimura, F. Gencarelli, B. Vincent, R. Loo, J. V. Campenhout, L. Cerutti, J. B. Rodriguez, E. Tournié, X. Chen, M. Nedeljkovic, G. Mashanovich, L. Shen, N. Healy, A. C. Peacock, X. Liu, R. Osgood, and W. M. J. Green, *Silicon-based photonic integration beyond the telecommunication wavelength range,* IEEE Journal of Selected Topics in Quantum Electronics **20**, 394 (2014).

[5] D. D'Agostino, S. Tahvilli, L. Sylwester, P. Veldhoven, H. Rabbani-Haghighi, C. Jin, B. Docter, H. Ambrosius, E. Bente, D. Lenstra, and M. Smit, *Monolithically integrated widely tunable coupled cavity laser source for gas sensing applications around 2.0 µm wavelength,* in *Advanced Photonics 2015* (Optical Society of America, 2015) p. JT5A.1.

[6] S. Latkowski, D. D'Agostino, P. J. van Veldhoven, H. Rabbani-Haghighi, B. Docter, H. Ambrosius, M. Smit, K. Williams, and E. A. J. M. Bente, *Monolithically integrated tunable laser source operating at 2 µm for gas sensing applications,* in *2015 IEEE Photonics Conference (IPC)* (2015) pp. 535–536.

5

DISTANCE METROLOGY WITH INTEGRATED MODE-LOCKED RING LASER

A setup for distance metrology using mode-resolved spectroscopy with a mode-locked monolithically integrated laser source and a VIPA spectrometer is presented. The laser featured a repetition rate of 2.5 GHz and was provided by COBRA and smartphotonics. The layout allowed for hybrid as well as passive mode-locking. Distance information has been obtaining by evaluating the interference from a Michelson interferometer, which depends on the arm length difference of measurement and reference arm. Distances have been retrieved with a standard deviation of 3 µm over the length of 25 mm.

A manuscript based on the work presented here has been submitted to a peer-reviewed scientific journal and is currently under review.

5.1. INTRODUCTION

The field of distance metrology greatly profited from the improvements made in the development of mode-locked laser sources[1]. Progress in the level of integration allowed for portable setups and enabled outdoor measurements. Significant improvements have been made towards stabilising mode-locked lasers, leading to frequency comb lasers[2]. Frequency combs have found a multitude of applications since their emergence at the beginning of this century[3]. While initial applications were targeting to provide an optical frequency standard, the versatility and reliability of frequency combs sparked new research in high-resolution optical spectroscopy and length metrology. As such frequency comb interferometry makes use of the strict definition of the optical spectrum to extract distance information from the interferogram of the many individual comb modes. Current relative accuracies are suffering from the uncertainty of the refractive index and are not limited by the performance of the frequency comb[4, 5]. While those accuracies can be achieved in-lab, outdoor measurements benefit from integrating the laser source[6]. Ti:Saph oscillator based frequency combs show limited performance when a portable setup is required. Fiber-based laser sources can be completely integrated, the long optical path length in the oscillator on the other hand results in a very low repetition rate. Since the repetition rate corresponds to the comb mode spacing in the frequency domain, a higher repetition rate loosens the resolution requirements of the spectrometer. External cavities can be employed to filter some of the comb modes until individual modes can be resolved, but increase the complexity of the system and are sensitive to vibrations[7]. On-chip lasers on the other hand are not only integrated and therefore less affected by ambient changes, they can also reach very high repetition rates. In this work we present a distance measurement based on mode-resolved interferometry with a monolithically integrated mode-locked laser. The laser features a repetition rate of 2.5 GHz, which ensures, that the modes can be separated by our spectrometer[8]. At the same time a higher repetition rate would decrease the sampling of the obtainable spectra and hence the accuracy of the distance determination. The combination with a VIPA (Virtually Imaged Phased Array) spectrometer allows to obtain the spectrum in a single shot[9, 10]. Not only does this allow for fast measurements, but in contrast to competing spectrometers, e.g. in a Fourier transform infrared spectroscopy (FTIR) setup, no moving parts are required, significantly improving the portability of the device. The interferogram was created by superimposing a beam propagating through the measurement arm with a beam propagating through a fixed reference arm. As such this method can only retrieve path length differences and requires an independent calibration of the reference arm.

5.2. EXPERIMENTAL SETUP

The setup for the experiment presented in this work has three main components: the on-chip laser source, the Michelson interferometer with reference and measurement arm, and the VIPA (Virtually Imaged Phased Array) spectrometer. Optical single-mode fibers are used to transfer the light between those components. A schematic of the setup can is shown in Figure 5.1. The different segments and their control parameters are explained in the following sections.

For repeatability the used equipment is listed in the Appendix in Section A.1.3.

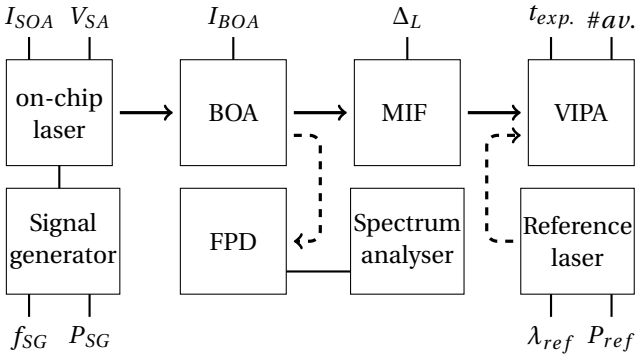

Figure 5.1: The main parts of the setup are shown in a schematic diagram. A lensed fiber collects light from the on-chip laser which is subsequently amplified in the booster optical amplifier (BOA). The amplified light is sent to the Michelson interferometer (MIF) with reference and measurement arm. The length difference of both arms can be read out from the spectrogram extracted from the VIPA spectrometer (VIPA). A reference laser was used to calibrate the VIPA spectrometer. A fast photo-detector (FPD) in combination with a spectrum analyser allowed for measuring the repetition rate of the laser. The light is guided with single-mode fibers between the different parts of the setup. Hybrid mode-locking could be achieved when using the signal generator. The main components and their control parameters are explained in greater detail in their corresponding sections.

5.2.1. ON-CHIP LASER

The on-chip laser has already been reported on in [8]. A mode-locked laser with a repetition rate of $f_{rep} \approx 2.5$ GHz at a wavelength of 1.58 µm was realised on the InP-based multi-project wafer (MPW) run by SMART Photonics. It was designed with the background of dual frequency comb spectroscopy in mind and featured a 33 mm long ring laser cavity. Elements for phase-control, as well as gain sections and saturable absorbers in the cavity allowed for tuning and optimisation of the laser output. The chip was mounted on an aluminum sub-carrier and the electrical contacts wire-bonded to a printed circuit board (PCB), which allowed for easier electrical control in comparison to landing needle probes. The chip allowed for passive and hybrid mode-locking. Passive mode-locking was realised by only applying DC (direct current) bias to the saturable absorber segments. In hybrid mode-locking operation an additional RF (radio frequency) signal was fed to the chip via a bias tee, which matched the f_{rep} of the chip in passive mode-locking operation. In hybrid mode-locking f_{rep} could be pinned to a fixed value over the course of the entire experiment, while in a passively locked operation the repetition rate of the laser experienced drift. The on-chip semiconductor optical amplifier (SOA) was connected to a laser diode driver. The chip featured angled output ports with anti-reflective coatings, from which the light was collected with a tapered fiber. To reach detectable power levels the light from the mode-locked laser had to be passed through a booster optical amplifier (BOA). A circulator was placed before the BOA to prevent light from the BOA from entering the chip and disturbing the laser operation. The final laser output is depending on the settings of I_{SOA}, V_{SA}, and I_{BOA}, corresponding to driving current, absorber voltage, and amplifier current. The repetition frequency of the laser was

measured with a fast photo-detector in combination with a spectrum analyser. The signal generator provided an RF signal with matching frequency $f_{SG} = f_{rep}$ and an output power of $P_{SG} = 10\,\text{dBm}$.

5.2.2. MICHELSON INTERFEROMETER

The distance measurement is done by comparing path length of reference arm and measurement arm in a Michelson interferometer. The outline of the setup is shown in Figure 5.2. The retroreflector in the reference arm remained stationary, while the length of the measurement arm was changed with a translation stage with a range 25 mm. Accurate knowledge of the length of the reference arm and the path length difference yields the measurement arm's length. The optical path length changes by twice the amount of the movement of the translation stage, and with a pulse separation of $l_{rep} = c/f_{rep} = 12$ cm only a half cycle can be measured; here c denotes the speed of light. This might have an effect when trying to obtain the distance data by only looking at the output power, but does not pose a problem when using a spectrometer.

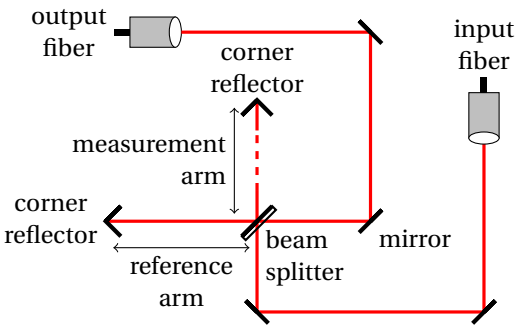

Figure 5.2: In the Michelson interferometer the reference arm was kept at a fixed distance to the beam splitter, while the retroreflector in the measurement arm was placed on a translation stage. Two mirrors were placed immediately before the fiber input and after the fiber output respectively to simplify the alignment. The optical path length difference can be obtained from the interference of both arms.

5.2.3. VIPA SPECTROMETER

The details of the VIPA spectrometer are explained in Section 6.3.1. In its core the spectrometer consists of two angular dispersers. The first disperser, consisting of the VIPA etalon and a cylindrical lens, has a high resolution. The drawback is the low free spectral range (FSR), which can be remedied by combining it with a grating spectrometer in orthogonal orientation as a post-disperser. After both dispersers a lens converts the angular change into a change of position on the detector plane of the camera. A continous broadband light source would create a line pattern on the camera, such as in the case of the measurements of Chapters 6, 7, and 8. For those measurements the resolution was not sufficient to observe the individual frequency comb modes. When following one line, spectral data for the span of one FSR of the VIPA can be obtained. To exceed this wavelength range, neighbouring lines have to be read out in the same fashion, which allows for *stitching* of the complete spectra out of the contributions of the individual lines

of the camera image, as shown in Figure 5.3. The etalon reached a resolution of 680 MHz with an FSR of 50 GHz for a single line. This resolution makes a seperation of the individual laser modes possible, as the mode separation is depending on the repetition rate of the mode-locked laser (2.5 GHz). Instead of lines the camera image shows an array of points, corresponding to the individual modes.

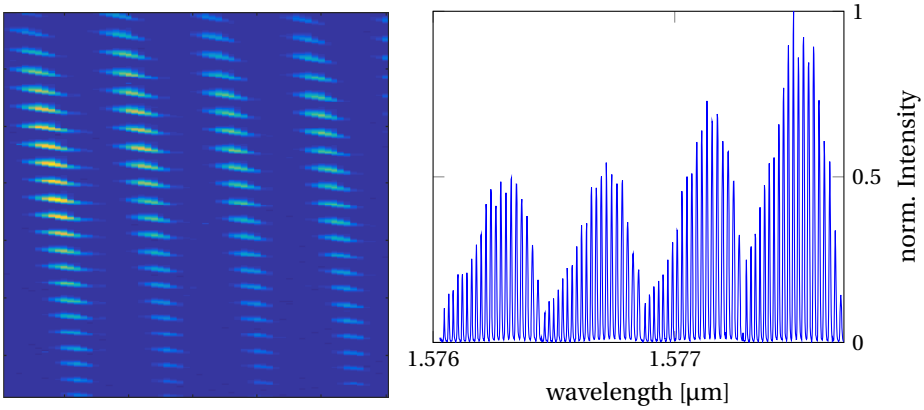

Figure 5.3: left: The spectral information is contained in a two-dimensional VIPA image. Following the individual lines yields the optical spectrum. A reduced data set is shown. right: Optical spectrum obtained from the VIPA image shown on the left side. After calibration of the FSR the line spectrum can be obtained by concatenating neighbouring lines.

5.3. METHOD AND MEASUREMENT

Distance information is contained in the spectral profile as obtained by the spectrometer. With the determination of the phase changes as a function of optical frequency the optical path length difference between measurement and reference arm can be extracted. The interference term in a Michelson interferometer is proportional to the cosine of the phase difference between both arms, $\cos\phi$. Ignoring dispersion for the operating bandwidth, the optical phase difference can be described as $\phi = \Delta L \cdot 4\pi n f/c$. Here ΔL is the length difference of both arms of the Michelson interferometer, n is the refractive index, f is the frequency of the light, and c denotes the speed of light. The actual path length difference of the beams in both arms corresponds $2\Delta L$, as the light travels through the arm length twice. Figure 5.4 shows data for a length difference of $\Delta L = 11\,\text{mm}$ with the corresponding cosine fit. Separate spectra of the individual arms as well as a dark image have been taken to normalise the amplitude of the modulation and simplify the fitting routine. While this has been done for each position individually, a packaged system is very likely to reach a stability that allows for a single set of those measurements for calibration. Due to nonlinearities in the camera's response the normalisation lacks accuracy in the regions of low intensity, but was sufficient to allow for a proper determination of the phase of the cosine function. The length difference can be obtained from $\Delta L = cP_{mod}/(4\pi n)$, with the modulation parameter $P_{mod} = 4\pi\Delta L n/c = d\phi/df$ taken from the curve fit. This is an alternative to obtaining the phase from methods

based on the Fast Fourier Transform [5, 11]. In contrast to regular spectral interferometry, where the frequency axis needs to be calibrated, the separation of the modes by the repetition rate of the laser provides a relative frequency scale. As the distance is only obtained from the slope $d\phi/df$, an absolute frequency calibration is not needed. A detailled discussion of this method can be found in [12]. This discussion includes possible undersampling of the interference pattern by the laser modes and how data can be extracted in that case. The optical distance measurement is compared with the value given by the translation stage. Figure 5.5 shows the outcome of this analysis. Deviations of the measured displacement exhibit a root mean square value of rms ~ 3µm, or a peak value of ~ 6µm. As the intensity modulation caused by the interference periodically repeats for every 6 cm of arm length difference, an independent length measurement with such an accuracy is required to get an unambiguous distance estimate.

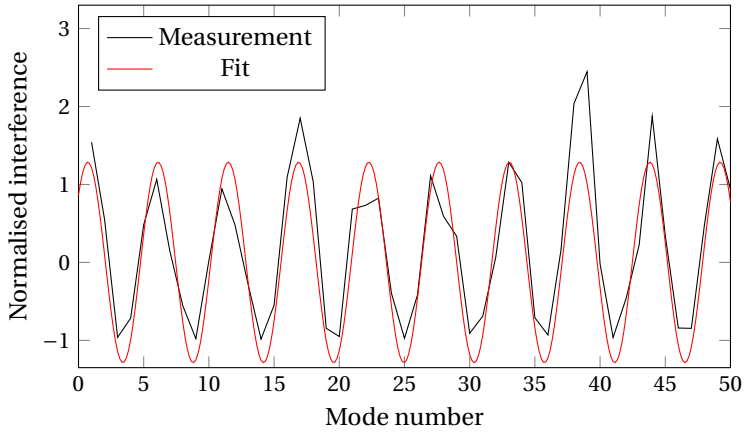

Figure 5.4: The normalised interference term allows for extracting distance information from the parameters obtained from the cosine fit. Only data for the first 50 out of the available 140 laser modes is shown. The fitting curve is shown in read, the processed data from the measurement with $\Delta L = 11$ mm in black. The corresponding VIPA image can be found in Figure 5.6(d).

5.4. CONCLUSION

We presented a length difference measurement with an integrated mode-locked laser. By using a VIPA spectrometer the optical spectra have been obtained in a single shot. With a laser repetition rate of 2.5 GHz the spectrometer allowed for direct observation of the individual modes. Over a length of 25 mm the distance could be extracted with an uncertainty rms ~ 3µm. Improvements on the bandwidth and the stability of the on-chip laser will further reduce this uncertainty. On the detector side advancements of the capabilities of infra-red cameras, especially with respect to the linearity of the response, will certainly enhance the accuracy of this method. It is possible combine the phase-sensitive measurement with an absorption measurement to eliminate the uncertainty of the refractive index that affects the distance determination[13]. The feasibility of this approach is investigated in Chapters 6, 7, and 8.

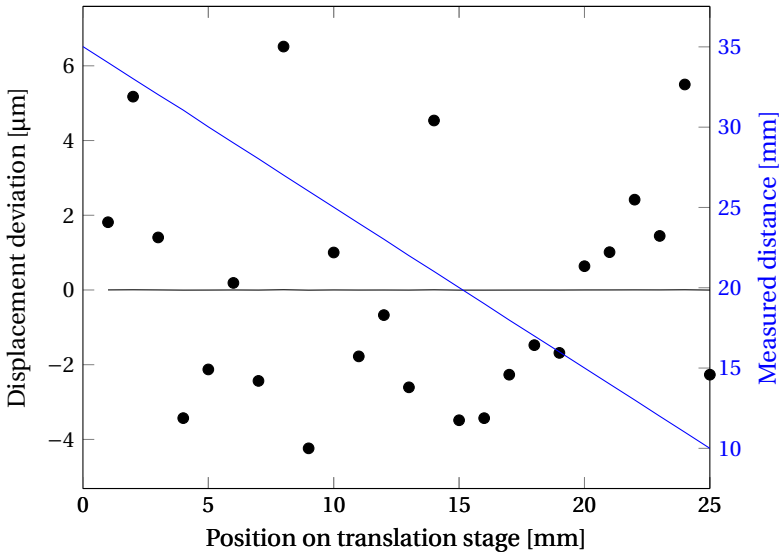

Figure 5.5: The position of the translation stage is changed in 1 mm increments. At each position the distance taken from the optical measurement is compared to length given by the translation stage. The difference of both displacements after compensation for misalignment is shown in black (left axis). The deviation peaks in a value of ~ 6µm. The blue curve (right axis) directly presents the optically measured distance in dependence of the position of the translation stage. With a pulse separation of $l_{\mathrm{rep}} = 12\,\mathrm{cm}$ the interference patterns repeat periodically after an arm length difference of 6 cm.

(a) $\Delta L = 27\,\mathrm{mm}$

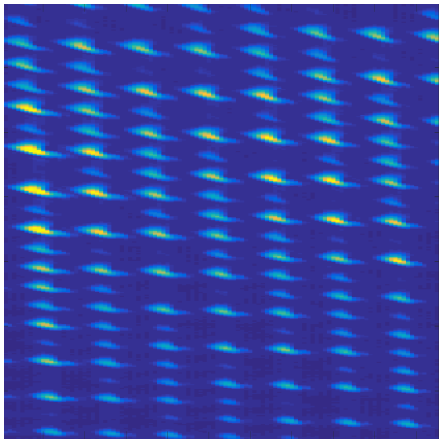

(b) $\Delta L = 20\,\mathrm{mm}$

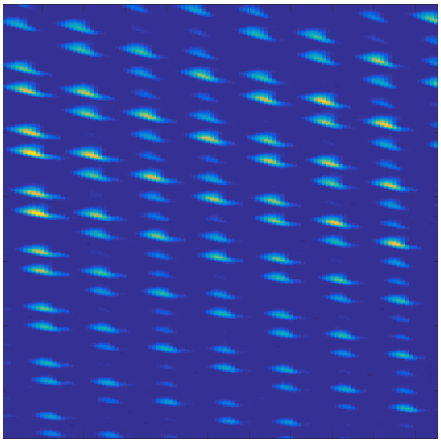

(c) $\Delta L = 16\,\mathrm{mm}$

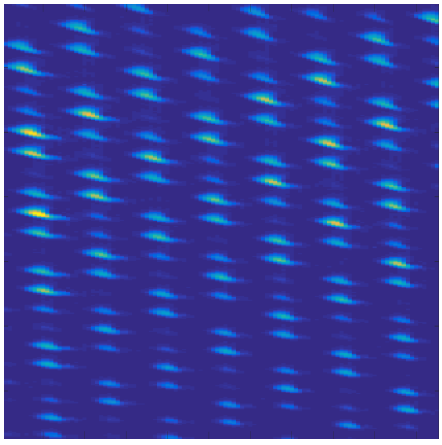

(d) $\Delta L = 11\,\mathrm{mm}$

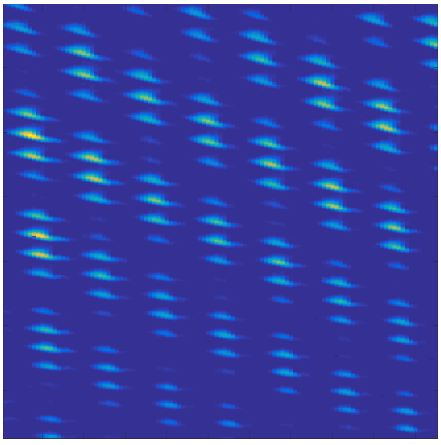

Figure 5.6: VIPA images of the interference of measurement and reference arm different for different displacements. The evaluation of those images allows for obtaining distance information. The arm length differences for the images have been (a) $\Delta L = 27\,\mathrm{mm}$, (b) $\Delta L = 20\,\mathrm{mm}$, (c) $\Delta L = 16\,\mathrm{mm}$, and (d) $\Delta L = 11\,\mathrm{mm}$.

REFERENCES

[1] K. Minoshima and H. Matsumoto, *High-accuracy measurement of 240-m distance in an optical tunnel by use of a compact femtosecond laser,* Appl. Opt. **39**, 5512 (2000).

[2] J. L. Hall, *Optical frequency measurement: 40 years of technology revolutions,* IEEE Journal of Selected Topics in Quantum Electronics **6**, 1136 (2000).

[3] S. A. Diddams, *The evolving optical frequency comb [invited],* J. Opt. Soc. Am. B **27**, B51 (2010).

[4] S. A. van den Berg, S. van Eldik, and N. Bhattacharya, *Mode-resolved frequency comb interferometry for high-accuracy long distance measurement,* Scientific Reports **5**, 14661 (2015), article.

[5] M. Cui, M. G. Zeitouny, N. Bhattacharya, S. A. van den Berg, and H. P. Urbach, *Long distance measurement with femtosecond pulses using a dispersive interferometer,* Opt. Express **19**, 6549 (2011).

[6] L. C. Sinclair, I. Coddington, W. C. Swann, G. B. Rieker, A. Hati, K. Iwakuni, and N. R. Newbury, *Operation of an optically coherent frequency comb outside the metrology lab,* Opt. Express **22**, 6996 (2014).

[7] R. Šmíd, A. Hänsel, L. Pravdová, J. Sobota, O. Číp, and N. Bhattacharya, *Comb mode filtering silver mirror cavity for spectroscopic distance measurement,* Review of Scientific Instruments **87**, 093107 (2016), http://dx.doi.org/10.1063/1.4962681.

[8] S. Latkowski, V. Moskalenko, S. Tahvili, L. Augustin, M. Smit, K. Williams, and E. Bente, *Monolithically integrated 2.5 ghz extended cavity mode-locked ring laser with intracavity phase modulators,* Opt. Lett. **40**, 77 (2015).

[9] A. Vega, A. M. Weiner, and C. Lin, *Generalized grating equation for virtually-imaged phased-array spectral dispersers,* Appl. Opt. **42**, 4152 (2003).

[10] S. Xiao and A. Weiner, *2-d wavelength demultiplexer with potential for ≥ 1000 channels in the c-band,* Opt. Express **12**, 2895 (2004), vIPA.

[11] K.-N. Joo, Y. Kim, and S.-W. Kim, *Distance measurements by combined method based on a femtosecond pulse laser,* Opt. Express **16**, 19799 (2008).

[12] S. A. van den Berg, S. T. Persijn, G. J. P. Kok, M. G. Zeitouny, and N. Bhattacharya, *Many-wavelength interferometry with thousands of lasers for absolute distance measurement,* Physical Review Letters **108** (2012), 10.1103/physrevlett.108.183901.

[13] A. Hänsel, A. Reyes-Reyes, S. T. Persijn, H. P. Urbach, and N. Bhattacharya, *Temperature measurement using frequency comb absorption spectroscopy of CO_2,* Review of Scientific Instruments **88**, 053113 (2017), http://dx.doi.org/10.1063/1.4984252 .

6

SPECTROSCOPIC GAS TEMPERATURE MEASUREMENTS

Temperature changes in a gas lead to a change of the refractive index, as can be seen from Edlén's equation, as well as to a change of absorption. When determining the temperature of a gas by measuring the absorption, it is possible to determine the refractive index accordingly. This knowledge can be used to improve the accuracy of long-distance measurements in air, where refractive index variations are a limiting factor. A setup for measuring the temperature of CO_2 and O_2 in a gas cell is presented and the involved components are characterised. Limitations of the method are discussed.

6.1. INTRODUCTION

Optical path lengths differ from the physical distances by factor n, with n being the refractive index of the material the light propagates through. Depending on the method this can either be the group index, or the phase refractive index of the material. In the interferometric methods discussed here, the latter has to be used. Consequently when measuring distances using light the refractive index will always enter the field, as long as measurements are not taken in vacuum. Since the majority of earthbound long distance measurements has to take place in ambient air variations in the refractive index lead to inaccuracies in the distance determination. Edlén provided an equation for the refractive index of dry air, which he revised later [1, 2]. Special attention was given to the influences of temperature and pressure. In the boundary layer of our planet (earth) the latter is varying less than the former[3]:

$$\frac{\delta p}{< p >} \approx \frac{0.01\,\mathrm{kPa}}{100\,\mathrm{kPa}} = 10^{-4} \tag{6.1}$$

$$\frac{\delta T}{< T >} \approx \frac{1\,\mathrm{K}}{300\,\mathrm{K}} \approx 3.33 \cdot 10^{-3} \tag{6.2}$$

$$\tag{6.3}$$

For closed systems, i.e. systems with a constant volume and molecule number, and an ideal gas a change in temperature directly reflects a change in pressure[1]. In both cases a temperature measurement seemed to be sufficient. This is usually done by accompanying the distance measurements with a thermometer array, which is placed alongside the beam. This provides several localised measurements around the beam propagation path from which the temperature in the beam path is deduced. The accuracy of this approach depends on the density of the sensor placement and the homogenity of the ambient medium in the experiment. Obtaining the environmental parameters spectroscopically promises several advantages. First of all the temperature can be measured exactly at the propagation path. Additionally temperatures measured this way will automatically be integrated line data, as each point in the propagation path of the beam provides data. The temperature dependence of the absorption is included in the spectroscopic data, which was obtained from HITRAN on the web[4]. There are other atmospheric transfer codes available, such as LOWTRAN, FASCODE, MODTRAN, and PCLNWIN[5].
When extending the scheme to long distance measurements in open air turbulences will have to be taken into account. The discussion of those effects will be saved for Chapter 7.

6.1.1. EDLÉN'S EQUATION

Edlén analysed measurements of the dispersion of standard air, i.e. air at standard temperature and pressure, and derived the following formula for the refractive index n of air

$$(n-1)\cdot 10^8 = 6431.8 + \frac{2949330}{146-\sigma^2} + \frac{25536}{41-\sigma^2} \tag{6.4}$$

[1] From $pV = Nk_BT$ it follows $p \propto T$ when V, N = const; (T, V, N, p, k_B)=(Temperature, Volume, Particle number, pressure, Boltzmann constant)

as “simplest and best representation of the observed values” [1], which he updated later to

$$(n-1)\cdot 10^8 = 8342.13 + \frac{2\,406\,030}{130-\sigma^2} + \frac{15\,997}{38.9-\sigma^2}. \tag{6.5}$$

In both equations n is the refractive index and σ is the wavenumber in $(\mu m)^{-1}$. The influence of pressure and temperature on the refractive index was expressed by the formula

$$(n-1)_{tp} = (n-1)_s \frac{0.00138823\cdot p}{1+0.003671\cdot t}, \tag{6.6}$$

with p in torr and t in °C [2]. In Equation (6.6) the index s denotes standard air as introduced above, while the index tp marks the refractive index taking different pressures and temperatures into account. For visible radiations and normal atmospheric conditions he considered the influence of water vapor by finding

$$n_{tpf} - n_{tp} = -f(5.722 - 0.0457\sigma^2)\cdot 10^{-8}. \tag{6.7}$$

In the last equation f is the partial pressure of water in air (again in torr), at the same temperature and total pressure as before.
The formulae have been derived by reviewing existing spectroscopic measurements and combining them to cover a wider spectrum. They are empirical in nature and are based on experimental data.

6.2. ABSORPTION SPECTROSCOPY

Atoms, molecules and crystals can absorb light. According to quantum mechanics this corresponds to destroying a photon and using this energy to change the state of the interacting particle. It is not sufficient to have a photon energy that matches the difference between two states, the transition itself has to be allowed (this can be seen as a quantum mechanical interpretation of momentum, angular momentum and energy conservation). To each transition a probability is attributed, that depends among others on the population density in both states. Usually an atom, molecule or crystal (from now on simply referred to as particle) is filling vacant allowed states with electrons starting from the lowest energy. Thermal excitation leads to excitation of higher energy states and vacant states of lower energy. In addition to that the temperature influences the number of molecules in a given volume and the absorption linewidth.
Independent of what is causing the change in absorption, a temperature influence can directly be seen when looking at the spectra, as the line strengths change. Similar pressure changes can be monitored when looking at the linewidth of a transition. The HITRAN database allows for predicting the influence of those parameters on the spectrum[4].

6.3. SETUP

A schematic of the used setup can be found in Figure 6.2. It contains two VIPA (Virtually Imaged Phased Array) spectrometers, each containing a VIPA etalon. We will refer to the VIPA spectrometer simply as *VIPA*; the *VIPA etalon* will be always named as

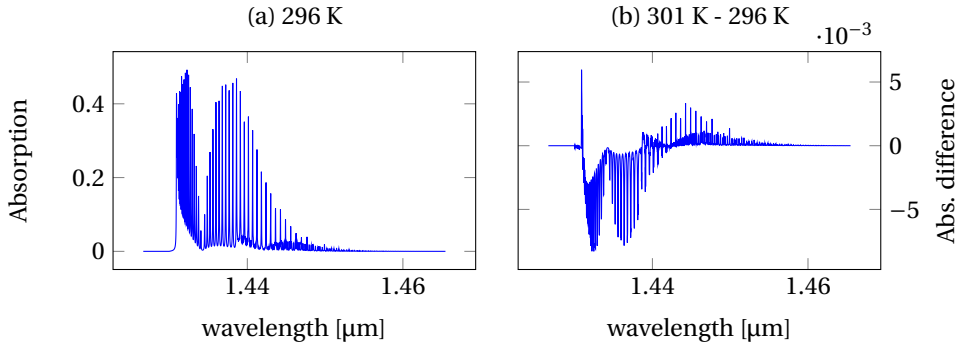

Figure 6.1: (a) HITRAN spectra for 1.5 m pure CO_2 at atmospheric pressure and a temperature of 296 K. The maximum absorption in that wavelength regions exceeds 40% . (b) Difference in absorption when subtracting the profile of 296 K from the profile of 301 K. The differences in absorption are less than 1% for a 5°C temperature change.

such. The used light source is a frequency comb (FC) laser, although the resolution of the spectrometers was insufficient to resolve the modes. To extend the wavelength from the infra-red region to the visible light a second-harmonic generation (SHG) nonlinear crystal was placed in the focussed spot of the beam. Both wavelength ranges were recollimated by the virtue of a parabolic mirror, which avoids chromatic aberrations, which can be quite significant over the wide wavelength range present in this setup. Since the spectrometers contained cameras sensitive to visible and infrared light respectively, a dichroic mirror needed to be inserted to separate both beams.
VIPA, FC and SHG will be explained in the following sections.

6.3.1. VIPA SPECTROMETER

The VIPA specrometer used in the setup was making use of a VIPA etalon as a high resolution spectrometer. High resolution resolution is usually paired with a small free spectral range, which necessiates the use of a pre-disperser, which was a grating in our case. Similar to a grating the VIPA etalon is an angular disperser. The angular displacement is imaged with a lens onto the camera. A schematic of the spectrometer is shown in Figure 6.3. A similar setup has been succesfully used for distance measurements before[6].

VIPA ETALON

A VIPA can be considered a Fabry-Pérot interferometer with some modifications[7–10]. A thin glass plate is coated on two parallel sides with reflective coatings: e.g. $\lesssim$100% on the entrance side at ~95% on the other side. A small window is left uncoated (or provided with an anti-reflective coating) at the entrance side. A focussed spot on the back wall of the VIPA can be considered as a point emitter[2]. Due to the highly reflective walls the system mimicks a set of (virtual) emitters along the reflection angle of the beam (see

[2] Since a cylindrical lens is used it is actually a line emitter. Every component used is invariant in the neutral direction of the cylindrical lens, for which reason we can reduce our considerations to the 2D case. In that framework the line reduces to a point.

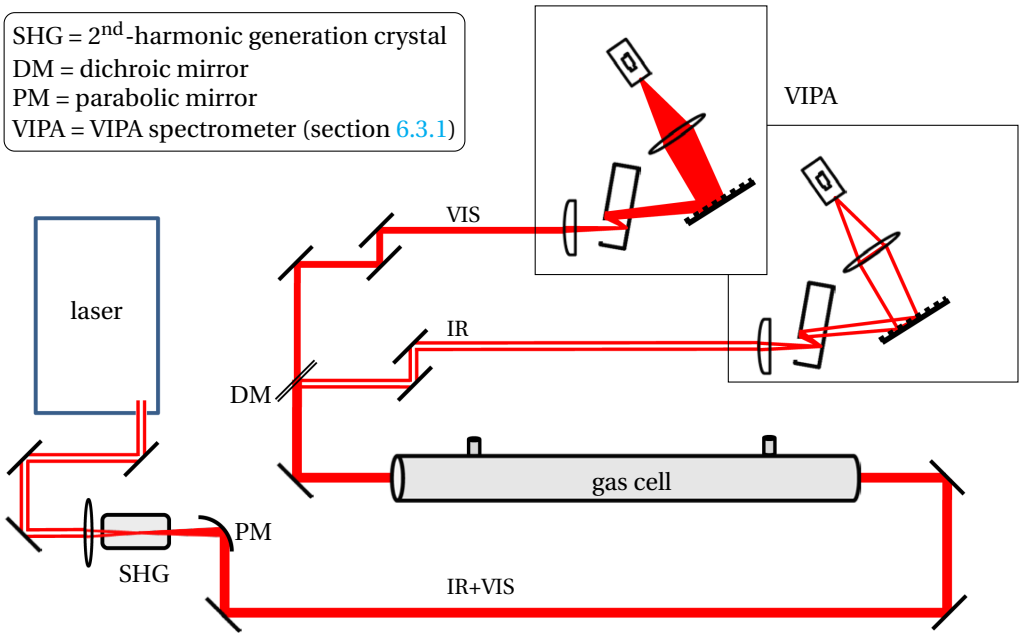

Figure 6.2: Schematic of the setup for the temperature measurement. The infra-red laser beam is focussed on a nonlinear optical crystal to generate frequency-doubled visible light. Both beams are recollimated with a parabolic mirror and guided through the gas cell, which can be filled with CO_2, O_2, and N_2 at variable pressures. A dichroic mirror is separating both wavelength ranges directing them to the corresponding VIPA spectrometers.

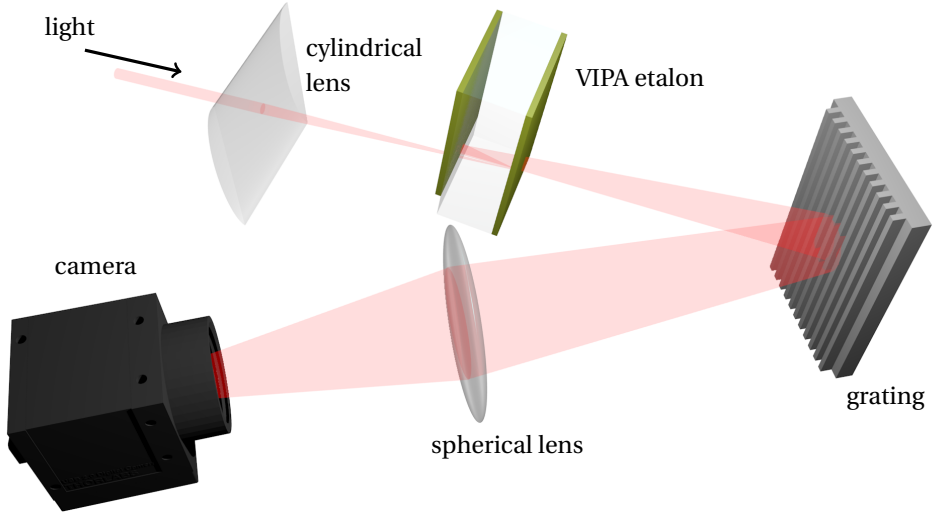

Figure 6.3: In the used VIPA spectrometer light entering the spectrometer is dispersed in the y-direction by means of the VIPA etalon in combination with a cylindrical lens. A grating is used as a pre-disperser in the x-direction before the light is imaged on a camera.

Figure 6.4 for clarification).

The following derivations assume an air-spaced VIPA and is based on [10]. The difference between air-spaced and glass etalon can be removed when using Snell's law and $\theta_i = n \cdot \theta_{\text{incident}}$ and scaling the thickness accordingly. The angular changes are expected to be small due to the almost perpendicular incidence. Care also has be taken when considering the light leaving the etalon, which suffers from refraction as well. The positions of the emitters are labelled with the index $n = 0, 1, 2, \cdots$, with $n = 0$ being the point where the beam entering the VIPA hits the reflective layer at the exit side. For a Gaussian beam at its waist it holds that

$$E_n(x) = (Rr)^n \exp\left(-\frac{(x-\Delta x_n)^2}{w_0^2}\right) E_0. \tag{6.8}$$

In this case E_0 is the field strength of the incident light, R and r are the reflectivities (field-wise) of the front and back reflective interface respectively. For a collimated beam with radius w prior to focussing of the cylindrical lens with a focal length of f, $w_0 = \lambda f / \pi w$ where λ denotes the wavelength. The displacement in the transversal direction, that is in x, is

$$\Delta x_n = 2nt \sin(\theta_i) \tag{6.9}$$

with t being the thickness of the etalon. Similar the longitudinal displacement is

$$\Delta z_n = 2nt \cos(\theta_i). \tag{6.10}$$

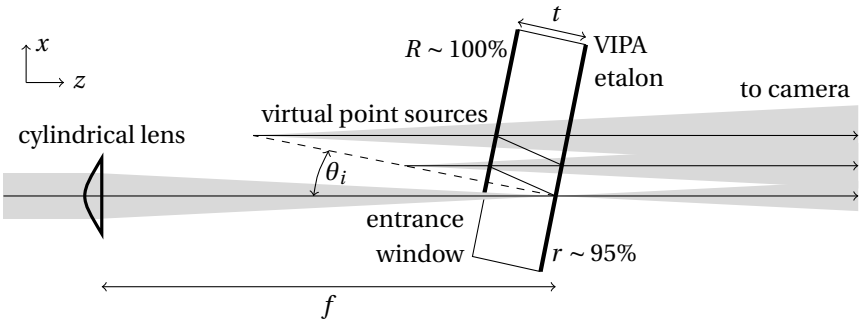

Figure 6.4: Virtual point sources, created by reflections of the focussed spot on the backside of the VIPA etalon interfere allowing only certain wavelengths to be transmitted at a fixed angle. At the camera side a lens is placed to image infinity on the sensor array of the camera (not shown here, see Figure 6.3). Refraction of the incoming light at the interface of the entrance window is ignored to simplify the drawing.

The lens is acting as a Fourier transformer, with the resulting field at the back focal plane[10–12]

$$E_{\text{out}}(x_F,\lambda) \propto \exp(-ikd)\exp\left(-i\frac{k}{2F}\left[1-\frac{d}{F}\right]x_F^2\right)\int_{-\infty}^{\infty} E_{\text{in}}\exp\left(\frac{ikx_Fx}{F}\right)dx, \tag{6.11}$$

where E_{out} denotes the field in the back focal plane of the lens, and E_{in} denoting the field before the lens. The dependence on λ is given by $k = 2\pi/\lambda$. The focal length of the spherical lens is F, the camera is placed in the back focal plane; x_F being the x-coordinate in the focal plane. The distance between object plane and lens is denoted by the symbol d. To simplify further calculations we assume the front focal plane to match the waist of the beam with $n = 0$, i.e. the incident beam: $d_n = F + \Delta z_n$. This assumption is purely for convenience and is not a demand on the experimental setup. It follows the outgoing field for the n-th virtual source is

$$E_{\text{out},n}(x_F,\lambda) \propto \exp(-ik\Delta z_n)\exp\left(i\frac{k\Delta z_n}{2F^2}x_F^2\right)\int_{-\infty}^{\infty} E_n(x)\exp\left(\frac{ikx_Fx}{F}\right)dx. \tag{6.12}$$

Inserting Equation (6.8) into Equation (6.12) we have

$$\begin{aligned} E_{\text{out},n}(x_F,\lambda) \propto (Rr)^n \exp\left(-\frac{f^2}{F^2}\frac{x_F^2}{W^2}\right)\cdot\exp\left(-i\frac{4n\pi t\cos(\theta_i)}{\lambda}\right) \\ \cdot\exp\left(i\frac{4n\pi t\sin(\theta_i)x_F}{\lambda F}\right)\cdot\exp\left(i\frac{2n\pi t\cos(\theta_i)x_F^2}{\lambda F^2}\right). \end{aligned} \tag{6.13}$$

By summing over all sources the total field can be obtained, $E_{\text{out}} = \sum_n E_{\text{out},n}$, hence

$$E_{\text{out}} \propto \exp\left(-\frac{f^2}{F^2}\frac{x_F^2}{W^2}\right) \cdot \sum_{n=0}^{N}\left[(Rr)^n \exp\left(-i\frac{4n\pi t\cos(\theta_i)}{\lambda}\right) \cdot \exp\left(i\frac{4n\pi t\sin(\theta_i)x_F}{\lambda F}\right) \cdot \exp\left(i\frac{2n\pi t\cos(\theta_i)x_F^2}{\lambda F^2}\right)\right]. \tag{6.14}$$

For a sufficiently large number of virtual sources N ($N \to \infty$) the equation can be simplified to

$$E_{\text{out}}(x_F,\lambda) \propto \exp\left(-\frac{f^2}{F^2}\frac{x_F^2}{W^2}\right) \frac{1}{1 - Rr\exp\left(-i\frac{4\pi t\cos(\theta_i)}{\lambda} + i\frac{4\pi t\sin(\theta_i)x_F}{\lambda F} + i\frac{2\pi t\cos(\theta_i)x_F^2}{\lambda F^2}\right)} \tag{6.15}$$

with a resulting intensity distribution $I_{\text{out}}(X_F,\lambda) \propto |E_{\text{out}}(x_F,\lambda)|^2$ of

$$I_{\text{out}}(X_F,\lambda) \propto \exp\left(-2\frac{f^2}{F^2}\frac{x_F^2}{W^2}\right) \frac{1}{(1-Rr)^2 + 4Rr\sin^2\left(\frac{k\Delta}{2}\right)}. \tag{6.16}$$

We used

$$\Delta = 2t\cos(\theta_i) - \frac{2t\sin(\theta_i)\,x_F}{F} - \frac{t\cos(\theta_i)\,x_F^2}{F^2}. \tag{6.17}$$

Equation (6.16) shows a Gaussian shape in x_F, and for fixed x_F a Lorentz distribution[3] in k. The transmission is maximised for wavelengths satisfying $k\Delta = 2m\pi$ with m as an integer. For small angles, $\frac{x_F}{F} \approx \theta_\lambda$ the peak condition can be rewritten to

$$k\Delta = k\left(2t\cos(\theta_i) - 2t\sin(\theta_i)\theta_\lambda - t\cos(\theta_i)\theta_\lambda^2\right) = 2m\pi. \tag{6.18}$$

Consequently the free spectral range (FSR) is found to be

$$\text{FSR} = \frac{c}{2t\cos(\theta_i) - 2t\sin(\theta_i)\theta_\lambda - t\cos(\theta_i)\theta_\lambda^2}, \tag{6.19}$$

which can be converted (by the use of a Taylor expansion[4]) to

$$\text{FSR} = \frac{c}{2t\cos(\theta_i)}\left[1 + \tan(\theta_i)\theta_\lambda + \left(\frac{1}{2} + \tan^2(\theta_i)\right)\theta_\lambda^2\right]. \tag{6.20}$$

The peak output wavelength λ_p can be related to the dominant wavelength at direct transmission $m \cdot \lambda_0 = 2t\cos(\theta_i)$ via Equation (6.18):

$$\Delta\lambda = \frac{-2t\sin(\theta_i)\theta_\lambda - t\cos(\theta_i)\theta_\lambda^2}{m} = -\lambda_o\left(\tan(\theta_i)\theta_\lambda + \frac{\theta_\lambda^2}{2}\right). \tag{6.21}$$

[3] Lorentz distribution is a term commonly used in physics. It can also be referred to as Cauchy distribution.
[4] A derivation can be found in the appendix in Section A.6.

For Equation (6.21) we used the definition $\Delta\lambda = \lambda_p - \lambda_0$. The angular dispersion factor is consequently obtained by

$$\frac{d\,\Delta\lambda}{d\theta_\lambda} = \frac{d\lambda_p}{d\theta_\lambda} = -\lambda_0\,(\tan(\theta_i) + \theta_\lambda) \tag{6.22}$$

and hence

$$\frac{d\theta_\lambda}{d\lambda_p/\lambda_0} = -\frac{1}{\tan(\theta_i) + \theta_\lambda}. \tag{6.23}$$

Introducing the influence of the refractive index n_r for the solid VIPA the equations change to

$$k\Delta = k\left(2tn_r\cos(\theta_{\text{in}}) - 2t\tan(\theta_{\text{ni}})\cos(\theta_i)\theta_\lambda - \frac{t\cos(\theta_{\text{in}})}{n_r}\theta_\lambda^2\right) = 2m\pi \tag{6.24}$$

$$\Delta\lambda = \lambda_p - \lambda_0 - \lambda_0\left(\frac{\tan(\theta_{\text{in}})\cos(\theta_i)}{n_r\cos(\theta_{\text{in}})}\theta_\lambda + \frac{1}{2n_r^2}\theta_\lambda^2\right) \tag{6.25}$$

$$\frac{d\theta_\lambda}{d\lambda_p/\lambda_0} = -\frac{1}{\frac{\sin(2\theta_i)}{2\left(n_r^2-\sin^2(\theta_i)\right)} + \frac{1}{n_r^2}\theta_\lambda} \tag{6.26}$$

with $n_r\sin(\theta_{\text{in}}) = \sin(\theta_i)$ and $m\lambda_0 = 2tn_r\cos(\theta_{\text{in}})$. As mentioned before position on the camera x_F and θ_λ are related via $\frac{x_F}{F} = \theta_\lambda$. Following the derivations in [13] we can obtain a formula for the resolution of the VIPA. Equation (6.16) shows a maximum transmission of $I_{\max} \propto \frac{1}{(1-Rr)^2}$ for $k\Delta = 2m\pi$, as before. The transmission falls to $I_{\max}/2$ for

$$(1-Rr)^2 = 4Rr\sin^2\left(\frac{k\Delta}{2}\right) \quad\Rightarrow\quad \frac{1-Rr}{2\sqrt{Rr}} = \sin\left(\frac{k\Delta}{2}\right). \tag{6.27}$$

The VIPA has reflective coatings ($Rr \to 1$) allowing us to approximate the sine function. The sine function is periodic with a modulus of 2π. With $k_0\Delta = 2m\pi$ and $k = k_0 + \delta k$ we get $k\Delta = 2m\pi + \frac{1-Rr}{\sqrt{Rr}}$ and thus $\Delta\cdot\delta k = \frac{1-Rr}{\sqrt{Rr}}$. Taking twice the distance of peak to half maximum and using $\delta k = -\frac{2\pi}{\lambda^2}\delta\lambda$ results in

$$\delta\lambda_{\text{FWHM}} = \frac{\lambda^2(1-Rr)}{\pi\Delta\sqrt{Rr}} \approx \frac{\lambda^2}{2\pi tn_r\cos(\theta_{\text{in}})}\frac{1-Rr}{\sqrt{Rr}} \tag{6.28}$$

when only taking the first term in Equation (6.24) into account. Similarly we can conclude

$$\delta\nu_{\text{FWHM}} = \frac{c(1-Rr)}{\pi\Delta\sqrt{Rr}} \approx \frac{c}{2\pi tn_r\cos(\theta_{\text{in}})}\frac{1-Rr}{\sqrt{Rr}} \tag{6.29}$$

for the frequency resolution by applying $\delta\nu = -\frac{c}{\lambda^2}\delta\lambda$.

GRATING

A grating is a periodic structure, such as an array of slit apertures. This periodicity leads to a wavelength dependence of the transmission or reflection, except for the zeroth order. The grating used in this setup was a reflection grating, more specifically a blazed

grating. The resolving power of a grating is $\frac{\lambda}{\delta\lambda} = m \cdot k$[14]. Consequently the order of diffraction (m) and the number of diffracting apertures (k) affect the resolution. The amount of light diffracted into certain orders is depending on the configuration of the grating. A blazed grating consists of tilted structures with a saw-tooth profile. The diffraction efficiency can be increased when the diffraction angle of the chosen order matches the specular reflection angle of the saw-tooth surface, e.g. $\theta_1 = \theta_{\text{in}} + 2\theta_B$.

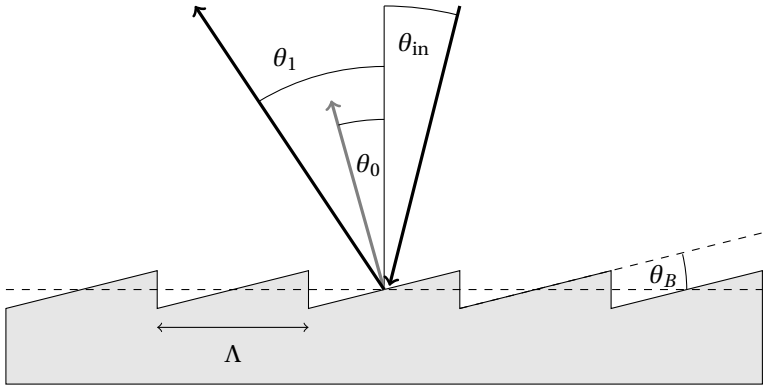

Figure 6.5: A blazed grating allows for improved diffraction efficiency into an order of choice. For the zero-th order $\theta_0 = \theta_{\text{in}}$ holds.

The directions of the diffracted orders can be calculated using the diffraction equation[12]

$$\sin(\theta_m) = \sin(\theta_{\text{in}}) + m\frac{\lambda}{\Lambda}. \tag{6.30}$$

6.3.2. FREQUENCY COMB LASERS

A frequency comb laser is a mode-locked laser with fixed set of discrete lines in its spectrum[15, 16]. The modes are separated by the repetition frequency $f_r = \frac{c}{2nL}$ with L denoting the resonator length and c/n being the speed of light in a medium with refractive index n. Since the mode separation corresponds to the periodicity of the signal in the time domain (with a period of $T = 1/f_r$), it is beneficial to treat the concept simultaneously in frequency and time domain (see Figure 6.6). Ultimately the pulse duration is limited by the bandwidth of supported frequencies. The comb offset is connected to the carrier envelope phase shift by $f_0 = \frac{1}{2\pi} f_r \Delta\phi_{ce}$, which itself can be expressed by $\Delta\phi_{ce} = \left(\frac{1}{v_g} - \frac{1}{v_p}\right) 2L\omega_c$. In this case v_p and v_g are the average group and phase velocities of the laser pulse with carrier/central angular frequency of ω_c.

For the absorption measurement in this experimental setup the comb can be considered to be a broadband laser source, since neither the spectral resolution of the spectrometer nor the temporal resolution of the camera are sufficient to separate the comb modes.

The wavelength span can be seen in Figure 6.7, which shows the power spectral density after second harmonic generation and propagation through a dichroic mirror.

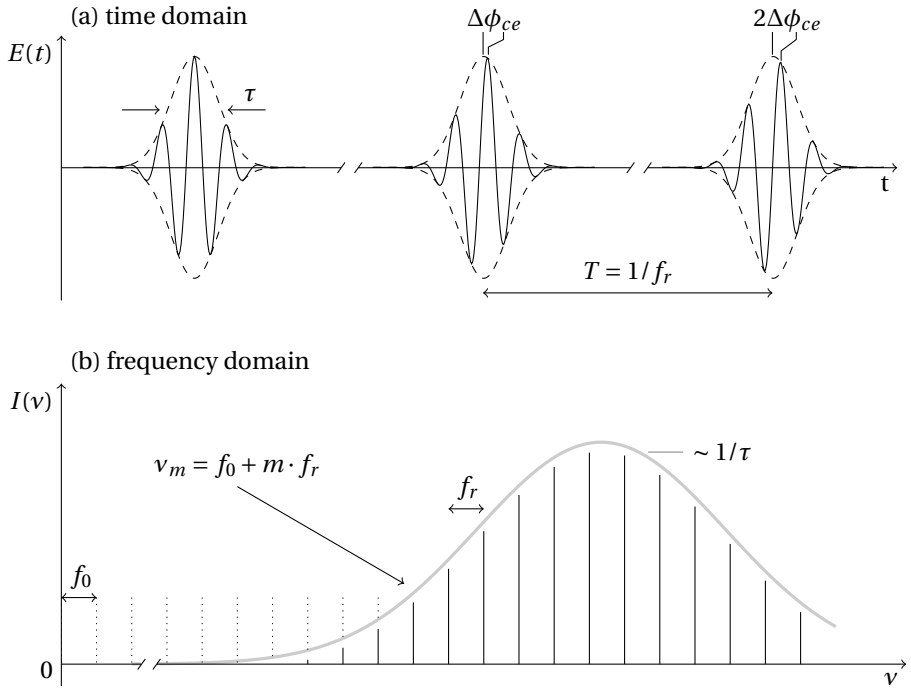

Figure 6.6: Optical frequency comb in (a) time and (b) frequency domain. The properties of the light in both domains is strongly related. The pulse duration τ is directly represented by the bandwidth in the spectral domain. The spectral line spacing is reflected in the repetition frequency f_r of the laser.
While this picture explains the relations between the quantities, frequency combs in experimental setups rarely show such a regular spectrum and pulse shape.

6.3.3. SECOND HARMONIC GENERATION

The output of the frequency comb laser is limited to the wavelength range of 1.4 to 1.6 µm. While this is sufficient for CO_2 spectroscopy, there are no absorption lines of O_2 in that interval. Fortunately those lines could be targetted by frequency doubling the laser light, which was done using the nonlinear optical effect of second harmonic generation (SHG).

Nonlinear optical processes, that means processes in which the response of the system depends on the incident power, can generally be described using Maxwell's equations assuming a nonlinear polarisation of the n-th order $\mathbf{P}^{(n)}_{\omega_\sigma}$ in the shape of[17]

$$\mathbf{P}^{(n)}_{\omega_\sigma} = \varepsilon_0 \sum_{\omega} K(-\omega_\sigma;\omega_1,\cdots,\omega_n)\chi^{(n)}(-\omega_\sigma;\omega_1,\cdots,\omega_n)|\mathbf{E}_{\omega_1}\cdots\mathbf{E}_{\omega_n}, \tag{6.31}$$

where $\chi^{(n)}$ is the corresponding tensor for the nonlinear interaction. The sum $\sum_\omega$ indicates the summation over all sets of $\omega_1,\cdots,\omega_n$ that satisfy $\omega_\sigma = \omega_1+\omega_2+\cdots+\omega_n$. This allows for arbitrary sequences of $\omega_1,\cdots,\omega_n$, which is factored in in the definition of the numerical factor

$$K(-\omega_\sigma;\omega_1,\cdots,\omega_n) = 2^{l+m-n}p. \tag{6.32}$$

Here $l = 1$ if $\omega_\sigma \neq 0$ and $l = 0$ otherwise, n is the order of the nonlinearity, p is the number of distinct permutations of $\omega_1,\cdots,\omega_n$, with m of the n frequencies being zero. Following this definition $K = 1$ for the linear response, $K = 1$ for sum (or difference) frequency generation, $K = \frac{1}{2}$ for second harmonic generation (SHG). The definition of negative frequency is to be interpreted as

$$[\mathbf{E}(\omega)]^* = \mathbf{E}(-\omega^*) \overset{\omega\in\mathbb{R}}{=} \mathbf{E}(-\omega). \tag{6.33}$$

Equation (6.31) can be expressed in scalar form according to

$$\left(P^{(n)}_{\omega_\sigma}\right)_\mu = \varepsilon_0 \sum_{\alpha_1\cdots\alpha_n}\sum_{\omega} K(-\omega_\sigma;\omega_1,\cdots,\omega_n)\cdot\chi^{(n)}_{\mu\alpha_1\cdots\alpha_n}(-\omega_\sigma;\omega_1,\cdots,\omega_n)\left(E_{\omega_1}\right)_{\alpha_1}\cdots\left(E_{\omega_n}\right)_{\alpha_n}. \tag{6.34}$$

In the case of SHG, an expression for the fields at the fundamental and at the doubled frequencies can be derived. The details of the derivations can be found in [17, 18]. For monochromatic waves it holds that

$$\frac{\partial}{\partial z}\hat{E}_{2\omega} = \frac{i2\omega}{2n_{2\omega}c}\left[\frac{1}{2}\chi^{(2)}(-2\omega;\omega,\omega)\hat{E}^2_\omega\right]\exp(i\,\Delta k\,z) \tag{6.35}$$

$$\frac{\partial}{\partial z}\hat{E}_{\omega} = \frac{i\omega}{2n_{\omega}c}\left[\chi^{(2)}(-2\omega;\omega,\omega)\hat{E}^*_\omega\hat{E}_{2\omega}\right]\exp(-i\,\Delta k\,z) \tag{6.36}$$

with the phase mismatch

$$\Delta k = 2k_\omega - k_{2\omega} = 2\omega(n_\omega - n_{2\omega})/c. \tag{6.37}$$

$\hat{E}$ denotes the slowly varying wave envelope. We changed the notation of n, formerly representing the order of the nonlinearity, to an expression for the refractive index at

respective wavelengths. The power flow between the fields is governed by the Manley-Rowe relation[5], which can be written as

$$\frac{1}{2\omega}\frac{\partial}{\partial z}I_{2\omega} = -\frac{1}{2}\frac{1}{\omega}\frac{\partial}{\partial z}I_{\omega}. \tag{6.38}$$

Assuming an undepleted pump[6] ($I(\omega)$ = const) the intensity after a propagation over a distance of L can be found to be

$$I_{2\omega}(L) = \frac{(2\omega)^2}{8\varepsilon_0 c^3}\frac{\left|\chi^{(2)}(-2\omega;\omega,\omega)\right|^2}{n_\omega^2 n_{2\omega}} I_\omega^2 L^2 \mathrm{sinc}^2(\Delta k L/2) \tag{6.39}$$

assuming the initial condition $\hat{E}_{2\omega}(z=0)=0$. For perfect phase matching the conversion efficiency can grow rather high, in which case Equation (6.39) is not accurate enough and an exact solution of the coupled equation is needed. We get

$$I_{2\omega}(L) = I_\omega(0)\tanh^2 GL, \tag{6.40}$$

$$I_\omega(L) = I_\omega(0)\mathrm{sech}^2(GL), \tag{6.41}$$

$$G^2 = \frac{2\omega^2}{\varepsilon_0 c^3}\frac{\left(\frac{1}{2}\chi^{(2)}(-2\omega;\omega,\omega)\right)^2}{n^3} I_\omega(0), \tag{6.42}$$

where we defined $n = n_{2\omega} = n_\omega$. Phase matching can be achieved using birefringent crystals for certain orientations. In general dispersion prevents phase matching for arbitrary orientations.

Media with inversion symmetry cannot produce second harmonic light, at least not in bulk media. This is just listed here for completeness, the interested reader can turn his attention to [17, 18]. In a nutshell it can be summarised that light incident on a second order nonlinear crystal can generate light of twice the frequency, or half the wavelength, if the intensity is sufficiently high.

The output of the second harmonic light along with the fundamental wavelength (at reduced power) can be found in Figure 6.7. As will be seen later the wavelength span is sufficiently long to contain several absorption lines of O_2.

6.4. MEASUREMENT PROCEDURE

Spectra were taken with a VIPA spectrometer. In such a spectrometer the spectral data are contained in a 2D camera image, with the intensity on the pixels representing the power spectral density (PSD) of a defined wavelength. A typical VIPA image, that is a picture acquired by the camera in the VIPA spectrometer, can be seen in Figure 6.8.

It is not sufficient to take an image of the sample alone. After subtracting a dark image the spectrum of the laser and the instrument function of the spectrometer still have to be calibrated for. A balanced detector scheme can accomplish that. For balanced

[5] While they may look rather trivial at first glance, they could be interpreted in terms of photon numbers. The derivation used only classical fields, while photons are a concept of quantum optics.

[6] The conversion efficiency usually remains small and the percentage loss of power for the fundamental frequency is mostly insignificant. For perfect phase matching and longer light propagation this is not valid anymore and the coupled equations have to be solved differently.

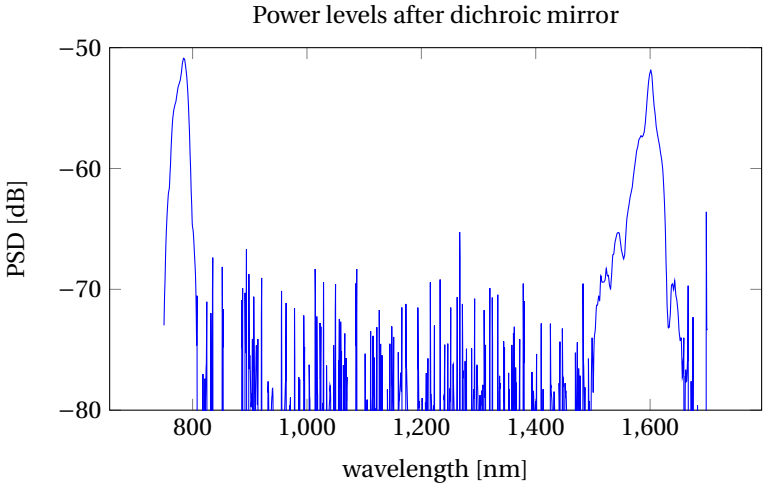

Figure 6.7: Power spectral density after passing the beam through a dichroic mirror to reduce the power of the fundamental wavelength. The shown output spans a range wide enough to observe several absorption lines of CO_2 and O_2.

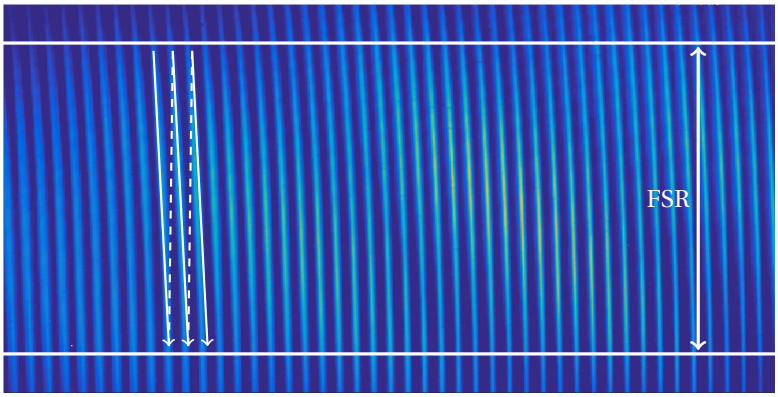

Figure 6.8: Power levels are expressed in line patterns on a VIPA image. The *stitching* procedure is visualised with white lines. After reading out spectral data over one FSR, the neighbour line has to be read out and the data can be concatenated to a spectral line.

detection at least two spectral images need to be taken, one containing the gas species under test and the other one of a neutral reference, e.g. a gas that is not absorbing at the measured wavelengths. Following this approach slow variations of the spectrometer response or the laser light intensity can be levelled out. When looking at the 2D VIPA image the difference between measurement and reference is a good measure for whether an absorption line is present or not, although it is not properly normalised. The VIPA needs to be calibrated either by using a single mode laser of defined wavelength or by fitting to a known absorption spectrum, e.g. from a laser wavelength reference cell. Once the FSR range is known, the mode stitching procedure reading out line spectra over one FSR and concatenating it with the neighbours, will transfer the 2D spectral data into line data. Once the 1D (line) spectra have been obtained, the ratio between measurement (spectrum of the laser after passing the gas cell filled with the gas under test) and reference (same for neutral gas) shows the transmission. This is impossible to do with the 2D data, which contains zero lines between the actual spectral information. The measurements have to be repeated for different temperatures to test if a transmission difference can be measured that matches the prediction from the simulations. The temperature was increased using a heating coil around the gas cell. Mass flow and pressure controllers were used to control the gas constituents in the cell and a thermometer was inserted to monitor the temperature. The setup allowed us to investigate absorption lines of both CO_2 and O_2. Consequently VIPA spectrometers for visible and infra-red light were built.

6.4.1. DEVELOPED SOFTWARE

The conversion of the two-dimensional VIPA images to a line spectrum contains too many data points to be done manually. A matlab script was written to automate the process; a graphical user interface (GUI) was created to simplify the initialisation of the script, which is shown in Figure 6.9[7].

6.5. OBTAINED DATA

Line spectra were obtained and steps were taken to improve on the quality of the acquired data. Limiting factors will be discussed in Section 6.6. Figures 6.10 and 6.11 show the best spectra we were able to obtain at room temperature for CO_2 and O_2. The spectra get worse when increasing the working temperature as can be seen in the comparison of Figure 6.12.

6.5.1. USED EQUIPMENT

The measurement equipment for the experiments of this chapter can be found in Section A.1.4 in the Appendix.

6.6. LIMITATIONS

While allowing the collection of the whole spectrum in one shot the VIPA has significant drawbacks limiting its usefulness for the attempted spectroscopic measurements. Due

[7] The software was created in Matlab 2011b. Newer versions do not run the file properly. The script version still works fine, but the GUI does not.

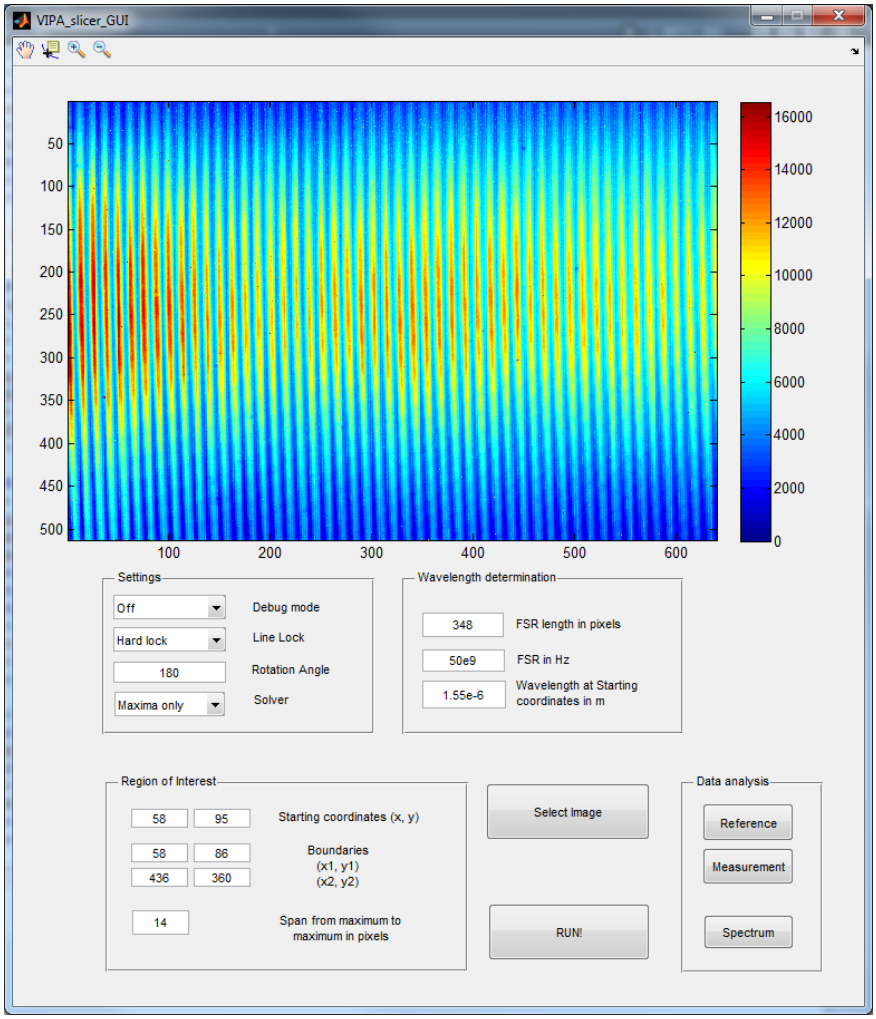

Figure 6.9: The script uses predetermined lines to follow and read out the intensity, which requires a rough estimate of the distance between two lines of maxima. The region of interest can be limited to avoid sections where the data is too noisy. Since the solver reads from top to bottom and left to right with increasing wavelength it might be needed to rotate the image. A pointer tool allows for selecting the pixels without plotting the picture separately. The corresponding spectra can be stored as reference and measurement in the memory and be used to determine the transmission spectrum of the test gas.
The intensity levels can be determined in two different ways: integrating between the minima surrounding the maximum, or by just considering solely the maximum level ignoring the spread of the maximum.

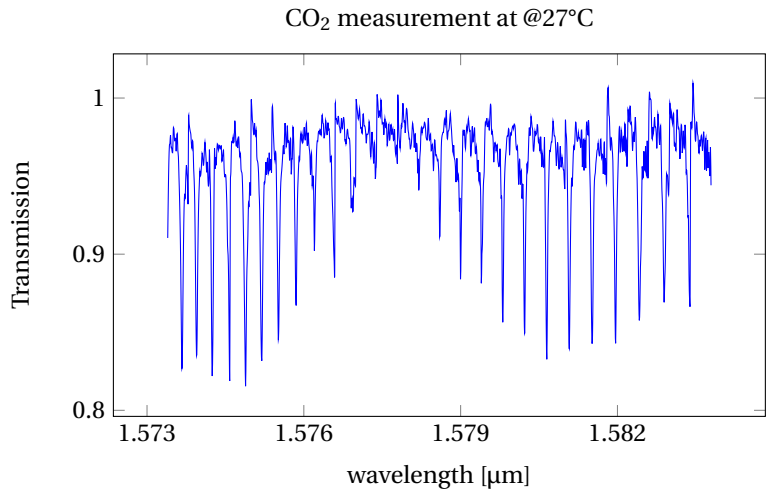

Figure 6.10: Obtained line spectrum for CO_2 at 27°C after applying the conversion software. The wavelength scale needs to be calibrated accurately matching known absorption lines to the ones measured. As can be seen in the figure the noise level is too high to attempt temperature measurements.

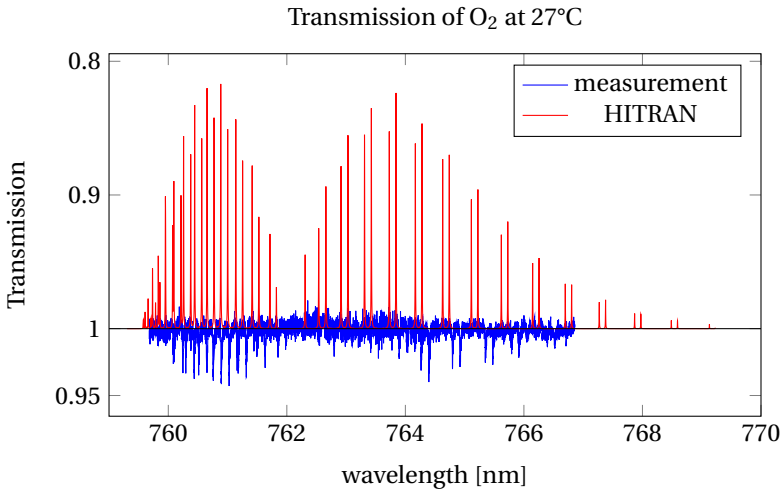

Figure 6.11: Comparison of the transmission lines of pure O_2 at the atmospheric pressure, as measured (blue) and simulated (red), for wavelengths around 1.5 m. The values for the HITRAN data are flipped, as can be seen when looking at the axis numbering, to improve the visualisation. The large difference in the magnitudes (~factor 4) hampers the wavelength calibration. In addition to that the baseline of the measurements show a strong noise level preventing meaningful temperature measurements.

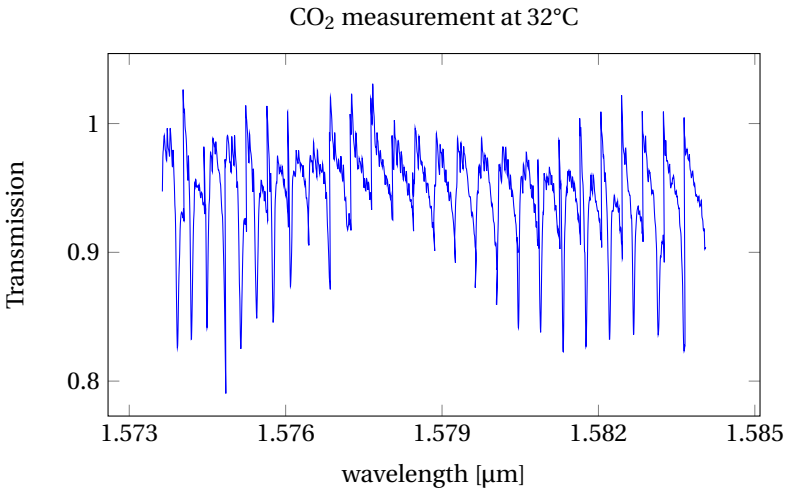

Figure 6.12: When increasing the working temperature to 32°C the data quality reduces (compare with Figure 6.10), which is an additional effect preventing temperature measurements.

to the fact that it is an angular disperser a change in the incidence angle will be interpreted as a change in the spectrum. Since it contains focussing elements a change of the optical path length between the spectrometer elements influences the coupling into the etalon or the intensity envelope on the camera, both which are difficult to compensate for. Linear drifts on the camera can also be misinterpreted as spectral changes, but those are easier to compensate if not too strong.
The laboratory was not temperature stabilised, leading to temperature variations of about 1°C over the course of one day. Local variations of air temperature can lead to a beam drift or changes in the incidence angles. The gas cell itself was also not temperature stabilised. Measurements could be taken at room temperature and by subsequently heating the gas cell with a heating wire that was coiled around it. Temperatures were measured with a thermometer in the gas cell, but no feedback could be used to equilibrate or fine tune the temperature.

6.6.1. THERMAL EXPANSION OF THE GAS CELL

The thermal expansion coefficient of stainless steel, of which the gas cell consisted, ranges between $\alpha = 9.9 \cdots 17.3\,10^{-6}\mathrm{K}^{-1}$ [19]. A change of 5 K corresponds to a fractional length change of $\delta l = 4.95 \cdots 8.65\,10^{-5}$, which will increase the light path and hence the absorption in the medium accordingly (compare with Figure 6.1). While this is about factor 100 lower than the expected changes in the absorption profile directly to temperature, it can lead to a change of the beam path when not heating the gas cell uniformly. In our measurements, however, thermal effects of the gas cell were much smaller than other noise contributions.

6.6.2. EVACUATION AND FILLING OF THE GAS CELL

The gas cell was evacuated to obtain a reference image to ensure no CO_2 or O_2 respectively was still present when the image was taken. To avoid problems that can occur due to different pressures the cavity was refilled with a neutral background gas, N_2 in our case. Alternatively the gas cell can be flushed with N_2, requiring a gas flow to fill the cell several times in order to be sure that no absorbant remains. Figure 6.13 shows the impact of a gas flow, in this case evacuation of the cell, on the recorded spectrum, which would result in a spectral change when directly interpreting the VIPA image[8]. When completing the procedure the beam went back to his initial position, but the accuracy of this reversal cannot be guaranteed. The strength of the effect can be reduced when filling and evacuating the cavity slower, which would harm the signal quality due to e.g. thermal drift as the time between the measurements is increased. During the measurements a steady gas flow was applied. While this is helpful for avoiding adhesion of gas to the cell walls and enables the pressure controller to compensate for leakage, it also introduces turbulence into the system. The reason for that is that the gas entering the gas cell has room temperature, but the gas in the cell may have a different temperature. This is especially obvious in the case of the measurements of higher temperatures.

(a) equilibrium (b) when evacuating

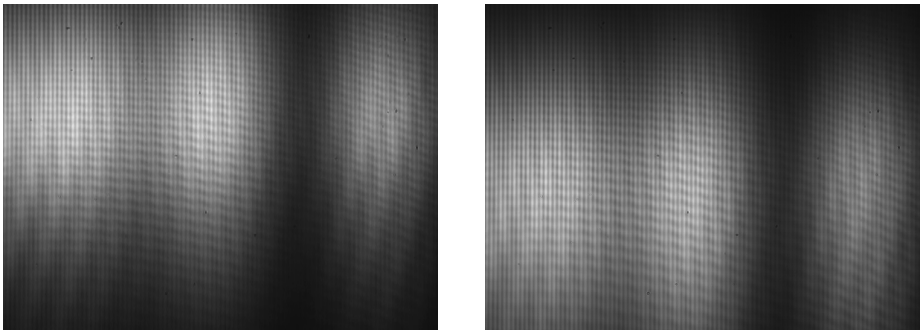

Figure 6.13: The beam is moving when evacuating the cavity resulting in a different VIPA image. (a) shows the state when the system is unperturbed. Image (b) is taken while the cavity is being evacuated.

6.6.3. LINEARITY OF THE CAMERAS

The linearity of the detector, i.e. the linear relation between pixel level and light power, is a big concern in spectroscopy. This is especially tricky when dealing with cameras, in particular in the infra-red, where the technology has not reached the necessary maturity yet. Precise evaluation would require testing the camera pixel by pixel for different camera settings and light intensities. Linearity could be verified for a single pixel and for a limited range of settings. We restricted our measurements to be within this settings. Especially at low power levels nonlinearities were very high, but could be controlled to

[8] Figure 6.13 also shows horizontal lines that impede obtaining a line spectrum (where there is no light, there is no information). The origin of those lines could not be traced with certainty.

some extent for higher power levels. The influence of these nonlinearities can be minimised when only taking pixels with high power levels into account[20]. This would mean cutting off absorption values higher than e.g. 50% and using a fitting procedure to interpolate the lineshape. The noise present in our system did not allow for this approach.

6.6.4. CAMERA NOISE AND DEAD PIXELS

We obtained dark images, i.e. camera images without incident light, with the IR camera. In these images some isolated dead pixels were identified. Less visible, but still present, are predetermined line patterns in the VIPA image, which also should not be present. These readouts also pollute the measured signals. The background can be subtracted from the measured images, but the dead pixels will always be spots in which the camera image cannot be trusted.
In the case of the visible light camera used for O_2 absorption measurements the situation was significantly better having less dead pixels and a lower background.

6.6.5. DYNAMIC RANGE OF THE CAMERA IMAGE ACQUISITION

Digital cameras commonly store image files with a dynamic range of 8bit, i.e. values between 0 and 255, and in the case of coloured images, for the red, green, and blue channel respectively. Scientific cameras allow for a higher dynamic range, which was the case for the infra-red cameras used. They featured 14bit data channels. For the visible camera image, which was only providing 8bit data, averaging had to be applied hoping that power levels would show a probability of being e.g. 40% of the time at 121 and 60% of the time at 120 for a real level of 120.4. The error due to storing data in 8bit can be roughly estimated to relative error $\approx \frac{1}{2}\frac{1}{256} \approx \frac{1}{500} = 0.2\%$.

6.7. CONCLUSION

The limitations of the setup for absorption measurements have been shown. While it is possible to detect whether or not CO_2 is in the cavity, noise and instabilities hamper the performance preventing the intended temperature measurements. Improvements have to be made towards better temperature control within the gas cell and improving the spectrometers. For O_2 measurements the SHG process needs to be stabilised or a different light source has to be used.
It was decided to use fibers as aperture, which can avoid the problems of the wrong spectral read out for angular changes of the propagating beam. Fiber coupling elements however did not cover the needed wavelength range for simultaneous spectroscopy of CO_2 and O_2. In combination with the issues in the SHG the O_2 of the setup was discontinued. The integration of the spectrometers with fibers allowed for measurements outside of the lab, which will be shown in the next chapter. The impact of the improved setup on the in-lab measurements with a CO_2 filled gas cell is shown in Chapter 8.

REFERENCES

[1] B. Edlén, *The dispersion of standard air,* Journal of the Optical Society of America **43**, 339 (1953).

[2] B. Edlén, *The refractive index of air,* Metrologia **2**, 71 (1965).

[3] R. B. Stull, *An Introduction to Boundary Layer Meteorology* (Kluwer Academic Publishers, 1988).

[4] Harvard-Smithsonian Center for Astrophysics (CFA) and V.E. Zuev Institute of Atmospheric Optics (IAO), *Hitran on the web,* website.

[5] L. C. Andrews and R. L. Phillips, *Laser Beam Propagation through Random Media*, edited by E. Pepper (SPIE Press, 2005).

[6] S. A. van den Berg, S. T. Persijn, G. J. P. Kok, M. G. Zeitouny, and N. Bhattacharya, *Many-wavelength interferometry with thousands of lasers for absolute distance measurement,* Physical Review Letters **108** (2012), 10.1103/physrevlett.108.183901.

[7] M. Shirasaki, *Large angular dispersion by a virtually imaged phased array and its application to a wavelength demultiplexer,* Opt. Lett. **21**, 366 (1996).

[8] A. Vega, A. M. Weiner, and C. Lin, *Generalized grating equation for virtually-imaged phased-array spectral dispersers,* Appl. Opt. **42**, 4152 (2003).

[9] S. Xiao and A. Weiner, *2-d wavelength demultiplexer with potential for ≥ 1000 channels in the c-band,* Opt. Express **12**, 2895 (2004), vIPA.

[10] S. Xiao, A. Weiner, and C. Lin, *A dispersion law for virtually imaged phased-array spectral dispersers based on paraxial wave theory,* IEEE Journal of Quantum Electronics **40**, 420 (2004), vIPA.

[11] F. Gori, *Elementi di Ottica* (Accademica, 1995).

[12] B. E. A. Saleh and M. C. Teich, *Grundlagen der Photonik* (WILEY-VCH, 2008).

[13] M. J. Thorpe, *Cavity-enhanced direct frequency comb spectroscopy*, Ph.D. thesis, University of Colorado (2009).

[14] L. Bergmann and C. Schaefer, *Optics of waves and particles*, edited by H. Niedrig (Walter de Gruyter, 1999).

[15] J. Ye and S. T. Cundiff, *Femtosecond Optical Frequency Comb: Principle, Operation, and Applications* (Springer, 2005).

[16] E. Ippen, *Principles of passive mode locking,* Applied Physics B **58**, 159 (1994).

[17] P. N. Butcher and D. Cotter, *The Elements of Nonlinear Optics* (Cambridge University Press, 1990).

[18] R. W. Boyd, *Nonlinear Optics* (Academic Press (Elsevier), 2008).

[19] *The engineering toolbox,* website.

[20] L. Nugent-Glandorf, F. R. Giorgetta, and S. A. Diddams, *Open-air, broad-bandwidth trace gas sensing with a mid-infrared optical frequency comb,* Applied Physics B **119**, 327 (2015).

7

LONG PATH SPECTROSCOPIC TEMPERATURE MEASUREMENTS IN AMBIENT AIR

A setup has been built to measure CO_2 absorption in ambient air with the aim of determining its temperature. Due to water vapor having overlapping absorption lines with a broad range of CO_2 absorption lines, a comparatively weak line had to be selected. Path lengths reached up to 640 m. The experiments have been conducted in the basement of the Applied Sciences building of TU Delft.

7.1. INTRODUCTION

In Chapter 6 we discussed measurements in a controlled environment. In this chapter we discuss the transition that was made towards open cavities relying on the ambient air rather than defined gas composition. This matches the goal of combining the absorption measurements with long distance measuremens better, but has severe drawbacks. The gas composition cannot be chosen, and water (H_2O) has overlapping absorption lines with CO_2. Water leaves a small window in which a CO_2 is visible, although at a very weak level, as can be seen in Figure 7.1. Consequently a very long path length is needed to extract information below the noise level, which is in accordance with the goal of long distance measurements. This fact can be turned into an advantage for longer propagation lengths for which a strong absorption does not allow to distuingish line strengths. However, at longer path lengths beam diffraction as well as turbulences have to be considered. The setup was additionally complicated by the fact that the beam has to leave the laboratory space to reach the corridor of the basement of TU Delft, where a long path setup could be built. Optical tables were placed in the said corridor and fibers were used to guide the light out of the lab. The propagation distance was increased to ~ 640 m before beam distortions reached a level at which the feasibilty of reaching longer path lengths was made questionable.

7.2. ABSORPTION OF AMBIENT AIR

Spectroscopy in ambient air is in some sense more complicated than measurements within a defined reference cell. First of all the gas composition cannot be chosen anymore, but has to be taken from the measurement environment. Spectroscopic lines that were interesting before cannot be targetted anymore since they are hidden behind absorption lines of other gas constituents. Additionally, fluctuations in the air along the beam path complicate the temperature determination. Turbulences, i.e. random changes in the air, affect the propagating path. This is a common problem in earthbound astronomical observations. While many of the techniques from astronomy can be used for improving our setup, factors that could be ignored in vertical propagation have to be taken into account in horizontal propagation. An example for this is water vapour, which can be a significant factor in horizontal propagation, but has little effect on the refractive index in vertical propagation[1]. On average turbulences are greatest near ground-level and fall off exponentially with increasing altitude. In horizontal paths near the surface, strong turbulence is encountered. Multiple scattering has to be accounted for when the strength of the light diffracted by the turbulence becomes comparable to that of the undiffracted light [1]. The interested reader is referred ro the work of Uscinski, Ishimaru, and Strohbehn[2–4].

To compare measurement and simulation atmospheric transfer codes can be used. We obtained theoretical predictions of the absorption behaviour of ambient air from HITRAN data, using the "USA model, mean latitude, winter, H=0"[5]. This corresponds to a gas composition as shown in table 7.1. The exact air composition is subject to change. This is highlighted when comparing the CO_2 content in air through the last years, which is a climate relevant gas and actively monitored. The global average for CO_2 in the atmosphere reached concentrations of more than 400 ppm[6].

Table 7.1: Gas composition according to "USA model, mean latitude, winter, H=0" of the HITRAN database[5].

Component	Abundance in %
H_2O	0.432
CO_2	0.033
O_3	0.000003
N_2O	0.000032
CO	0.000015
CH_4	0.00017
O_2	20.900001
N_2	78.100002

The corresponding absorption of light propagating one kilometer in such air is plotted in Figure 7.1. From Figure 7.1 it can be concluded that the spectrometer needs to be able to measure absorptions with a sub percent accuracy, if there is supposed to be any chance of retrieving the temperature.

7.2.1. OPTIMAL PATH LENGTH

In contrast to chapter 6 the path length in the absorbing medium is no longer constrained by the length of a gas cell, but can be chosen more or less arbitrarily. The question emerges whether there is an optimum propagation length to make the absorption measurement the most sensitive for temperature changes. We assume an exponential decay according to

$$I(l) = \exp(-\alpha(T) \cdot l) \tag{7.1}$$

when denoting the temperature with T, $\alpha(T)$ as the temperature dependent absorption coefficient and $I(l)$ as the intensity after propagating the length l. We are looking for the length L which maximises the temperature change of $I(l)$:

$$L : \max_l \left(\frac{\partial}{\partial T} I(l) \right). \tag{7.2}$$

With

$$\frac{\partial}{\partial T} I(l) = -\frac{\partial \alpha(T)}{\partial T}\, l \exp(-\alpha(T) l) \tag{7.3}$$

this resembles the condition (assuming $\frac{\partial \alpha(T)}{\partial T} \neq 0$)

$$\exp(-\alpha(T) l)\,(1 - \alpha l)\big|_{l=L} = 0 \tag{7.4}$$

or $l = 1/\alpha$. For this propagation length the intensity has been reduced to $1/e$, which results in an absorption of ca. 63%. When comparing with the absorption in Figure 7.1 it can be deduced that the optimum path length is longer than 10 km. This is much longer than the path lengths we aimed to achieve. Equation (7.4) has been obtained by using the first derivative test regarding l.

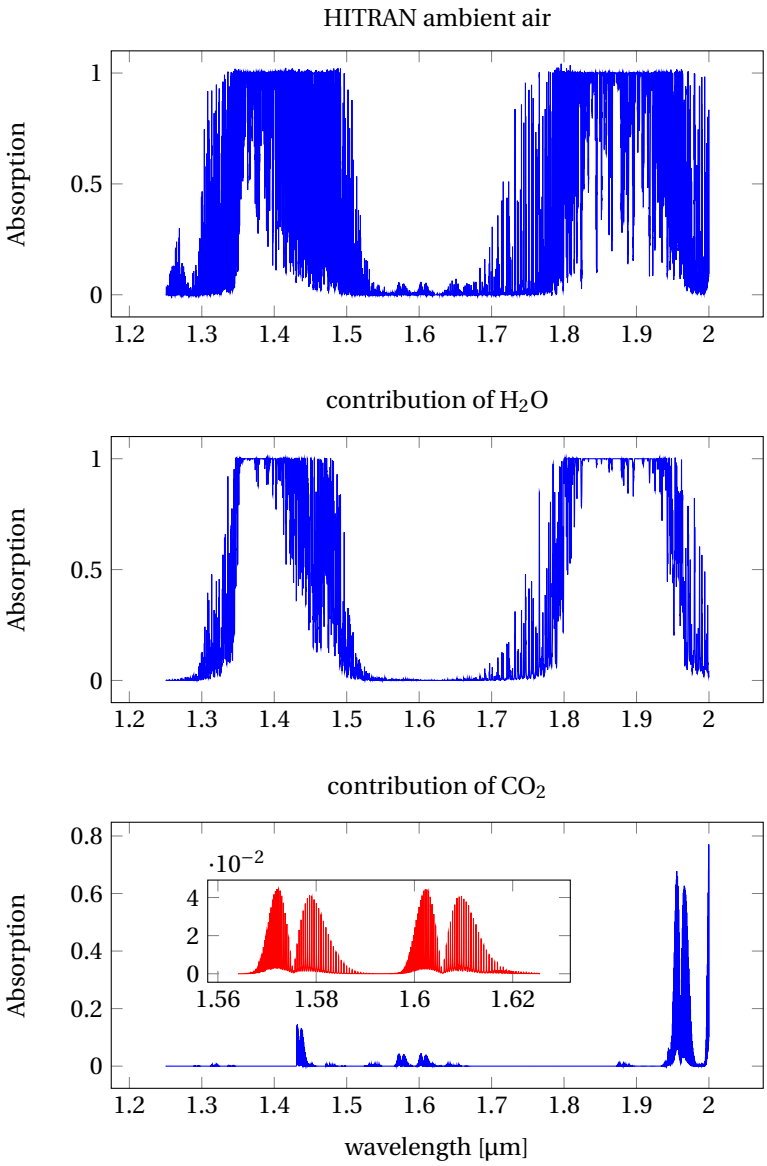

Figure 7.1: Absorption spectra of 1 km of air according to table 7.1, as well as the contributions of water vapour and CO_2 (from top to bottom). The only CO_2 absorption lines within the laser bandwidth, that are not hidden behind water lines, absorb less than 5% of the incoming light, as can be seen in the zoom-in in red colour. Interesting spectral lines seem to be present at higher wavelengths (~ 2µm), unfortunately outside of the laser bandwidth.

7.3. OPTICAL TURBULENCE

In this section we briefly discuss the origin of optical turbulence and methods to reduce their impact in our spectroscopic measurements. The conclusions drawn here are mainly based on [7], other textbooks to look into are [1, 8].
Turbulence refers to random fluctuations of physical quantities in a gas or liquid, such as the velocity, temperature, and refractive index. The latter one is often referred to as optical turbulence. The origin of optical turbulence are small-scale temperature and pressure fluctuations, which the refractive index is sensitive to. Mathematically the variations of the refractive index $n(\mathbf{R}, t)$ at a point $\mathbf{R}$ and time t can be expressed by

$$n(\mathbf{R}, t) = n_0 + n_1(\mathbf{R}, t), \tag{7.5}$$

with $n_0 = \langle n(\mathbf{R}, t)\rangle \approx 1$ and $n_1(\mathbf{R}, t)$ as the random deviations around its mean ($\langle n_1(\mathbf{R}, t)\rangle = 0$). The variations are extremely slow compared to the period of the light and therefore the frequency of the propagating light is not changed by turbulence. After a normalisation to n_0 we can write

$$n(\mathbf{R}) = 1 + n_1(\mathbf{R}), \tag{7.6}$$

which can be expressed as

$$n(\mathbf{R}) = 1 + 77.6 \cdot 10^{-6}\left(1 + 7.52 \cdot 10^{-3}\lambda^{-2}\right)\frac{P(\mathbf{R})}{T(\mathbf{R})} \tag{7.7}$$

for optical and IR wavelengths[7][1]. In Equation (7.7) λ is the wavelength in µm, P the pressure in mbar and T the temperature in K. The equation is simplified for visible light with $\lambda \sim 0.5\,\mu\text{m}$ to[2]

$$n(\mathbf{R}) \approx 1 + 79 \cdot 10^{-6}\frac{P(\mathbf{R})}{T(\mathbf{R})}. \tag{7.8}$$

As such Equations (7.7) and (7.8) serve as an estimate on how strong temperature and pressure fluctuations affect the refractive index.
Turbulences are usually treated in a statistical manner, with different approaches depending on the strength of the perturbation. The effects of turbulence-induced wavefront distortions include spreading of the beam, random variations of the beam position (beam wander), and redistribution of the beam energy (irradiance fluctuations). Additionally the spatial coherence of the laser beam is reduced, which limits the extent to which laser beams can be collimated or focussed, which affects the fiber coupling in our setup. Some of the limitations can be circumvented, such as irradiance fluctuations, which can be averaged out by applying long exposure times of tens of seconds.

[1] In [7] the equation is linked to [9]. However, Equation (7.7) does not directly appear as such in the publication. In [9] Edlén's formula is extended over a wider range of pressure, temperature and composition parameters as well as to the group refractive index[10, 11].
[2] In [1] the equation is $(n-1)10^{-6} = 77.6\,P/T$ instead.

7.4. SETUP

A schematic of the setup can be found in Figure 7.2. A 10 m long single-mode optical fiber was used to direct the beam out of the lab onto a table, which along with two others has been placed in the corridor. The single mode fiber supported wavelengths between 1260 and 1625 nm. Since commercially available connectable fiber couplers were not showing the wanted performance, the beam was manually focussed on the fiber ending. This also allowed for more precise collimation when coupling out of the fiber. Optical breadboards were clamped to those tables to provide stability and alignment anchors for placing the optical components.
Even when blocking the beam in the long path after the fiber coupling, optical power could be detected going to the VIPA. This power is most likely originating from a reflection at the fiber when incoupling and can serve as a reference measurement. For the long path in the corridor, 2" (2 inch = 5.08 cm) optics have been used to show more tolerance towards beam spreading, e.g. due to diffraction. The outer part of the setup has been placed in the corridor of E-wing in the basement of the Applied Sciences building in TU Delft (see Figure 7.3 for reference).

7.5. MEASUREMENTS

Measurements haven been taken for different optical path lengths. With increasing propagation length the signal level in comparison to the noise was steadily inreasing. Several beam widths have been tried to balance the influences of diffraction and turbulence. A wider beam allows for better collimation, but sees more turbulence. Measurements took place during the night and on weekends. This had physical and practical reasons: turbulences are supposed to be smaller during the night. A major source of turbulence is sunlight. Safety regulations, as well as noise considerations, required that no one was working in or in the laboratories adjacent to the corridor the laser beam was sent through. Despite those efforts strong fluctuations were visible on both powermeter (Figure 7.6) and VIPA spectrometer (Figure 7.5). An airflow could be noticed in the staircases the beam had to pass through. Due to the randomness of turbulence, averaging can reduce the variations. Averaging procedures have been applied, but could not reduce the noise sufficiently to obtain a spectrum. The power values shown in Figure 7.6 have been averaged over 500 samples. The VIPA image in Figure 7.7 contains averaged data over 1000 samples.

7.6. CONCLUSION

A setup for a long propagation path in air has been built in the basement of the Applied Sciences building in TU Delft. With a propagation length of 640 m the needed path length for the intended measurements could not be reached. A major concern is the lack of absorption in the used wavelength; a shift towards longer wavelengths seems to be beneficial. In addition to that the VIPA spectrometer suffers from the limitations of the infra-red cameras, which makes the use of a different spectrometer a reasonable consideration. Future experiments should be conducted at a place with a less turbulent environment.

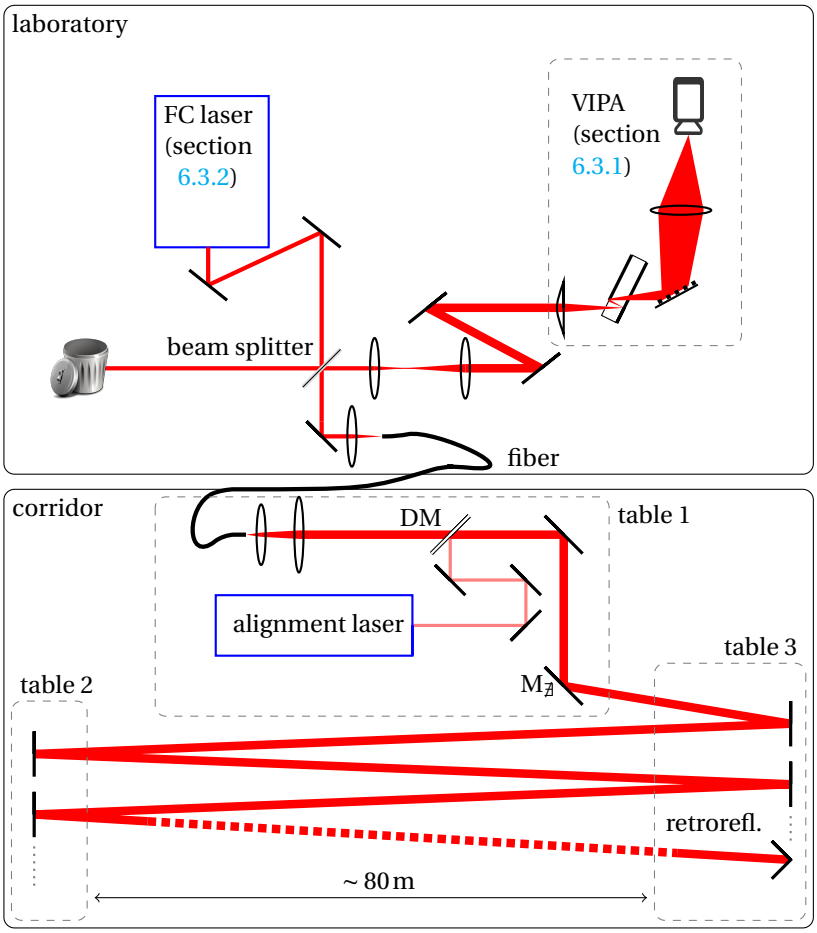

Figure 7.2: In the setup the beam was brought to the corridor, out of the lab, with a fiber. After recollimation the beam was propagated multiple times through the corridor in basement of the E-wing of the Applied Sciences building. To ease the alignment the beam of a visible laser was co-propagated by the virtue of a dichroic mirror (DM). The shown schematic is not entirely matching to the real setup to not impair the visibility of the lines. In the real setup mirror $M_{\not 1}$ does not exist and table 3 is rotated. The retroreflector could be placed on any of the three tables; in the measurement with the longest path length it was fixed to table 1. In theory more (or less) mirrors can be placed on tables to increase the path length. We stopped increasing the path length after ~ 640 m propagation distance.

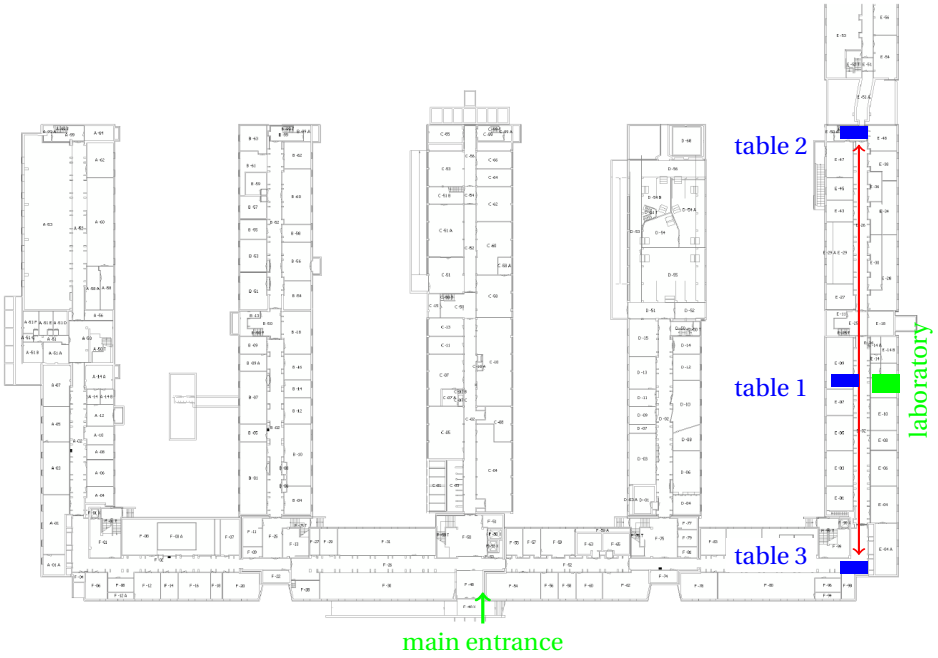

Figure 7.3: Floor plan of the basement of the Applied Sciences building. The corridor that the measurements have been taken in is shown in red, the table as defined in Figure 7.2 are depicted in blue. Main entrance and laboratory in green. The floor plan as been provided by the facility management of the building.

Figure 7.4: Perspective from table 2 when looking towards table 3 (see Figures 7.2 and 7.3 for definition). When taking measurements the lights in the corridor have to be switched off to enhance visibility of the beams and avoid straylight reaching the detectors. In this figure the breadboards have not been clamped to the tables and only the table positions are shown.

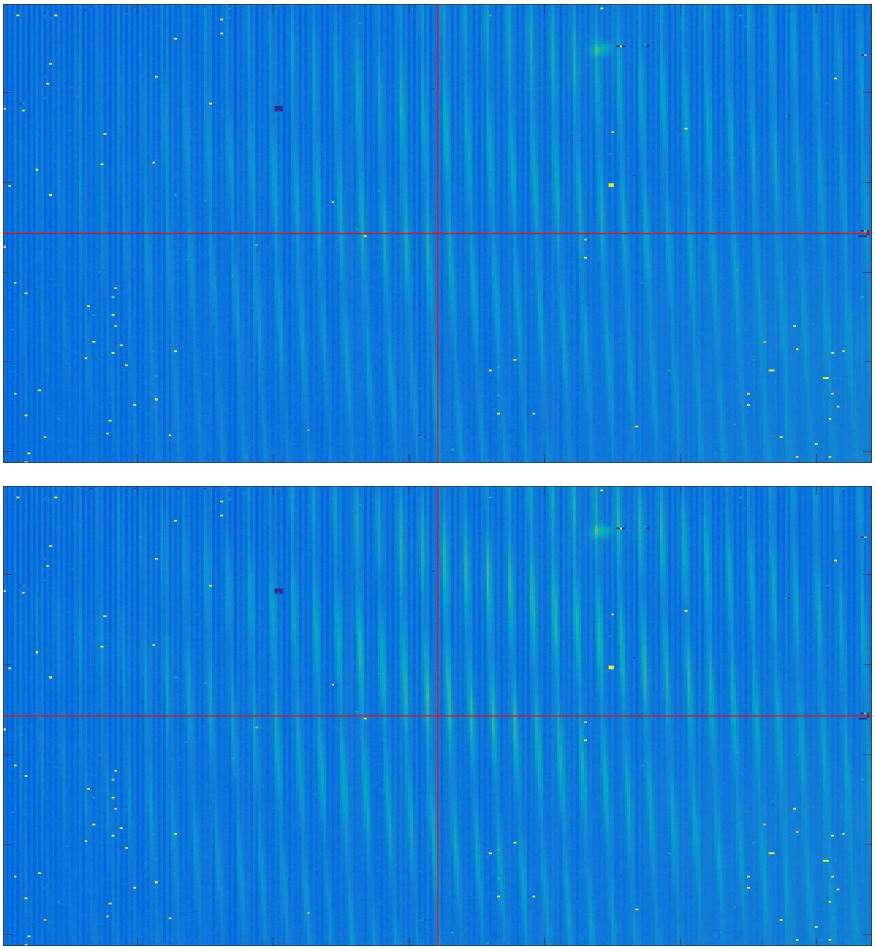

Figure 7.5: VIPA images after 640 m propagation taken less than a second apart. The pattern visible on the VIPA is changing in strength and position, which we attribute to turbulences and mechanical instabilities. The image also shows faulty pixels on the camera.

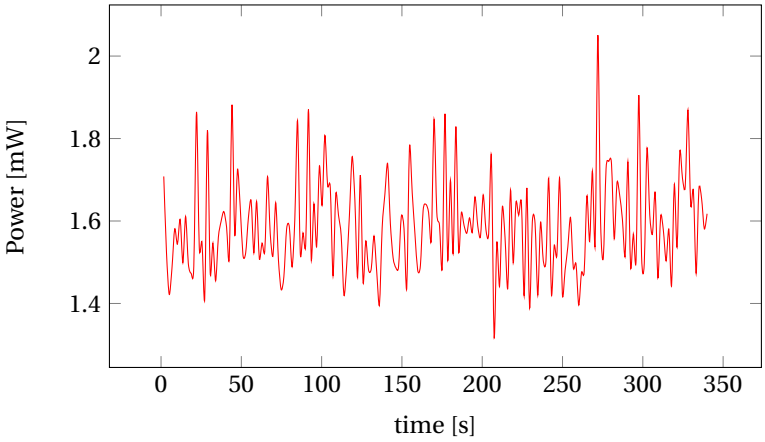

Figure 7.6: Recorded power after a propagation of 320 m in air. The power reflected from the fiber is about 0.85 mW and has not been excluded from the data in this plot. The signal contribution is consequently between $\sim 0.6 \cdots 1$ mW and hence showing variations, that make gas detection impossible if no additional techniques are applied.

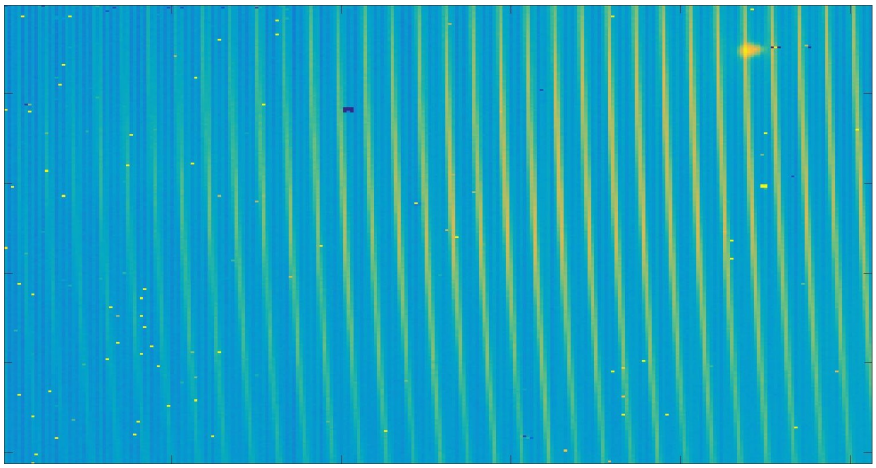

Figure 7.7: VIPA image after averaging over 1000 images with a delay time of 20 ms. The lines visible in Figure 7.5 vanished at the expense of longer acquisition time. The signal when measured with a power meter varied between $\sim 0.07 \cdots 0.3$ mW with an additional background of ~ 0.8 mW originating from reflections at the fiber interface. The path length was ~ 640 m in ambient air.

REFERENCES

[1] J. W. Hardy, *Adaptive Optics for Astronomical Telescopes* (Oxford University Press, 1998).

[2] B. Uscinski, *The Elements of Wave Propagation in Random Media* (McGraw-Hill, 1977).

[3] A. Ishimaru, *Wave Propagation and Scattering in Random Media*, Vol. 1 (Academic Press, 1978).

[4] J. Strohbehn, *Laser Beam Propagation in the Atmosphere* (Springer-Verlag, 1978).

[5] Harvard-Smithsonian Center for Astrophysics (CFA) and V.E. Zuev Institute of Atmospheric Optics (IAO), *Hitran on the web,* website.

[6] N. Oceanic and A. Administration, *Trends in Atmospheric Carbon Dioxide,* website.

[7] L. C. Andrews and R. L. Phillips, *Laser Beam Propagation through Random Media*, edited by E. Pepper (SPIE Press, 2005).

[8] R. B. Stull, *An Introduction to Boundary Layer Meteorology* (Kluwer Academic Publishers, 1988).

[9] J. C. Owens, *Optical refractive index of air: Dependence on pressure, temperature and composition,* Appl. Opt. **6**, 51 (1967).

[10] B. Edlén, *The dispersion of standard air,* Journal of the Optical Society of America **43**, 339 (1953).

[11] B. Edlén, *The refractive index of air,* Metrologia **2**, 71 (1965).

8

IMPROVED GAS CELL EXPERIMENT

To overcome some of the limitations of the setup from Chapter 6 the spectrometer has been rebuilt using fibers as apertures. Measurements on oxygen have not been continued, hence the part of the setup creating second harmonic light has been removed. The spectrometer was mounted on a breadboard to allow for transport to other setups. To access a different wavelength region the output port of the laser with the broadened spectrum was used. The quality of the measured spectra has been improved tremendously, allowing for temperature determination with a relative uncertainty of 3 K.

Parts of this chapter have been published in Review of Scientific Instruments **88**, 053113 (2017) [1].

8.1. INTRODUCTION

The setup from Chapter 6 suffered from the problem that changes in the beam path will show up as a spectral change in the spectrometer. Angular changes will result in a frequency shift of the reconstructed spectrum. Changes of the beam divergence or spot size will affect the intensity envelope, which can lead to a difference in the measured line strength for each individual line. Both effects are difficult to be compensated for. When placing a hard aperture, such as a fiber, the mentioned changes will only affect the overall power of the light coupled into the fiber. This will be visible in a drop of the baseline intensity, which is shared among all the lines. This drop can be compensated with a proper normalisation of the measured data. A welcome side effect of the fiber integration is the segmentation of the setup. In the free space setup modifying the propagation through the gas cell required a realignment of the spectrometer. Both parts of the setup can now be optimised independently. The VIPA spectrometer was mounted on a breadboard to make it portable. It can be used in other experimental setups without the need of rebuilding it from scratch. With the improved stability of the setup, a temperature determination could be undertaken.

8.2. SETUP

To eliminate error sources the scope of the setup has been reduced. As such the measurements on oxygen have not been continued. This way the second harmonic generation (SHG) part of the setup can be omitted. The influence of the SHG of the spectrum was not clear and it was assumed to be a major error contributor. Additionally the fibers were replacing free space optics propagation where possible. This provided hard apertures and allowed for a segmentation of the setup. The setup has been segmented into three main components, which are linked to each other with fibers: laser source, detection cell, and spectrometer. A schematic overview is shown in Figure 8.1. Unless stated otherwise, the used components are unchanged from the Chapters 6 and 7, except of those that have been removed. The individual segments are explained one by one, starting with the laser source.

8.2.1. LASER SOURCE

While the setup in Chapter 6 was optimised for output power to enable efficient second harmonic generation, this laser source was optimised for the available wavelength range. A stronger absorption band can be reached when expanding the bandwidth of the laser. For that reason the light was sent through a highly nonlinear fiber (HNF), which was already part of the frequency comb laser setup, but not used for the former measurements. Sufficient power levels at the wavelengths around 1.44 µm were reached to allow us to investigate the absorption of the $3\nu_3$ band of CO_2 [2]. We coupled the light leaving the laser box into a single mode fiber and sent it to the gas cell.

8.2.2. GAS CELL

The gas cell is mostly unchanged when compared to Chapter 6. The light was collimated after the fiber output and sent through the gas cell. Afterwards the beam was coupled back into a fiber, which was leading to the spectrometer segment. The fiber coupling

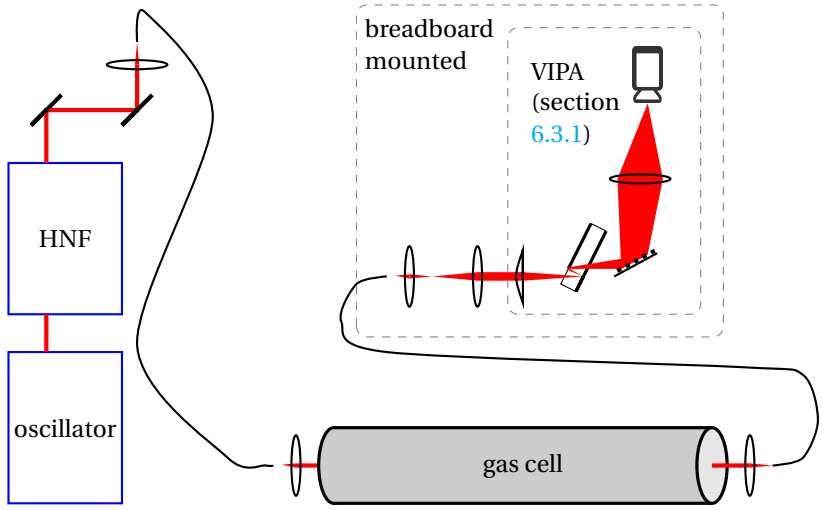

Figure 8.1: Schematic of the new simplified setup. The highly nonlinear fiber (HNF) broadens the spectrum to wavelength regions that are not covered by the laser oscillator. The fibers serve as apertures and simplify guidance of the beam between laser output, gas cell, and spectrometer. The spectrometer is mounted on an aluminum breadboard.

could be optimised every day without influencing other parts of the setup.

8.2.3. VIPA SPECTROMETER

The VIPA spectrometer has been already introduced in Section 6.3.1; it has been modified to be compatible with the fiber coupling. The most noteworthy change is the beam expansion with two lenses after the fiber collimation. The beam size determines the power envelope of the camera image and needs to be optimised to make optimal use of the imaging area. Another advantage is that it allows the compensation of inaccuracies in the fiber collimator. If the light leaving the fiber collimator is still diverging, the lens system can collimate the beam. The VIPA is very sensitive to badly collimated beams, as the cylindrical lens will break circular symmetry and introduce astigmatism in the system. The amount of translation stages for the components of the spectrometer has been reduced. The segmentation of the whole setup made it unnecessary to optimise the spectrometer on a regular basis, since, for example, the transmission through the gas cell, does not affect the beam path in the VIPA spectrometer. In the former setup the components were coupled and could not have been aligned independently. By replacing translation stages with fixed mount segments on the breadboard the components got more stable to mechanical vibrations at the expense of a more cumbersome alignment procedure. This proved beneficial as the alignment has only to be done once, while mechanical vibrations are a continuous problem in optical setups.

8.3. DATA ANALYSIS

We investigated 22 CO_2 lines between 6915 and 6975 cm^{-1}, which show a stronger absorption than the previously inspected lines. To allow for cross-comparison the identified absorption lines are labelled with the line number as taken from HITRAN[3] (see Figure 8.2). The lines of (P44, P42, ...,P2) correspond to (1, 2, ..., 22) following the notation here.

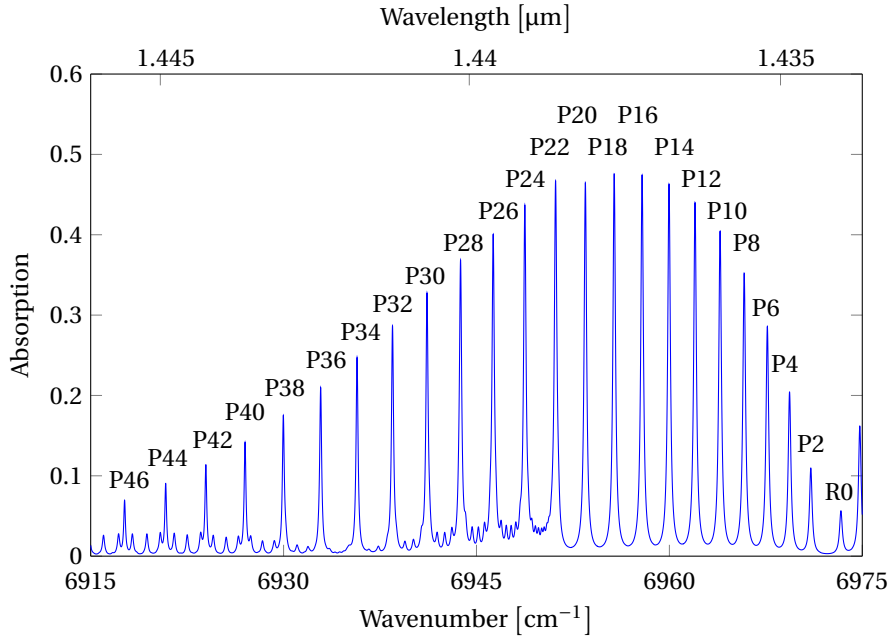

Figure 8.2: Nomenclature of the investigated CO_2 absorption lines as labelled in HITRAN. The shown absorption profile corresponds to 1.5 m of propagation through pure CO_2 at the pressure of 1 atm.

The expected change when increasing the temperature is very small. Figure 8.3 shows that the peak height only shows a weak dependency. However, the peak height is not the best parameter for the comparison. While the strength of an absorption line depends on the population densities of lower and upper states involved in the line transition as well as the number of absorbers, i.e. molecules, exposed to the light, changes in temperature and pressure can also influence the linewidth. An increase in the absorption linewidth would result in a reduced absorption peak height, while the area under the curve remains constant. Therefore we also compared the area under the curve for different samples. A temperature change is affecting the population densities given by the Boltzmann distribution as well as the amount of absorbers in a given volume. Both effects are expected to have an impact on the measured absorbtion strength[4].

The area under the curve can be determined by integrating over a fixed width for each line, or by fitting a line to the measured data. The fitting procedure can level out baseline variations to some extent, and should be the better measure. The overall per-

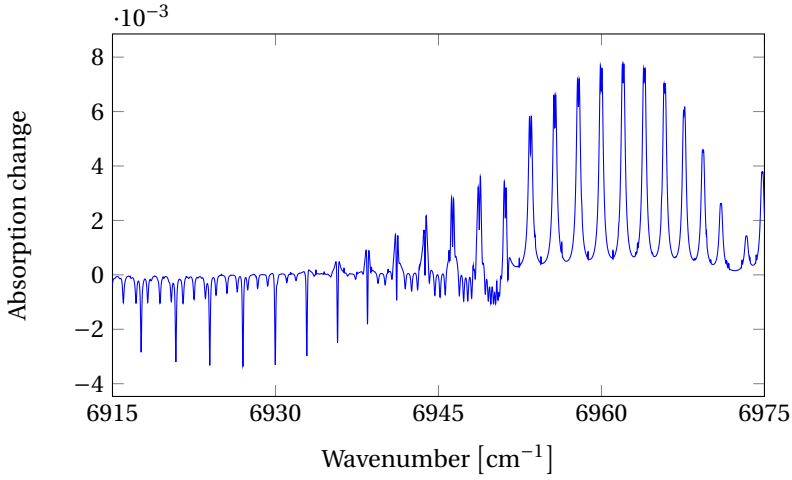

Figure 8.3: Expected change in absorption when increasing the temperature of pure CO_2 by 5 K. The plot shows the absolute difference in absorption (A(T=296 K)-A(T=301 K)) for propagation through 1.5m pure CO_2 at a pressure of 1 atm. The strength of the corresponding absorption lines is shown in Figure 8.2.

formance of the method depends on the ability of the fitting algorithm to match the lineshape properly. A bad fit will introduce a fitting error negating the benefits of the method. In this work we compared the differences in absorption for different temperatures. Another group used a more complicated approach comparing linestrength ratios instead[4, 5]. That method allows for a very accurate temperature determination, but has a more complex data treatment and needs additional measurements. It requires an accurate measurement of pressure and distance to obtain the absorber number density. Here, a separate calculation for these quantities can be omitted. An additional benefit of the method presented in this work is, that the comparison of directly measurable quantities simplifies the noise determination.
We compared two different reference measurements, one with an evacuated cell and one with a cell filled with N_2. We expected the N_2 to show better performance, as the pressure in the gas cell is identical and beam deviations between measurement and reference should be minimised. To verify this assumption, both references have been used.

WAVELENGTH CALIBRATION

The new measurements allowed for a direct comparison of absorption lines. In contrast to the measurements shown in Figure 6.10 the new spectra are clean enough to identify individual lines. This was used for a better wavelength calibration of the spectrometer. The new calibrated spectrum is shown in Figure 8.4.

To double check our calibration we filled the gas cell with lab air instead of the usual neutral background. Lab air contains water vapour, which has absorption lines in the investigated spectrum. Since these water lines are present in the reference image and not the measurement image, they show up as gain instead of loss when taking the ratio. The obtained spectrum with the lab air reference is shown in Figure 8.5. The free spectral

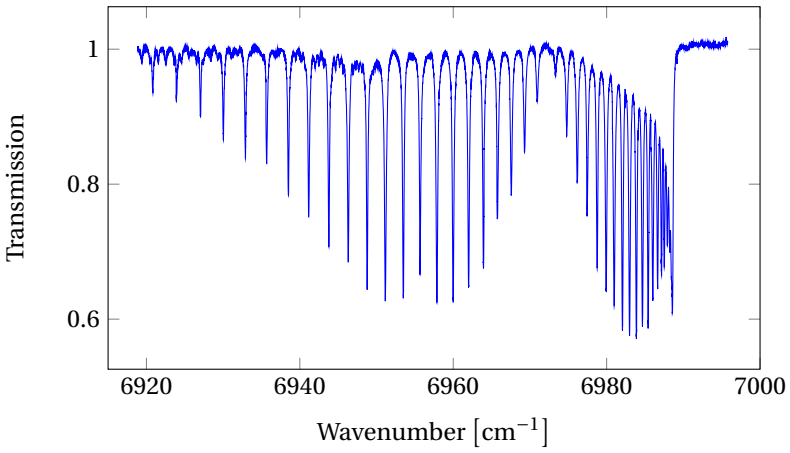

Figure 8.4: Measured CO_2 transmission at at 24.6°C. The new setup shows less noise at the baseline as well as clearer absorption lines than the former setup. This can be seen when comparing this figure with Figure 6.10. The transmission profile is taken by comparing the power of light propagating through 1.5 m of pure CO_2 at a pressure of 1 atm and vacuum. When comparing with Figure 8.2 it seems the power levels are lower than in the simulations, for a better comparison the area under the curve should be compared in contrast to the peak height.

range (FSR) was directly determined from the camera image. This is possible if a clear repeating pattern can be identified on the VIPA image. An independent FSR calibration was with a single mode laser source (Roithner LaserTechnik SPL1430-2-9-PD) leading to the same result as the former method.

It is worth mentioning, that once the absorption lines can be identified and linked to their corresponding HITRAN line, a wavelength calibration is technically not necessary. Further analysis steps only compare line strengths, not line positions. As a consequence line position errors do not contribute to the uncertainty of the presented analysis. If the wavelength is not scaled linearly, shifts in the wavelength can move the beam to a position with higher spread, i.e. with more pixels per wavelength unit. The central position of the absorption lines was only varying by a maximum of 3 pixels; for that small shift higher order wavelength scaling should be negligible. It can have a very strong effect at the sides of the stitching parts, but other errors are still more dominant than the wavelength calibration error. Since the positions of the absorption lines were mostly unchanged when altering the temperature, errors introduced by the wavelength scaling when integrating over a line are present in the measurements for both temperatures and can be calibrated for.

8.3.1. INCREASING THE TEMPERATURE

The temperature of the gas in the cell was increased by heating the gas cell itself with a with heating wire that was coiled around it. The heated gas cell transfers the temperature to the contained gas. Gas entering the gas cell has a different temperature than gas already in the cell. While refilling or evacuating the gas cell this shifted the focus posi-

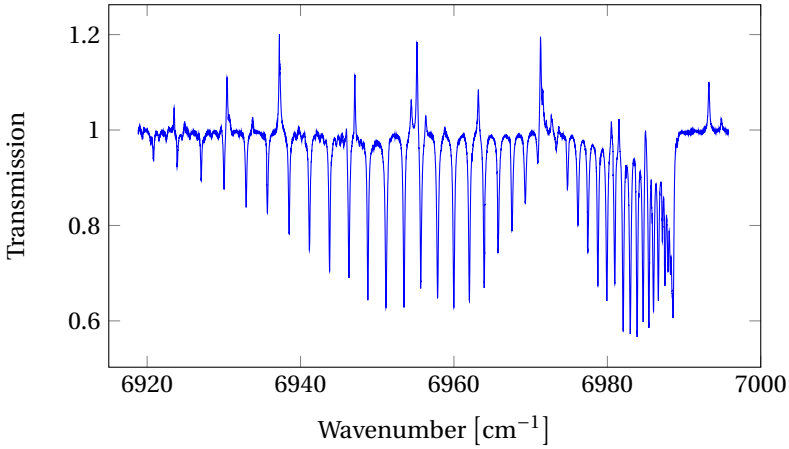

Figure 8.5: Measured spectrum of CO_2 with a lab air reference. When using lab air as a reference water lines will show up as increased transmission. In theory this allows for analysing both gases simultaneously; here it was only used to have a better wavelength definition by comparing lines of both gases.

tion of the fiber coupling lens after the gas cell. At room temperature and for low flow speeds the effect is barely noticeable. When measuring at higher temperatures it leads to a drastically decreased coupling efficiency and hence to a weaker signal on the camera. The focus shift could not be noticed when sending light through an evacuated gas cell; only when it was filled with a gas. Therefore we attribute the increased beam divergence to turbulence in the gas cell[6]. Since one of the measurements has to take place with a CO_2 filled gas cell, it is better to take the reference image with a neutral gas, instead of a vacuum reference. We could obtain better data for images taken with a N_2 background. A decreased coupling efficiency will show up as a reduced base transmission. We normalised the data to always have a transmission of unity at wavenumbers that are not in the direct vicinity of the absorption lines. Figure 8.6 shows unnormalised transmission data for a measurement at a temperature that is 5 K higher than the temperature of the laboratory. Heating the injected gas before it enters the cavity should prevent this baseline drop, as both gases should have the same temperature. This can be done by setting up a second heated gas cell before the measurement cell, from which the gas is fed into the test cell, further complicating the setup. A different approach is to not maintain a steady gas flow. Due to the long time it takes to reach a thermal equilibrium in the gas cell this is not advisable. Gases might adhere to the cell walls and if gas leaks out of the cell the pressure is not constant between two measurements.

We obtained a N_2 reference from a CO_2 filled gas cell by evacuating the gas cell and filling it with a high flow speed (1000 ml_n/min for a N_2 and 500 ml_n/min for CO_2). When the gas cell was completely filled the flow speed was lowered to 10 ml_n/min to maintain a steady gas flow. The flow speeds correspond to the maximal and minimal flow speeds for the respective gases. Depending on the difference between cell and room temperature it could take up to several hours to reach a steady thermal equilibrium. As an alternative

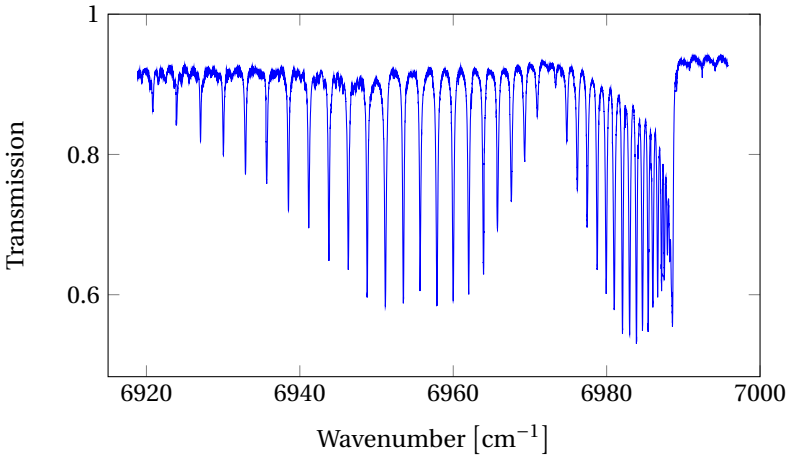

Figure 8.6: Spectral transmission measurement of CO_2 at 29.6°C. Increasing the temperature from 24.6°C to 29.6°C reduces the incoupling efficiency when the gas cell is not evacuated, as can be seen from the baseline not reaching 1. This effect is stronger than the expected change in absorption due to the temperature change. The data is normalised by the dividing by the base transmission value to compensate for this effect.

to the evacuation and refilling of the gas cell we flushed it with a high flow speed for a time much longer than needed to fill it once. After a reasonable amount of time the gas should be completely replaced. Evacuating the cavity before refilling it reduces the time needed to replace the gas and in consequence to a lower error introduced by ambient changes. However, it might be advantageous to not change the pressure in the gas cell to ensure that the cell windows remain steady. When comparing both methods we could not notice significant differences. The time that is needed to flush the gas cell and to reach a thermal equilibrium can be reduced when reducing its volume. This can be done by reducing the cell diameter, which requires a better tracking of the beam path as the entry and exit windows are smaller, or by changing the cell length, which reduces the interaction length of light and gas.

8.3.2. LINE COMPARISON

The HITRAN database provides lineshape parameters for absorption lines resembling Voigt profiles. A Voigt profile is a convolution of a Gaussian and a Lorentzian profile[7]. The Gaussian profile is a consequence of thermal Doppler broadening, while the Lorentzian profile is caused by pressure broadening. Since the spectra were fitted at atmospheric pressure, a Lorentzian profile was chosen for the fitting routine, as it provided better results than a fit assuming a Voigt profile. We also tested fitting a Gaussian curve to the data to confirm the assumption of a predominantly Lorentzian lineshape. Overall the Lorentzian fit provided a better match with the measured values and confirmed this assumption. Simply measuring the peak height does not suffer from errors introduced by the fitting algorithm and was for that reason included in our investigation. The same can be said about the simple integration over a fixed wavenumber range for each in-

dividual line. In that case the integration window was given by the nearest absorption minima encapsulating the peak. The same window was used for the data of both temperatures. Setting new integration windows for the new measurement can correct for a spectral drift that might have occured in between the measurements, but can lead to a different window range. This is especially the case for noisy data, which can make it difficult to find a minimum. The best results could be obtained when flushing the cell with N_2 and applying a multi-line Lorentzian fit. The outcome of this analysis is shown in Figure 8.7 (c), which shows the peak height as obtained by the fitting routine. The same figure contains the peak height and integrated area comparison as well. The temperature difference was 10 K, but would be estimated to be 15 K instead. We only took the lines 14 to 20 into account, because they showed best overlap between measured data and HITRAN. The relative error between the lines is estimated to be 3 K. A proper statistical error analysis would require more data; the estimate is based on the deviation of the predicted shape when looking at the HITRAN profile.
We used Origin to analyse the data and obtain the lineshape fits[8].

The same data analysis has been done for a vacuum reference and a temperaure difference of 5 K. The lower temperature difference should lead to better results. Comparing Figures 8.7 and 8.8 reveals that N_2 is a better reference than vacuum.

In Figure 8.9 a Gaussian lineshape has been assumed, instead of a Lorentzian. In contrast to what has been stated before, it appears to show a better performance than the Lorentzian fit shown in Figure 8.8 (c). This, however, is not reflected in the quality of the fit and did not appear in the analysis at higher temperatures. The quality of the Lorentzian fit alongside the measured spectrum is displayed in Figure 8.10. For most lines the fitted lineshape agrees very well with the measured data. The measured absorption is 20% lower than predicted by HITRAN, but the absorption lines have a similar envelope. Figure 8.2 shows the same lines as Figure 8.10, but with a different line strength. It would be possible to normalise the spectra accordingly. This is an extra calibration step and can improve the accuracy of the temperature determination. It has not been done here to allow for unaltered performance analysis of the proposed temperature measurement method.

8.4. CONCLUSION

The setup from Chapter 6 could be significantly improved. We tried different protocols and references in order to find the optimal method. Comparing the area of Lorentzian line profile fits to measurements with a N_2 reference showed the best performance. While first temperature measurements could be made, the discrepancy between measurement and prediction from HITRAN demands further improvements to make the setup a viable alternative to the conventional methods. The measurement showed an uncertainty of 3K, which can be lowered when averaging over a larger data set. The predicted temperatures were 50% higher than their simulated counter part. A calibration of the spectrometer for a larger set of temperature differences is very likely to remedy this discrepancy. This would entail comparing the line strength changes of all the absorption for smaller temperature differences. The absorption changes can then be compared to the calibration measurement, and given a stable system, reproduced. The temperature can then be retrieved by comparison with a measured data set instead of a prediction based on

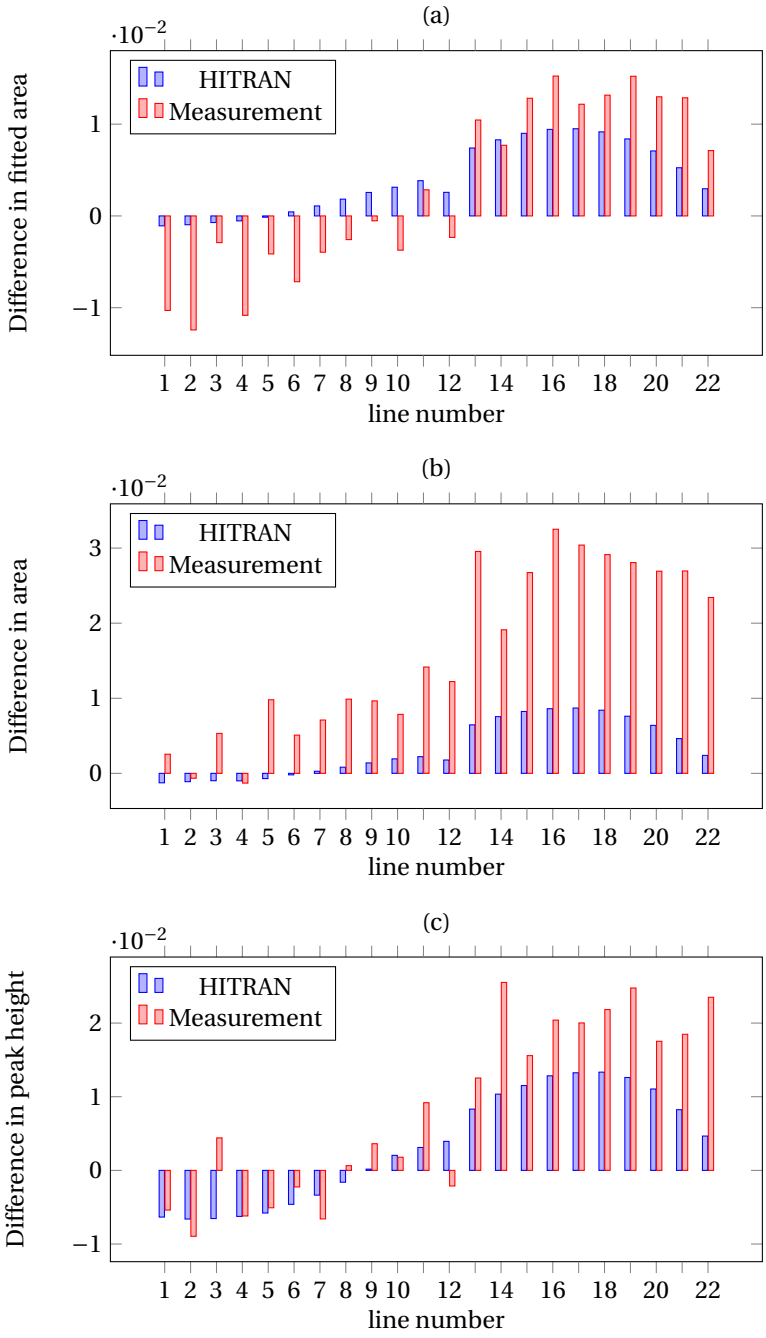

Figure 8.7: Changes in absorption for the different investigated absorption lines when increasing the temperature by ≈ 10 K (from 26.9°C to 36.7 °C). (a) Comparison of the area under the curve for a multi-line Lorentzian profile. (b) Comparison when integrating without assuming any lineshape. In (c) only the peak height was compared. The measurement (shown in red) generally shows a stronger reaction to the temperature changes than HITRAN data (blue). The measured temperature change would be interpreted as 5 K higher than in the HITRAN read-out, with an estimated uncertainty of 3 K. The reference was obtained by flushing the cell with N_2.

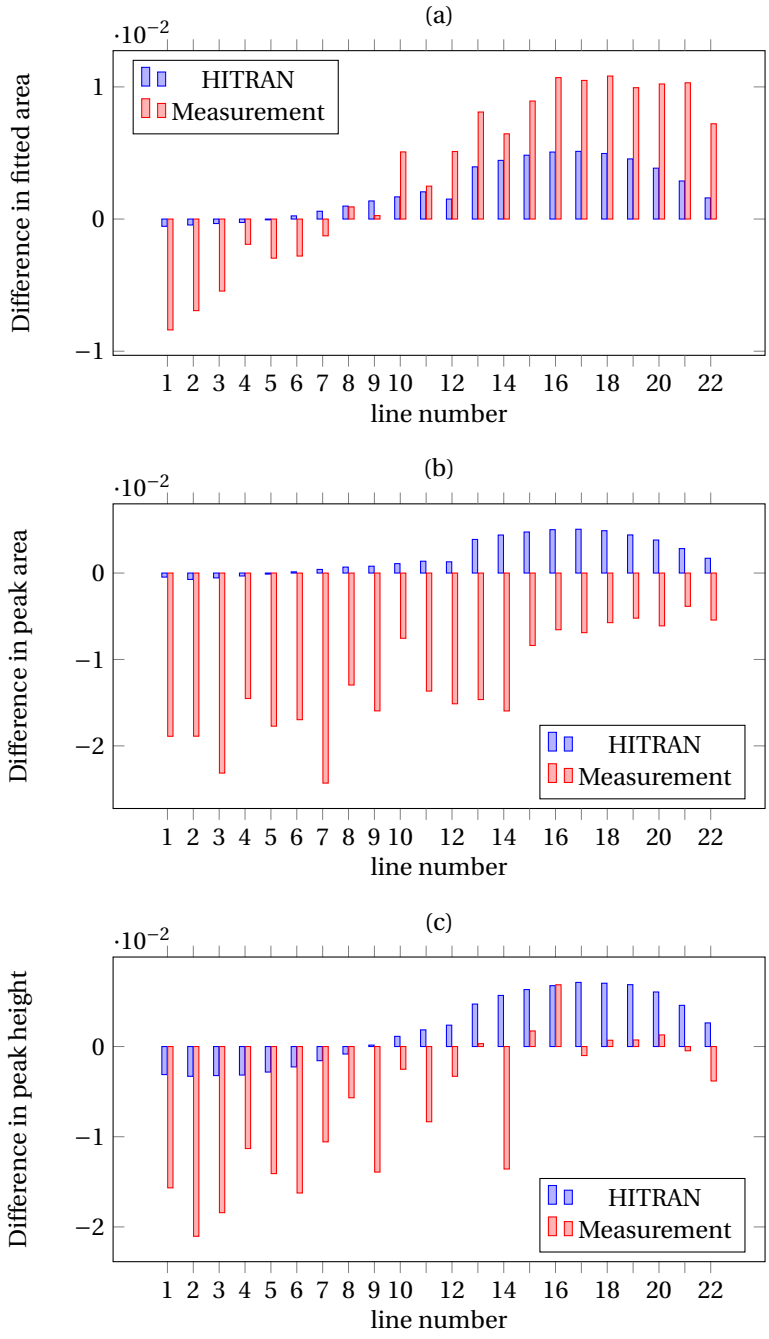

Figure 8.8: Line strength changes for a temperature increase of 5 K (24.6°C to 29.6°C). (a) Comparison of the area under the curve when fitting a Lorentzian profile. (b) Integrated area without line fit. (c) Peak height comparison. Deviations between measurement (red) from the HITRAN data (blue) are more dominant than in the case of a N_2 reference, which is shown in Figure 8.7. It seems as if there is a constant offset of line differences of HITRAN and measurement, as both data series show the same monotony, but the measured values are generally lower.

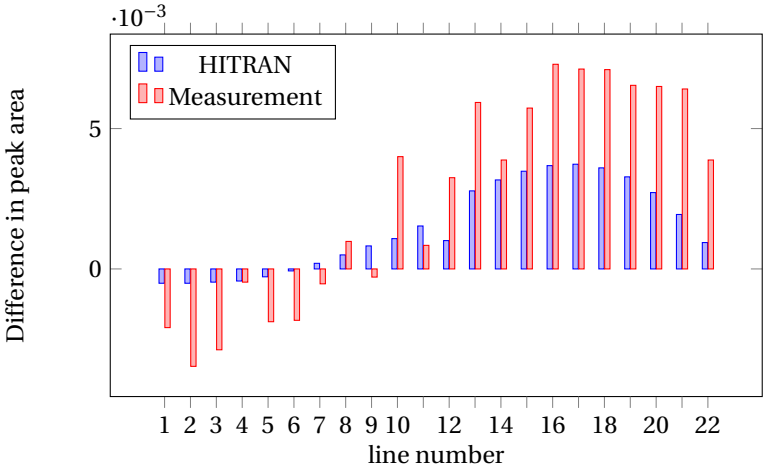

Figure 8.9: The results of the multiline Gaussian fitting. While the results seem slightly better than when using Lorentzian fitting routines, this is not reflected in the fitting and its error estimation. In our interpretation the data obtained from the Lorentzian fit is more reliable.

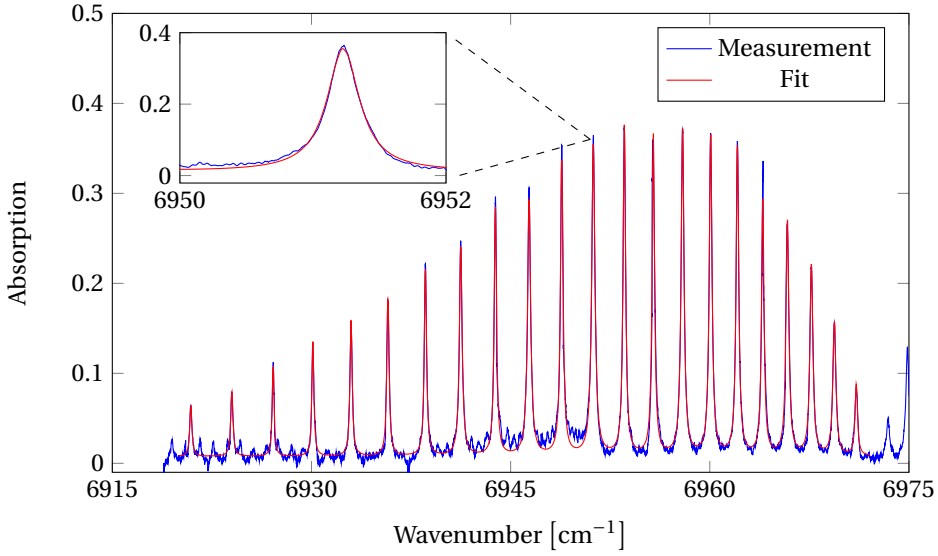

Figure 8.10: Multi-line Lorentzian fit to the measured spectrum at 26.9 °C. The fit is displayed in red, while the measured data are shown in blue. The variation of the baseline as well as the presence of weak lines in the vicinity of the main absorption peaks leads to difficulties in the fitting procedure. Only the main absorption lines were included as fitting parameters. The inset is zooming in on line number 12.
Comparison with Figure 8.2 shows a good qualitative agreement. Comparing the peak heights of measurement and HITRAN shows a disagreement of 20%. Possible explanations for this include instrumental spread of the spectrometer as well as nonlinearity of the camera.

simulated values. A major error source originated from the turbulence caused by the temperature difference between the gas in the cell and the gas injected for the measurement. Preheating the gas can significantly reduce this error, but was not possible in these experiments. The uncertainty of the reported line strength in HITRAN is listed as ≥ 1% and <2% for the investigated lines. This error is higher than the effect to be measured, which clearly suggests an independent calibration of the method is needed. The technique presented here can be very useful in non-contact measurements in hazardous environments, but has very high demands on the stability and calibration of the system due to the weak dependence of the temperature on the absorption. Since only the absorption of the medium has been measured, it can be combined with phase sensitive measurement, such as in the case of distance metrology. A combination of both is expected to allow for a determination of the refractive index of air. The uncertainty of the refractive index directly affects the uncertainty of the distance measurement, as optical and physical path length are multiplicatively linked by it. For certain applications, combining the presented method with optical waveguides or optical cavities can increase the interaction between light and air[9, 10]. This approach, however, cannot be used for long distance measurements.

Ultimately the presented temperature accuracy is comparable to the results reported by Klose et al., featuring a 2.6 K uncertainty[11]. While both setups and methods are similar, the work by Klose et al. made use of absorption lines around 2 µm wavelength range, which were not accessible given our frequency comb laser. It also made use of an independent reference arm to normalize the spectra, which requires a stable and independent link between laser and detector that can be difficult to establish for long distance measurements. While here the pressure was assumed to be constant, their experiment was able to simultaneously obtain the pressure directly from the optical measurement. This was done by determining the linewidths of the absorption lines and compare them to the expected line broadening effects. Unfortunately, the spectral resolution of the VIPA resulted in a relatively large uncertainty (50 out of ~700 Torr). Improvements can be made when using a higher resolution spectrometer.

REFERENCES

[1] A. Hänsel, A. Reyes-Reyes, S. T. Persijn, H. P. Urbach, and N. Bhattacharya, *Temperature measurement using frequency comb absorption spectroscopy of CO_2*, Review of Scientific Instruments **88**, 053113 (2017), http://dx.doi.org/10.1063/1.4984252 .

[2] R. A. Toth, R. H. Hunt, and E. K. Plyler, *Lines intensities of the co_2 σ-σ bands in the 1.43-1.65 μregion,* Journal of Molecular Spectroscopy **38**, 107 (1971).

[3] Harvard-Smithsonian Center for Astrophysics (CFA) and V.E. Zuev Institute of Atmospheric Optics (IAO), *Hitran on the web,* website.

[4] T. Hieta, M. Merimaa, M. Vainio, J. Seppä, and A. Lassila, *High-precision diode-laser-based temperature measurement for air refractive index compensation,* Appl. Opt. **50**, 5990 (2011).

[5] T. Hieta and M. Merimaa, *Spectroscopic measurement of air temperature,* International Journal of Thermophysics **31**, 1710 (2010).

[6] L. C. Andrews and R. L. Phillips, *Laser Beam Propagation through Random Media*, edited by E. Pepper (SPIE Press, 2005).

[7] Demtröder, *Laserspektroskopie - Grundlagen und Techniken*, 3rd ed. (Springer, 1993).

[8] *OriginPro 2015 Software, OriginLab,* .

[9] S. Hanf, R. Keiner, D. Yan, J. Popp, and T. Frosch, *Fiber-enhanced raman multigas spectroscopy: A versatile tool for environmental gas sensing and breath analysis,* Analytical Chemistry **86**, 5278 (2014).

[10] G. Kowzan, K. F. Lee, M. Paradowska, M. Borkowski, P. Ablewski, S. Wójtewicz, K. Stec, D. Lisak, M. E. Fermann, R. S. Trawiński, and P. Masłowski, *Self-referenced, accurate and sensitive optical frequency comb spectroscopy with a virtually imaged phased array spectrometer,* Opt. Lett. **41**, 974 (2016).

[11] A. Klose, G. Ycas, F. C. Cruz, D. L. Maser, and S. A. Diddams, *Rapid, broadband spectroscopic temperature measurement of CO_2 using VIPA spectroscopy,* Applied Physics B **122** (2016), 10.1007/s00340-016-6349-4, cO2.

9

CONCLUSION

Spectroscopic techniques are continously improving. Developments in integrating laser sources and spectrometers allow for smaller devices, and proper packaging ensures a high stability to ambient changes. The emergence of multi-project wafers (MPW) and joint platforms to fabricate such devices significantly lowered the entry costs for developing on-chip devices. We have shown the possibility of creating laser sources capable of spectroscopic measurements on that ground. This was done for initial designs at wavelengths around 1.55 µm, which was the starting point of the COBRA platform that was used for our designs. Two different devices were tested. While the chip presented in Chapter 2 indicated the design allowed for the desired tuning range of the single mode laser, the gain was not sufficient to allow for lasing operation. Chapter 3 featured a design that had longer optical gain section and did not suffer from this design flaw. The available wavelength range has been expanded and measurements at 2 µm have been made possible, which allowed for the design of the on-chip laser shown in Chapter 4. For both devices, the ones centered around 1.55 µm and the ones centered around 2 µm, very wide tuning ranges as well as the possibility of fine tuning capable of sampling spectral linewidths of test gases has been shown. This research will have an impact on future spectroscopic devices as both the integration using an MPW as well as the extension to longer wavelengths mark significant progress in the spectroscopic field. The potential of MPW layouts is not exhausted by the creation of tunable single mode lasers. COBRA developed a fully integrated mode-locked laser with a repetition rate high enough to allow for mode-resolved spectroscopy. The application of this device to distance metrology has been successfully investigated in 5. While the reported accuracy does not contest measurements with Ti:Sapphire laser sources, further progress in this field is expected to narrow down the gap in uncertainty while maintaining the benefits of integration. As such this research is a major step in the transition from laboratory to industry. We used a high resolution VIPA spectrometer for our measurements, but continued research will extend bandwidth and mode spacing of the mode-locked on-chip lasers and allow for combining the source with lower resolution spectrometers. A packaged system with laser source and spectrometer being monolithically integrated can be

expected to emerge in the near future. In a final step the interaction cell can be integrated. While this is difficult on the chip level, as the interaction volume will be very small, hollow core fibers can be filled with the gas sample to be tested. Such hollow core fibers allow for a very long propagation length of the light in the gas, but can be stored in a smaller volume. Current research has not yet exploited to combine all of the different mentioned components, but such a combined device is very likely to find industrial application.

Optics research was not limited to investigating the possibilities of creating smaller devices. Improvements on the stability of mode-locked lasers led to the development of frequency comb lasers, in which repetition rate and carrier envelope phase are kept fixed over very long times. In consequence the temporal and spectral stability is extremely high, which found a significant numbers of applications. The accuracy of frequency comb based metrology reached levels where fundamental limits of uncertainties, such as the uncertainty of the refractive index, were reached. Knowledge of the refractive index requires knowledge of temperature, pressure, and composition of the air the light is travelling through. Of those parameters the first in the list shows the strongest local variation. Current attempts in breaching the uncertainty barrier given by the refractive index variations are based on placing an array of thermometers in the vicinity of the beam path. Since this approach is difficult to follow through for very long distance measurements or hazardous environments, we investigated a temperature determination solely on interpreting an absorption measurement in air. To test the feasibility of this technique we started a setup reading out the absorption profile of CO_2 for two different temperatures. The change in absorption enables extracting the temperature difference. The chapters 6 and 8 were showing measurements in CO_2 filled gas cell, where the latter reduced the setup's complexity to improve the stability and repeatibility of the measurements. With these modifications a temperature resolution of $\sim 3\,\mathrm{K}$ has been achieved. Chapter 7 attempted to take CO_2 measurements in ambient air for a long optical path length in the basement of the university. Ultimately those measurements had to be abandoned as turbulence and dust prevented meaningful measurements. The research of those chapters explored the limits of the suggested techniques and presented realistical estimates for the accuracy of the investigated method. We concluded that further technical improvements are necessary to make it a feasible alternative to competing methods. Those technical improvements, however, are not out of reach and might emerge in the coming decade. For certain applications optical methods might still prove superior when compared to locally placing thermometers, as in the case for measurements of high temperatures in combustion engines, where the temperature accuracies can be much lower, but accessibility is limited. The measurements presented in this work were taken at temperatures of regular ambient conditions.

In summary this thesis studied two very different spectroscopic approaches and investigated possible applications. The first approach was based on a tunable single mode laser source and a broadband detector. The benefits of this method are the narrow linewidth of the laser mode and high maturity of the used detectors. The tuning capabilities of the devices have been shown. A disadvantage of the method is the measurement time,

which is limited due to the scanning of the laser emission line. The duration of the measurements scales with the wavelength range and sampling of the laser emission.
The second approach consisted of periodical or continuous broadband light sources and a spectrometer for the read out procedure. For such a device benefits and caveats can be very similar to the first investigated approach if e.g. a scanning Fourier Transform spectrometer is used. In this work, however, a VIPA spectrometer allowed for obtaining the whole data in a single camera image. Therefore measurements can be much faster and are, if the whole spectrum can be obtained with a single camera image, independent of the investigated wavelength range. For those measurements an infra-red camera needed to be used, which does not reach the stability and dynamic range of infra-red photo-detectors. While a scanning Fourier Transform spectrometer allows for a variable spectral resolution, the specrometer used here used angular dispersers and is of fixed resolution.
Both of the investigated approaches can have strong advantages depending on the requirements of the setup. A spectroscopist is advised to carefully select which method suits best when planning an experiment.

A

APPENDIX

A.1. USED EQUIPMENT

This section listes the equipment used for the measurements in the corresponding chapters. For the chapters not listed here, the equipment is mentioned in-text. For the other chapters adding the components in-text impeded the readabilty.

A.1.1. CHAPTER 2

The shown measurements were done in TU Eindhoven. The laser diode driver was a Thorlabs LDC8005 in a chassis of Thorlabs PRO8000. The output light was coupled into a tapered fiber (OZ-optics TSMJ-EA-1550-9/125-0.25-7-2.5-14-1-AR). Spectra were read out with a Yokogawa AQ 6375 optical spectrum analyser while the voltage tuning was facilitated by a National Instruments NI9923 in cDAQ-9178 chassis.
Additional measurements took place in TU Delft (data not shown in this work). Laser diode driver and voltage controller were identical to the devices used in TU Eindhoven. The spectrum analyser wass an Ando AQ-6315A. The fiber coupling used a WT&T CL5 tapered cone lensed fiber.

A.1.2. CHAPTER 3

The equipment used in Chapter 3 is listed in Table A.1.

A.1.3. CHAPTER 5

Table A.2 lists the equipment needed to repeat the measurements of Chapter 5. This includes active and passive components.

A.1.4. CHAPTER 6

A XenICs XEVA-FPA-1.7-640 camera was used to capture the VIPA images in the infrared wavelength region. For visible light an ImagingSource DMK 72BUC02 obtained the data. The frequency comb was bought from Toptica and Menlo Systems and is based on erbium-doped fibers. Mass flow and pressure controllers have been purchased from

A

Table A.1: Used equipment for measurements described in Chapter 3.

type	manufacturer/product
Lensed fiber	OZ-optics TSMJ-EA-1550-9/125-0.25-7-2.5-14-1-AR
Laser diode controller	Thorlabs PRO8000/LDC8005
Voltage sources	National Instruments NI9269 and NI9923 in cDAQ-9178 chassis
Optical spectrum analyzer	Yokogawa AQ 6375
High resolution OSA	APEX Technologies AP2041A
Fast photodiode	u2T-XPDV-1020R
Electrical spectrum analyzer	Agilent E44484
Acetylene cell	Thorlabs CQ09050-CH12
Optical power meter (fiber)	Agilent 81636B
Optical power meter (free space)	Newport 1835-C

Bronkhorst (F-201CV-1K0-RAD-22-V and P-702CV-1K1A-RAD-22-V). The gas cell was 1.5 m long and had entrance windows with 1 inch diameter, that were transparent for the IR light. Evacuation was done by connecting a Vacuubrand MD1 vacuum pump to the pressure controller. The thermometers are from Pico Technology (PT-104). The mirrors before the SHG crystal were dielectric mirrors from Thorlabs; after the wavelength conversion silver mirrors were used (BB1-E04 and PF10-03-P01). The parabolic and the dichroic mirror were purchased from Thorlabs as well (MPd254254-90-P01 and DMSP1180). The VIPA etalons were purchased from LightMachinery (OP-6721-1686-4) and Precision Photonics (S-LAH71) and combined with Thorlabs gratings (GR50-1208 and GR50-1210).

A.2. MAXWELL'S EQUATIONS

Maxwell's equations, describing electromagnetic phenomena, are

$$\nabla \cdot \mathbf{D}(\mathbf{r}, t) = \rho(\mathbf{r}, t) \tag{A.1}$$

$$\nabla \times \mathbf{H}(\mathbf{r}, t) - \frac{\partial}{\partial t}\mathbf{D}(\mathbf{r}, t) = \mathbf{J}(\mathbf{r}, t) \tag{A.2}$$

$$\nabla \times \mathbf{E}(\mathbf{r}, t) + \frac{\partial}{\partial t}\mathbf{B}(\mathbf{r}, t) = 0 \tag{A.3}$$

$$\nabla \cdot \mathbf{B}(\mathbf{r}, t) = 0 \tag{A.4}$$

as found in [1]. It is common in optics to assume no external charges ($\rho = 0$). $\mathbf{D}$ and $\mathbf{H}$ are defined as follows:

$$\mathbf{D}(\mathbf{r}, t) = \varepsilon_0 \mathbf{E}(\mathbf{r}, t) + \mathbf{P}(\mathbf{r}, t) \tag{A.5}$$

$$\mathbf{H}(\mathbf{r}, t) = \frac{1}{\mu_0}\mathbf{B}(\mathbf{r}, t) - \frac{1}{\mu_0}\mathbf{M}(\mathbf{r}, t). \tag{A.6}$$

Table A.2: Used equipment for measurements described in Chapter 5.

type	manufacturer/product
Lensed fiber	OZ-optics TSMJ-EA-1550-9/125-0.25-7-2.5-14-1-AR
Laser diode controller	Thorlabs PRO8000/LDC8005
DC voltage source	National Instruments NI9923 in cDAQ-9178 chassis
Fast photo-detector	Newport 818-BB-35F
Spectrum analyzer	RIGOL DSA1030
Booster optical amplifier	Thorlabs S9FC1004P
Circulator	Thorlabs 6015-3-APC
RF signal generator	Rohde & Schwarz SMB100A
Translation stage	PI M-112.1DG
Stage motion controller	PI C-863 DC
VIPA etalon	Precision Photonics S-LAA71
Post-disperser grating	Spectrogon UK G1100 31x50x10 NIR
Reference laser	Agilent 6015-3-APC in 8163B mainframe
IR camera	XenICs XEVAFPA-1.7-640

It is common to rewrite (A.5) and (A.6) to $\mathbf{D} = \varepsilon\mathbf{E} = \varepsilon_r\varepsilon_0\mathbf{E}$ and $\mathbf{B} = \mu\mathbf{H} = \mu_r\mu_0\mathbf{H}$ when staying in the field of linear optics.

A.3. STOKES RELATIONS

The current section is based on the *The Stokes Treatment of Reflection and Refraction* as found in the 4th edition of *Optics* by Hecht[2].
Consider a situation as in figure A.1(a): An incoming wave E_0 is partially reflected ($E_0 \cdot r$) and refracted ($E_0 \cdot t$) on an interface, with r and t being reflectivity and transmittivity with respect to the field. A situation identical to the one in (a), except with reversed directions, has to exist for reciprocal systems (see A.4). In this case the two fields are incident on the interface, $E_0 t$ and $E_O r$, which themselves also produces fields, such as in figure A.1(c). Comparing (b) and (c) we get

$$E_0 t t' + E_0 r r = E_0 \tag{A.7}$$
$$E_0 r t + E_0 t r' = 0. \tag{A.8}$$

The results should be independent of E_0, which is a factor in both equations. For $E_0 \neq 0$ this identical to

$$t t' = 1 - r^2 \tag{A.9}$$
$$r' = -r. \tag{A.10}$$

(A.10) shows the famous 180° phase shift on reflection, without giving an indication whether it occurs when reflecting on an optically denser ($n_2 > n_1$) material, or the other

A

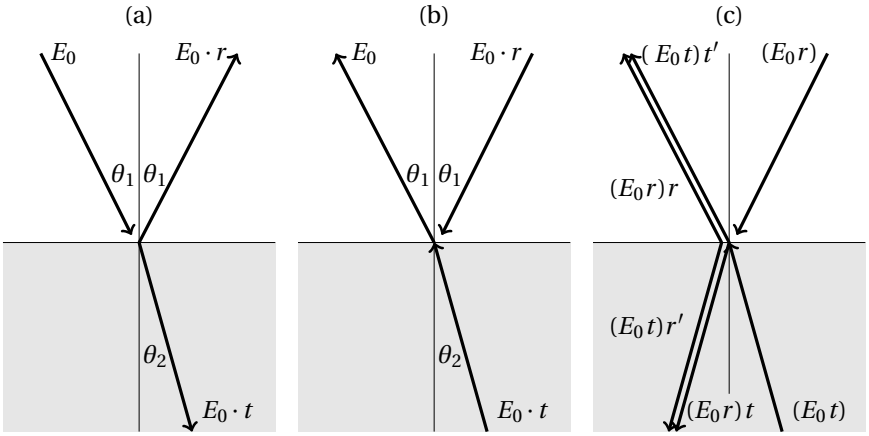

Figure A.1: Reflection and transmission of a beam with E_0 impinging on a surface. (a) Part of the beam is refracted, another part reflected. (b) An inverted path has to exist which reproduces identical behaviour save the propagation direction (this is assuming lossless interaction). (c) Adding beams resulting from the interaction of the new incoming beams with the interface. The primed index denotes opposite interaction direction to the one in (a).

way around.
So far the different angles of incidence have been ignored, reducing the validity to the case of perpendicular incidence. Including angles into the considerations we get

$$t(\theta_1)\, t'(\theta_2) = 1 - r^2(\theta_1) \tag{A.11}$$

$$r'(\theta_2) = -r(\theta_1). \tag{A.12}$$

With the use of Snell's law of refraction ($n_1 \sin\theta 1 = n_2 \sin\theta 2$) one can conclude phase relations for both propagation directions.

A.4. RECIPROCITY PRINCIPLE

The reciprocity principle states, that the physcial situation of a system has to be replicated when interchanging emitter and receiver; assuming that all the elements are reciprocal. Helmholtz has formulated[1], as cited in [3], the following theorem:
Vom Punkt A gehe das Einheitsquantum an Licht von bestimmer Farbe, polarisirt nach einer bestimmten Richtung α, in einer solchen Strahlrichtung aus, dass nach einer Reihe von Speigelungen und Brechungen schliesslich in B das Quantum x ankomme, und zwar nach einer Richtung β polarisiert. Lassen wir nun von diesem Ziel rückwärts in der umgekehrten Richtung des Endstrahls das Einheitsquantum nach β polarisirten Lichtes, von derselben Farbe ausgehen, so kommt nach allen jenen reciproken und reversibelen Vorgängen, die das Licht erleidet, dasselbe Quantum x also derselbe Bruchteil nach α polarisirten Lichtes am Ausgangsorte an.
It is stated that a light ray propagating from $A \rightarrow B$ has the same features in A and B as

[1] In *Theorie der Wärme*, I, 3, §42 according to [3]

the ray going $A \leftarrow B$ if only reversible processes are involved. One has to be very careful when considering systems with losses or treating extended light fields and apertures, the latter case being discussed in [3].

A.5. SYMMETRIES IN COUPLERS

Symmetries between the coupling coefficients in a coupler such as in figure A.2 are developed, as seen in Wouter Westerveld's PhD thesis[4]. The outputs are governed by

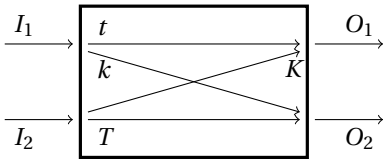

Figure A.2: Input and output for a 2 × 2-coupler.

$O_1 = tI_1 + KI_2$ and $O_2 = kI_1 + TI_2$, which can be written in matrix form as

$$\begin{pmatrix} O_1 \\ O_2 \end{pmatrix} = \begin{pmatrix} t & K \\ k & T \end{pmatrix} \begin{pmatrix} I_1 \\ I_2 \end{pmatrix} = U \begin{pmatrix} I_1 \\ I_2 \end{pmatrix}. \tag{A.13}$$

We assume a lossless coupler with $|I_1|^2 + |I_2|^2 = |O_1|^2 + |O_2|^2$. Calculating $|O_1|^2 + |O_2|^2 = O_1 O_1^* + O_2 O_2^*$ yields

$$\begin{aligned} & O_1 O_1^* + O_2 O_2^* \\ =& (tI_1 + KI_2)(tI_1 + KI_2)^* + (kI_1 + TI_2)(kI_1 + TI_2)^* && \text{(A.14)} \\ =& tt^* I_1 I_1^* + KK^* I_2 I_2^* + kk^* I_1 I_1^* + TT^* I_2 I_2^* \\ & + I_1 I_2^* (K^* t + kT^*) + I_1^* I_2 (Kt^* + kT^*) && \text{(A.15)} \\ =& \left(|t|^2 + |k|^2\right) |I_1|^2 + \left(|T|^2 + |K|^2\right) |I_2|^2 + I_1 I_2^* (K^* t + kT^*) + I_1^* I_2 (Kt^* + kT^*) && \text{(A.16)} \\ \stackrel{!}{=}& I_1 I_1^* + I_2 I_2^* \end{aligned}$$

Setting $I_{1,2} = 0$ respectively we can immediately conclude that

$$|t|^2 + |k|^2 = 1 \qquad |T|^2 + |K|^2 = 1. \tag{A.17}$$

The remaining $I_1 I_2^* (K^* t + kT^*) + c.c. = 0$ has to be valid for all combinations of I_1 and I_2, and therefore

$$K^* t + kT^* = 0 \qquad Kt^* + k^* T = 0. \tag{A.18}$$

We calculate $\left(U^\dagger = U^{*T}\right) U = I$ using (A.17) and (A.18). For a quadratic matrix A the inverse matrix can be defined as

$$A = \begin{pmatrix} a & b \\ c & d \end{pmatrix} \qquad A^{-1} = \frac{1}{\det(A)} \begin{pmatrix} d & -b \\ -c & a \end{pmatrix} \tag{A.19}$$

A

for $\det(A) \neq 0$[5]. With $\det(U) = D = tT - kK$ we get the condition

$$\frac{1}{D}\begin{pmatrix} T & -K \\ -k & t \end{pmatrix} = \begin{pmatrix} t^* & k^* \\ K^* & T^* \end{pmatrix}. \tag{A.20}$$

The determinant of a unitarian matrix can only have a phase, i.e. $|\det(U)| = 1$. From (A.20) it is clear that $T = Dt^*$ and $K = -Dk^*$. When choosing $D = 1$ we finalise with

$$\begin{pmatrix} O_1 \\ O_2 \end{pmatrix} = \begin{pmatrix} t & -k^* \\ k & t^* \end{pmatrix}\begin{pmatrix} I_1 \\ I_2 \end{pmatrix}. \tag{A.21}$$

A.6. DERIVATION OF (6.20)

We show the outcome of a Taylor expansion of (6.19) reaching (6.20). We start with

$$\mathrm{FSR} = \frac{c}{2t\cos(\theta_i) - 2t\sin(\theta_i)\theta_\lambda - t\cos(\theta_i)\theta_\lambda^2}. \tag{A.22}$$

A Taylor expansion corresponds to

$$\mathrm{FSR}(\theta_\lambda) = \mathrm{FSR}(0) + \mathrm{FSR}'(0)\cdot\theta_\lambda + \frac{1}{2}\mathrm{FSR}''(0)\cdot\theta_\lambda^2 + \cdots \tag{A.23}$$

where $\mathrm{FSR}' = \frac{\partial \mathrm{FSR}}{\partial \theta_\lambda}$ and similar for higher orders. We define the denominator $D(\theta_\lambda)$ according to $\mathrm{FSR} = \frac{c}{D}$, hence

$$D(\theta_\lambda) = 2t\cos(\theta_i) - 2t\sin(\theta_i)\theta_\lambda - t\cos(\theta_i)\theta_\lambda^2. \tag{A.24}$$

The calculation of the components of (A.23) is as follows:

$$\mathrm{FSR}(0) = \frac{c}{2t\cos(\theta_i)} \tag{A.25}$$

$$D(0) = 2t\cos(\theta_i) \tag{A.26}$$

$$\mathrm{FSR}'(\theta_\lambda) = -\frac{c}{D(\theta_\lambda)^2}\left(-2t\sin(\theta_i) - 2t\cos(\theta_i)\theta_\lambda\right) \tag{A.27}$$

$$\mathrm{FSR}'(0) = -\frac{c}{[2t\cos(\theta_i)]^2}\left(-2t\sin(\theta_i)\right) = \frac{c}{2t\cos(\theta_i)}\tan(\theta_i) \tag{A.28}$$

$$\mathrm{FSR}''(\theta_\lambda) = 2\frac{c}{D(\theta_\lambda)^3}\left[-2t\sin(\theta_i) - 2t\cos(\theta_i)\theta_\lambda\right]^2 + \frac{c}{D(\theta_\lambda)^2}2t\cos(\theta_i) \tag{A.29}$$

$$\mathrm{FSR}''(0) = \frac{2c}{(2t\cos(\theta_i))^3}4t^2\sin^2(\theta_i) + \frac{c}{(2t\cos(\theta_i))^2}2t\cos(\theta_i) = \frac{2c\tan^2(\theta_i) + c}{2t\cos(\theta_i)} \tag{A.30}$$

Inserting (A.25), (A.28), and (A.30) into (A.23) ignoring higher order terms yields

$$\mathrm{FSR} = \frac{c}{2t\cos(\theta_i)}\left[1 + \tan(\theta_i)\theta_\lambda + \left(\frac{1}{2} + \tan^2(\theta_i)\right)\theta_\lambda^2\right], \tag{A.31}$$

which is identical to (6.20).

REFERENCES

[1] J. D. Jackson, *Classical Electrodynamics*, 3rd ed. (John Wiley and Sons, 1999).

[2] E. Hecht, *Optics*, 4th ed. (Addison-Wesley, 2001).

[3] M. Minnaert, *The reciprocity principle in lunar photometry*, Astrophysical Journal **93**, 403 (1941).

[4] W. Westerveld, *Silicon photonic micro-ring resonator to sense strain and ultrasound*, Ph.D. thesis, Delft University of Technology (2014).

[5] I. N. Bronstein, K. A. Semendjajew, G. Musiol, and H. Mühlig, *Taschenbuch der Mathematik*, 7th ed. (Verlag Harri Deutsch, 2008).

ACKNOWLEDGEMENTS

They say *it takes a village to raise a child*, and in the same fashion a PhD is not solely an individual achievement. Reaching this state involved the support of many many people, and fortunately this document allows for a section dedicated to them.

It is the tradition to thank the promotor first. Therefore I want to thank Prof. Urbach first for enabling me to do my PhD in the Optics Research group. I also want to express my gratitude to Nandini Bhattacharya, who supervised me during this time. I apologise for every grey hair I must have caused. You were helping in every possible way and where I saw impossible you saw difficult. I hope I did not manage to take that optimism from you.
Furthermore I am thankful to all the committee members for reviewing my thesis and providing feedback.

Another big thanks is owed to Sylwester Latkowski. You were in many ways my supervisor from Eindhoven. The STW project would have not reached this point without your contribution, because you did not only work on the development of the technology, but also on the accessibility for other labs. Thank you for this very smooth and pleasant collaboration. This was aided by Erwin Bente, who I want to thank as well.

The Dutch translation of the summary was provided by Iterio Degli-Eredi. Thanks a lot, you really helped me out. I want to thank Frederikke Chang Winterberg, who designed the cover for this dissertation.

In the optics research groups I made a lot of friends. Among the first were Nitish Kumar (a.k.a. Boss Nitish) and Gopika Ramanandan (or actually GKPR, but that is just too long). You are awesome people and I enjoyed every event we had together. I feel bad for always praising your cooking skills first (they are truly remarkable) since you are amazing on so many levels other than that. Even Vihaan, the newest member of your family, helped by assisting me in my active immunisation endeavours. Also thanks to Luca Cisotto, *my brother from another mother*. Just watching the adventures you get yourself into is a true delight. Please always put a name tag on your valuable belongings. I spent a lot of time in the office with Nishant Kumar, Ying Tang, and Daniel Nascimento Duplat. One cannot ask for better office mates. I enjoyed the discussions with you, scientific and sometimes not so scientific ;-). A thank you also to my other office mates Sven van Haver and Peiwen Meng (Doris) with whom I shared the office for a much shorter time. Alessandro "you should do something" Polo, thank you for the very entertaining discussions. Thanks to Adonis Reyes Reyes for making for an easy start in the Netherlands, by helping me in the lab and showing me the *wild* nightlife of Delft. Thanks to Tania Vazquez Faci for keeping check on that guy, he is a danger to himself ;-) Thank you Sarathi (speak: Shaa-Row-Tea)

Roy for showing Nitish that there is a life beyond cricket and for showing that even people at our age can afford doing some sports. Luiz Couto, you probably thought I would forget you; no way. Stay awesome, old sport. I want to thank Katsiaryna Ushakova for organising social events that would get you through a cold winter. Thank you Hamed Ahmadpanahi (I give up if that's not the right name), in the next laser tag game I will not let you get the better of me! Thanks to Edgar Rojas for enduring all the bad jokes at his expense. Thanks Matthias Strauch for proving that good things can come from bad federal states. Priya Dwivedi, I am thankful for all the jokes you set yourself up to by not thinking about your words carefully. The same can be said about Lei Wei. I will never forget Fellipe Grillo Peternella's discussion in a German restaurant. You quickly became an integral part of optica. Kefei Hei, it was a great collaboration with you during my final days in the group. I appreciate the way you discussed your concerns and thought of solutions to the occurring problems, as well as the hard work you put into the measurements. A big *thanks* to Yifeng Shao for his surprise back massages. I am sure others will appreciate it as much as I did ;-) Thanks to Zhe Hou for being a bridge in European-Chinese communication and providing translations when we were all in dire need of it. Another thanks to Marco Mout for doing the same, but with Dutch instead of Chinese. Thanks to all the others for making the Optics research group a nice place, namely Zheng Zhu, Zhongwen Deng, Paolo Ansuinelli, Xukang Wei, Anna Ezerskaia, and Po-Ju Chen.

Thank you to Aurèle Adam for organising the movie nights before it was shown the way to democracy. Thanks to Joseph Braat, Peter Zomers and Paul Plancken for sharing their knowledge about science and (Dutch) society with me. Omar El Gawhary, thanks for the very helpful scientific discussions. I cannot remember a single time I came to you with a question and did not leave with an answer; and usually a set of new questions. Thanks to Jeff Meisner for taking part in all the scientific debates. Running experiments and maintaining a setup is a complicated task, but it would have been an impossible task without the help of the technical support or Rob Pols, Roland Horsten, and Thim Zuidwijk. Thank you for all the help. Another thanks to Yvonne van Aalst to help me with my occasional struggles with the Dutch bureaucracy. I also want to express my gratitude to Florian Bociort and Silvania Pereira.
I also want to thank my students for their curiousity and help in improving the setup. That includes Remo van den Hoek, Farnoosh Farmani, Ton Verhoeven, and Alberto Maran.

I also want to thank the friends I made outside of work, which made life so much more pleasant. Iari Verhuliza, thank you for making Den Haag a fun place to be. Thanks to Kokila Egodage for having been a great support for such a long time and for making me travel the world. Travis Stone and Rachel Richardson, you are the funniest Americans I have met so far. I am indebted to Daniel White for basically running a hospital for the last months I spent in the Netherlands. Also thank you for teaching me why you should always sit in the front of the bus. Alexandru Mare, I am glad to have met you. Keep the business *running*. Ilaria Mengoli, I am indebted to you for sharing Luca with me ;-) Thanks Lorenzo Mengoli for your very own interpretation of the word *cute*. Thanks to Alessandro Garufo for the world's best lasagna and Carito for explaining the difference between *humilde* and *modesto*.

There are still some friends from *back in the days* that kept in contact with me after I moved to the cold north. Per Heisel, Daniel Adolph, and Felix Mucha deserve to be mentioned explicitly, and so do many more that are not mentioned here.

The last words are reserved for the family, and since my parents could not be bothered to learn English I will write it in German:
Vielen Dank an meine lieben Eltern. Ihr habt mich in diese Welt gesetzt und seid damit für dieses Schlamassel verantwortlich ;-) Danke für die inzwischen langjährige Unterstützung und die Autonomität, die ihr mir Recht früh gestattet habt. Danke an Michael und Thomas für das ständige Gehör, die zahlreichen Ratschläge, und die gelegentliche Klugscheißerei. Ihr habt gezeigt wie gut und wichtig Familie sein kann.

CURRICULUM VITÆ

Andreas HÄNSEL

01-09-1986 Born in Erfurt, Germany.

EDUCATION

1997–2005 High School
Buchenberg-Gymnasium, Erfurt (Germany)

2006–2011 Diplom-Physiker
Friedrich-Schiller-Universität Jena (Germany)
Thesis: Effekte der Selbstphasenmodulation in plasmonischen Wellenleitern
Supervisor: Prof. Dr. Falk Lederer, Dr. Rumen Iliew

2012 – PhD. Physics
Technische Universiteit Delft (Netherlands)
Thesis: Applications of Spectroscopy with Multiwavelength Sources
Promotor: Prof. dr. H.P. Urbach
Copromotor: Associate Prof. dr. Nandini Bhattacharya

LIST OF PUBLICATIONS

PEER REVIEWED JOURNAL PUBLICATIONS

7. **A. Hänsel**, K. Hei, Zhongwen Deng, S. Latkowski, S. A. van den Berg, E. A. J. M. Bente, and N. Bhattacharya, *Distance metrology with integrated mode-locked ring laser* (revised manuscript in preparation).

6. **A. Hänsel**, D. Nascimento-Duplat, N. Bhattacharya, and H. P. Urbach, *Resonant $LiNbO_3$ cavity with metal mirrors for polarisation control* (manuscript in preparation).

5. **A. Hänsel**, A. Reyes-Reyes, S. T. Persijn, H. P. Urbach, and N. Bhattacharya, *Temperature measurement using frequency comb absorption spectroscopy of CO_2*, Review of Scientific Instruments **88**, 053113 (2017).

4. S. Latkowski, **A. Hänsel**, P. J. van Veldhoven, D. D'Agostino, H. Rabbani-Haghighi, B. Docter, N. Bhattacharya, P. J. A. Thijs, H. P. M. M. Ambrosius, M. K. Smit, K. A. Williams, and E. A. J. M. Bente, *Monolithically integrated widely tunable laser source operating at 2 µm*, Optica **3**, 1412-1417 (2016).

3. R. Šmíd, **A. Hänsel**, L. Pravdová, J. Sobota, O. Číp, and N. Bhattacharya, *Comb mode filtering silver mirror cavity for spectroscopic distance measurement*, Review of Scientific Instruments **87**, 093107 (2016).

2. S. Latkowski, **A. Hänsel**, N. Bhattacharya, T. de Vries, L. Augustin, K. Williams, M. Smit, and E. Bente, *Novel Widely Tunable Monolithically Integrated Laser Source*, IEEE Photonics Journal **7**, 1-9 (2015).

1. **A. Hänsel**, O. A. Egorov, S. B. Hasan, C. Rockstuhl, and F. Lederer, *Optical bistability in a doubly resonant $\chi^{(2)}$-nonlinear plasmonic nanocavity*, Phys. Rev. A **85**, 053843 (2012).

CONFERENCE PROCEEDINGS

2. S. Latkowski, **A. Hänsel**, D. D'Agostino, P. J. van Veldhoven, H. Rabbani-Haghighi, B. Docter, N. Bhattacharya, P. J. A. Thijs, H. P. M. M. Ambrosius, M. K. Smit, K. A. Williams, and E. A. J. M. Bente, *Long Wavelength Monolithic Photonic Integration Technology for Gas Sensing Applications*, 18th International Conference on Transparent Optical Networks (ICTON), 2016

1. **A. Hänsel**, A. Reyes-Reyes, H. P. Urbach, N. Bhattacharya, and S. A. van den Berg, *Beam path temperature determination for long distance measurements*, 3rd Joint International Symposium on Deformation Monitoring (JISDM), 2016